ANALYSIS OF THE INJECTION OF A HEATED, TURBULENT JET INTO A MOVING MAINSTREAM, WITH EMPHASIS ON A THERMAL DISCHARGE IN A WATERWAY

by

James F. Campbell

Thesis submitted to the Graduate Faculty of the
Virginia Polytechnic Institute and State University
in partial fulfillment of the requirements for the degree of

DOCTOR OF PHILOSOPHY

APPROVED:

J. A. Schetz, Chairman

J. M. Wiggert

G. R. Inger

J. F. Marchman, III

C. B. Ling

December, 1972

Blacksburg, Virginia

ANALYSIS OF THE INJECTION OF A HEATED, TURBULENT JET INTO A MOVING MAINSTREAM, WITH EMPHASIS ON A THERMAL DISCHARGE IN A WATERWAY

by

James F. Campbell

(ABSTRACT)

An experimental and theoretical investigation has been undertaken to study the trajectory and growth of thermal effluents having a range of discharge velocities and temperatures. The discharge of a turbulent effluent into a waterway was mathematically modeled as a submerged jet injection process by using an integral method which accounts for natural fluid mechanisms such as turbulence, entrainment, buoyancy, and heat transfer. The analytical results are supported by experimental data and demonstrate the usefulness of the theory for estimating the location and size of the effluent with respect to the discharge point. The capability of predicting jet flow properties, as well as two- and three-dimensional jet paths, was enhanced by obtaining the jet cross-sectional area during the solution of the conservation equations (a number of previous studies assume a specific growth for the area). Realistic estimates of temperature in the effluent were acquired by accounting for heat losses in the jet flow due to forced convection and to entrainment of free-stream fluid into the jet.

II. TABLE OF CONTENTS

III. ACKNOWLEDGEMENTS

The author wishes to acknowledge the supervisory staff of the National Aeronautics and Space Administration's Langley Research Center for their broad support of his graduate school endeavors. Not only did they encourage him to finish the course requirements for this advanced degree, but upon his return to L.R.C. made sure he had the necessary physical and mental working environment to successfully complete the research.

The author's major advisor Dr. Joseph A. Schetz of the Aerospace Engineering Department provided the inspiration and stimulus for the present work. Dr. Schetz originally suggested the current topic as the dissertation subject, and was always available with his time and advice during the course of the investigation, despite his active pursuits as an outdoorsman, a family man, and Chairman of the AsE Dept.

The following individuals are recognized for their contributions to the present effort:

- Dr. James M. Wiggert of the Civil Engineering Department for providing the water channel used during the experimental tests.
- Dr. J. B. Jones of the Mechanical Engineering Department for the use of the Hydraulics Laboratory in which the experiments were performed.
- Dr. M. J. Werle, now of the Aerospace Engineering Department at the University of Cincinnati, for his helpful comments.
- The author's wife, Jan, for her suggestions concerning the numerical solution of the governing equations.

IV. LIST OF FIGURES AND TABLES

V. NOMENCLATURE

Latin Symbols

A	cross-sectional area of jet control volume
A_i	area of jet orifice ($\pi d_i^2/4$)
A_∞	cross-sectional area of water-channel flow
a	vertical distance of injection port from water-channel floor (see Fig. 18)
B	approximate cylindrical area of jet control volume ($\pi d \Delta s$)
b	width of turbulent mixing zone
C	effective jet circumference, $\sqrt{4\pi A}$
C_D	drag coefficient
C_p	pressure coefficient
c	rate of spread of jet flow
c_p	specific heat at constant pressure of jet fluid
D	drag force on jet flow due to blockage of free-stream flow
d	effective jet diameter, $\sqrt{4A/\pi}$
d_i	diameter of jet orifice
ds	differential length of jet control volume
$d\delta$	elemental area
$d\sigma$	elemental volume
E	entrained mass flow per unit length of jet
E^*	entrainment coefficient

$\vec{e}_N$	unit vector normal to elemental area $d\delta$
$\vec{e}_s$, $\vec{e}_n$, $\vec{e}_t$	unit vectors in natural coordinate system
$\vec{e}_x$, $\vec{e}_y$, $\vec{e}_z$	unit vectors in cartesian coordinate system
F_b	buoyancy force
F_c	centrifugal force
F_p	pressure force
Fr_i	Froude number of jet flow at injection point, $2V_i^2/[d_i g(\rho_\infty - \rho_i)/\rho_i]$
$\vec{f}_b$	body force acting on elemental volume $d\sigma$
g	gravity
H	nondimensional width of jet control volume, h/d_i
H_c	water depth of main flow at injection station (see Fig. 56)
h	width of jet control volume
$\bar{h}$	average film heat-transfer coefficient
K_1	constant in expression for ε, see Eq. (40)
k	thermal conductivity of jet fluid
L	horizontal distance of injection port from flow straightener, see Fig. 18
m	mass of jet fluid in control volume
m_e	free-stream mass entrained into control volume
$\dot{m}_i$	mass flow rate of injectant
$\dot{m}_\infty$	mass flow rate of water-channel flow
Nu_d	Nusselt number based on effective jet diameter $(\bar{h}d/k)$

Pr	Prandtl number
p	local static pressure around perimeter of jet cross section
p_∞	free-stream static pressure
$\bar{p}$	average static pressure in jet flow
Q	rate of heat flow from jet control volume
q	average dynamic pressure of jet flow, $\rho V^2/2$
q_∞	average dynamic pressure of free-stream flow, $\rho_\infty V_\infty^2/2$
R	radius of curvature of jet trajectory
Re_d	Reynolds number based on effective jet diameter, see Eq. (55)
Re_{d_i}	Reynolds number of jet flow at injection point, $V_i d_i/\nu_i$
Re_L	Reynolds number based on horizontal distance L, $V_\infty L/\nu_\infty$
$\vec{r}$	position vector from injection point to a point on the jet trajectory, see Fig. 57
S	frontal area of jet control volume
s,n,t	natural coordinate system attached to jet trajectory, see Fig. 57
T	average temperature of jet fluid, see Eq. (4)
T_∞	average temperature of free-stream fluid
t	time, see Eqs. (1) and (9)
U	velocity, see Eq. (39)

u,w	direction cosines $\cos(\alpha)$ and $\cos(\beta)$, respectively
VR	effective velocity ratio, $[(\rho_i V_i^2)/(\rho_\infty V_\infty^2)]^{1/2}$
V	average velocity of jet flow, see Eq. (4)
V_∞	average free-stream velocity
$\vec{V}$	velocity vector
$V_{\infty,e}$	local free-stream velocity at edge of boundary layer, see Fig. 56
$V_{\infty,\ell}$	local free-stream velocity, see Eq. (A-3)
W_c	width of water channel, see Fig. 56
x,y,z	cartesian (inertial) coordinate system, see Fig. 2
y_o	point above injection surface where laminar jet flow is assumed to begin its turbulent growth

Greek Symbols

α,β,γ	inclination of jet axis with respect to the x,y, and z axes, respectively, see Fig. 57
δ	boundary-layer thickness
Δs	infinitesimal length of jet control volume
ΔT	temperature difference, $T - T_\infty$
ε	virtual kinematic (eddy) viscosity
ψ,ξ	constants in expression for Nu_d, see Eq. (54)
θ	angular orientation of p, see Fig. 8
λ	velocity parameter in expression for K_1, see Eq. (45)

ν	kinematic viscosity
ρ	average density of jet fluid, see Eq. (4)
ρ_∞	average density of free-stream fluid
τ	shear stress in s-direction acting on jet flow
$\overline{\overline{\tau}}$	surface stress tensor
τ_o	torsion of jet trajectory, see Eq. (B-9)

Subscripts

i	conditions at point of jet injection
max	maximum
min	minimum
ℓ	local value of jet flow property
s,n,t	condition in s,n,t directions
∞	condition associated with the free-stream flow
1,2	jet flow conditions in control volume before and after entrainment

VI. INTRODUCTION

One of the most basic processes in fluid mechanics is the mixing that occurs during the interaction of two intersecting streams of fluid. A large portion of interaction processes exists where one stream of fluid has a much smaller mass (or volume) flow than the other stream, such as the case of a plume issuing from a smoke stack or a fluid injecting into a boundary layer on a vehicle traveling at hypersonic speeds. This class of interaction problems can be categorized as fluid, or jet, injection processes, and are usually associated with a nearby solid boundary or surface,and are complicated by the fact that in their natural state they are almost invariably turbulent.

An example of a fluid injection process of current interest is where a heated water effluent is discharged into a river, reservoir, or estuary, the water being initially heated during the course of some industrial process. For example, the generation of electricity accounts for approximately 70 percent of the waste heat discharged daily into waterways in the nation.[1] In order to satisfy the nations' demand for electricity in 1980, almost 250 billion gallons of water per day will be required for cooling, of which about 200 billion gallons will be from fresh water sources. This will comprise 1/5 of all fresh water run-off in the country. A schematic diagram is presented in Fig. 1 (Aronson[2]) to illustrate how fuel in an electric power plant becomes electrical energy and how water from a nearby river or reservoir

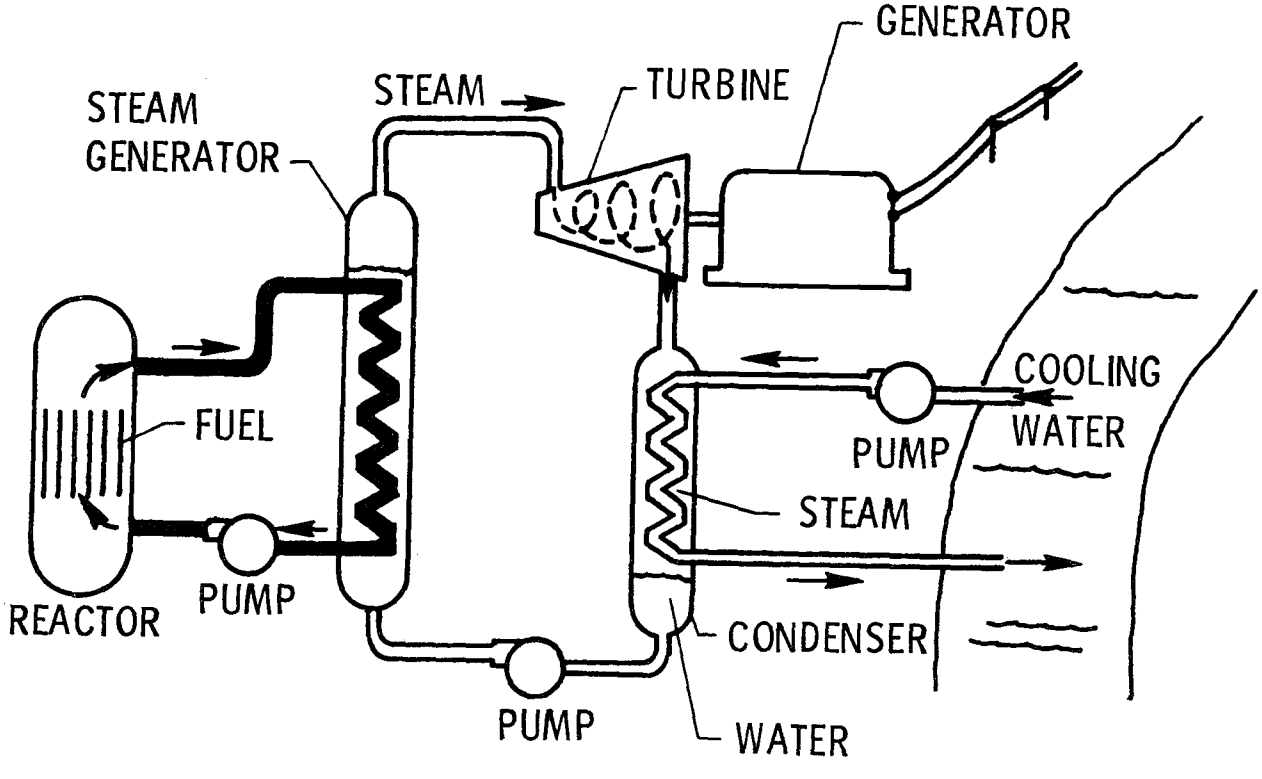

Figure 1.- Schematic diagram of thermal power plant flow system (after Aronson[2]).

becomes heated. The steam used to turn the turbines and hence to generate electricity must be condensed in order to be re-used. Cooling water drawn from a nearby water source circulates through the condenser withdrawing heat from the steam, and in its warmed-up state is then returned to the water source. The increase in cooling water temperature above the ambient temperature is typically 10° to 25°F, depending of course on the volume flow of water through the condenser and the amount of heat extracted. This process of heat disposal, called the "once-through" cooling method, is the most widely used technique because it is the easiest to build and the cheapest to operate (Woodson[3]). At present about 90 to 95 percent of steam-electric cooling water is put back into the waterway using this once-through method; the remaining percentage of water is treated in cooling towers and/or ponds before discharge.

In an attempt to control the growth of this problem, water quality standards have been legislated which set temperature limits (above the ambient temperature) on the various types of water bodies accepting heated water. All of these standards apply to that region of the receiving water outside of the "mixing zone", where the heated effluent mixes with the ambient water. The fact that the definition of the mixing zone varies not only from state to state, but often between different locations within the same state, adds to the ambiguous nature of the problem.

A great deal of information has been generated concerning the effects of heat on aquatic life (Refs. 4 to 6), however it has only

been in recent years that serious research attention has been turned to the fluid physics involved with modeling the heated discharge. Many of the previous studies directed towards the physical understanding of the calefaction of waterways have been more concerned with the far-field effects of the thermal discharge. Examples of this are the works by Edinger and Geyer[7] who consider the overall heat balance of bodies of water having excess heat addition, and Mahgary[8] who attempts to examine the diffusion of water temperature assuming a two-dimensional mixing model, but neglects to consider momentum transport. Since it is desirable to observe the time history of a heated effluent (or thermal plume) from the point of discharge to the point of final thermal mixing with the ambient fluid, it is therefore necessary to consider the near-field effects. In their general reviews of research needs, Tichenor[9] and Parker[10] stressed the importance of considering the momentum jet as the method of modeling the discharge in the near field. This is certainly the more pragmatic approach to the physical understanding of the problem, particularly if the definition of a thermal mixing zone is desired in order to minimize impact on the local water environment.

Accordingly, the present study was initiated to investigate the pertinent fluid mechanics and heat-transfer aspects of heated, turbulent effluents discharging into a moving water environment. Emphasis has been given to determining the effects of the ambient flow variables and effluent discharge properties on the three-dimensional path, or trajectory, of the thermal plume and to examining how the flow properties of and heat loss from the plume vary along the path. In a realistic

situation, the heated effluent would be discharged into an irregular velocity field typical of most river flows, however, in order to provide a starting point for the present theoretical analysis, the effluent is considered as a submerged jet flow injecting into a moving water system having a spatially dependent velocity field. The general development of the theoretical model is contained in Chapter VIII, with details contained in the Appendices in Chapters XIV and XV. The theory is compared with other analytical models in Chapter X, as well as with experimental data acquired from a number of investigations. Experimental tests were conducted for the lateral, vertical, and oblique jet injection into a water channel, the jet having a range of injection velocities and temperatures. Results of the tests are described in Chapters IX and XIII and are presented to verify the major assumptions of the mathematical model. Results are represented by properly non-dimensionalized parameters to make the analysis applicable to any situation.

VII. REVIEW OF LITERATURE

Since the question of siting thermal discharges on a moving waterway will largely be settled on the basis of localized effects near the outfall, it is important for us to understand the fluid mechanics of the jet injection process. Margason's bibliography[11] on previous experimental investigations of incompressible jets injecting into a cross flow provides a starting point for the discussion. The complex interaction that takes place after a fluid is injected into a moving stream results in a three-dimensional flow field, even though the jet may be following a two-dimensional path. This, of course, complicates the job of the experimentalists. Gordier[12], Margason[13], and Platten and Keffer[14], concentrated their efforts on measuring the jet's trajectory for a wide range of injection angles (α_i) and velocities (V_i/V_∞), the trajectory being one of the easiest jet properties to measure (see Fig. 2). Jordinson[15], Keffer and Baines[16], Ramsey[17], and Kamotani and Greber[18] measured details of the interaction process and revealed the very complex flow field that exists due to the pressures and shear stresses in and around the jet flow. Very good descriptions of how the jet flow distorts and develops under the influence of the free-stream flow and body forces are given by Keffer and Baines[16], Ramsey[17], Abramovich[19], and Keffer[20].

The most detailed measurements of the flow field appear to be those of Keffer and Baines[16], and Kamotani and Greber[18]. In particular, Kamotani and Greber examine the structure of the rotational velocity

field which results because of the shearing action between the free-stream flow and the edge of the jet flow. The rotational velocity field, usually interpreted to be a pair of counter-rotating vortices, is an interesting as well as important facet of the injection process; it affects the path of the jet as well as the mechanisms that govern entrainment. Both Refs. 16 and 18 reduced their data so a measure of mass flux in the jet could be obtained, which in turn resulted in estimates of the rate that free-stream fluid is entrained into the jet structure. In addition to investigating the characteristics of the velocity field, Ramsey[17] and Kamotani and Greber[18] measured the temperature field resulting from the injection of a heated jet.

It is important to note the limiting conditions of a jet injected at an arbitrary angle into a cross flow. If the angle between the jet axis and the direction of the free-stream velocity (α) goes to zero for a given V_i/V_∞, the condition exists of a jet in a co-flowing stream. If the jet velocity becomes very large ($V_i/V_\infty \to \infty$) for a given α, the situation approaches that of a free jet. An indication of the magnitude of entrainment for a jet in a co-flowing stream and for a free jet has been provided by Morton[21], and Ricou & Spalding[22], respectively.

In reviewing some of the theoretical methods available for modeling an injection process, it should be emphasized that a method is desired here which allows the thermal effluent to be followed from its point of discharge to some point downstream where complete thermal mixing takes place. At a minimum, the method should be able to estimate the three-dimensional (3-D) path of the thermal plume, show how the plume

size varies as it procedes downstream, and include basic heat-transfer mechanisms which allow the plume temperature to be predicted. The most advanced method would result in a complete and detailed description of the flow field resulting from an injection into a moving stream. This could be done by solving the full three-dimensional, turbulent, Navier Stokes equations in an Eulerian framework, which requires the specification of the eddy viscosity field.

In order to avoid the complexities inherent with this approach, many studies have tried to theoretically model the gross features of the injection process by describing the fluid motion of the jet from the point of discharge in a Lagrangian framework. This procedure allows an estimate of jet properties to be obtained if the appropriate forces acting on the jet flow are accounted for. Since the jet path is the most obvious of the jet properties, it is natural that early attempts were concerned only with obtaining estimates of the trajectory. Abramovich[19], for example, obtained the trajectory of a jet which had a circular cross-section at the injection point by balancing the centrifugal and blockage forces perpendicular to the trajectory. His basic argument was that the blockage effect of the jet flow on the free-stream flow could be approximated by assuming that the jet flow acts as a "solid" body inclined at some angle to the free stream. He accounted for the deformation of the jet's cross-section by assuming the shape to be elliptical and by specifying a growth rate for the cross-sectional area, which is necessary if only one force equation is used to obtain a solution for the trajectory. One of the serious drawbacks of this method is the

assumption that the component of jet momentum perpendicular to the direction of the free-stream flow remains constant. This assumption was relaxed by Schetz and Billig[23].

Two other forces acting perpendicular to the jet trajectory and which help govern the development of the jet flow are: (1) buoyancy force resulting from a difference in density between the jet and free-stream fluids, and (2) entrainment force resulting because of the free-stream fluid that is drawn into the jet structure. Theoretical trajectories were obtained by Reilly[24] and Campbell and Schetz[25] using procedures similar to those described above, but also accounting for the entrainment phenomenon; Campbell and Schetz, in addition, included the buoyancy force in their model.

Since all of these previous works utilized an assumed area growth based on experimental data obtained in the proximity of the injection point, they are not suitable for providing realistic trajectory information further downstream. This deficiency can be avoided if, instead of assuming an area growth rate, a momentum conservation equation in the direction of the jet path is used; this equation is used in addition to the conservation equation perpendicular to the trajectory. Wooler et. al.[26] and Hoult et. al.[27,28] used this procedure, solving force equations normal and parallel to the jet path simultaneously to obtain a solution for the trajectory. An added advantage of using these two force equations is that, if all of the appropriate forces are accounted for, the solution procedure allows the jet flow properties to be estimated. The theoretical studies discussed up to this point,

however, do not include all of the necessary forces. This is illustrated in Table I which presents a summary of the capabilities of a number of theoretical investigations. In particular, the shear stresses that exist in the flow field due to differences between the jet and free-stream velocities are not represented in most theoretical efforts. The shear force normal to the trajectory is usually combined with the force due to the pressure distribution around the jet flow to form the blockage force (mentioned previously). The shear force parallel to the jet path must be accounted for in a force balance on the jet flow, which was done by Hirst[29] and Campbell and Schetz[30].

The theories discussed thus far have been concerned with predicting the flow characteristics of a jet following a two-dimensional (2-D) path. This type of path occurs when the radius-of-curvature vectors associated with the trajectory lie in one plane, the trajectory of course being a curve in that plane. If the injection and free-stream velocity vectors shown in Fig. 2 are considered to form an "injection plane", then a two-dimensional trajectory will always result when this plane is oriented vertically, i.e. aligned with the gravity vector. When the injection plane is rolled away from the vertical, a three-dimensional trajectory may occur depending on the buoyancy of the jet flow. If the buoyancy force is absent, or is small with respect to the jet momentum, then a two-dimensional path will result. A larger buoyancy force, however, will cause the jet to bend out of the injection plane, and the result will be a three-dimensional trajectory. The radius-of-curvature vectors associated with this type of trajectory

TABLE I. - CAPABILITIES OF PREVIOUS THEORIES USING INTEGRAL TECHNIQUES

Investigators	Arbitrary Injection Velocity	Arbitrary Injection Angle	Forces parallel and perpendicular to jet trajectory				Jet Flow Properties		3-D Trajectory
			Blockage	Entrainment	Buoyancy	Viscous Shear	ρ, A, V	T	
Abramovich[19]	X	X	X						
Schetz and Billig[23]	X	X	X						
Reilly[24]	X		X	X					
Campbell and Schetz[25]	X		X	X	X				
Wooler et. al.[26]	X		X	X					
Hoult and Fay[27]	X			X	X				
Hoult and Weil[28]	X			X	X				
Hirst[29]	X	X	X	X	X	X	X		X*
Campbell and Schetz[30]	X	X	X	X	X	X	X	X	
Present	X	X	X	X	X	X	X	X	X

* No 3-D trajectory results given

do not lie in one plane. Since a jet with a two-dimensional trajectory is a special case of the jet with the more general three-dimensional trajectory, it is desirable to have a theory that can estimate the more general situation. At present, the only theoretical method which appears capable of predicting jet flows with three-dimensional trajectories is that of Hirst, although no results of this kind were presented in his report (Ref. 29).

In view of the preceding comments, the purpose of the theoretical portion of the present investigation is to develop an integral method which accounts for natural fluid mechanisms such as turbulence, entrainment, buoyancy, and heat transfer in the conservation equations governing the jet flow. In particular, it is desirable to have a theory that: (1) utilizes the momentum conservation equation along the jet path, in addition to that perpendicular to the path, in order to avoid any assumption regarding the growth of the jet's cross-sectional area as was done in Refs. 19, 23-25; (2) accounts for a shear force in the momentum equation along the jet trajectory, which was not included in the works in Refs. 26-28, in order to provide improved predictions of two-dimensional jet trajectories, and to allow estimates of jet flow properties, such as velocity, cross-sectional area, and momentum, to be made; (3) obtains a third momentum conservation equation for the jet flow which, when solved simultaneously with the other two momentum equations, allows three-dimensional jet paths to be calculated, thus extending the theories reported in Refs. 29 and 30; (4) provides estimates of the temperature of the jet fluid by examining several heat

transfer mechanisms that can account for the heat loss from the jet flow; and (5) is easily adapted to account for free-stream flows with either a nonuniform velocity field or a nonuniform temperature field. The purpose of the experimental portion of the present study is to provide information for a submerged jet injected laterally, vertically, and obliquely into a water channel in order to support the theoretical effort, as well as to extend the experimental results of previous investigations. It is desirable to examine the effects of changing injection velocity for the different injection orientations, and to provide test results at higher injection velocities than those reported in Refs. 12 to 20. In addition, the effects of increasing injectant temperature on the injection processes should be ascertained, and measurements of jet temperature decay made to compare with the results of Refs. 17 and 18.

VIII. THEORETICAL DEVELOPMENT

This chapter is concerned with the development of a theory which approximates the fluid mechanical process that occurs when a submerged, turbulent jet of circular cross-section is injected into an effectively infinite free-stream flow. The mathematical model should allow the jet to penetrate into the cross flow, to bend over and spread under the influence of natural fluidic forces, and the jet's velocity vector to approach the free-stream velocity vector at some point downstream from the jet exit. This capability is obtained by considering a section of jet fluid as a control volume similar to the approach used by Reilly[24]. This is illustrated in Figure 2 which depicts the trajectory of a jet injecting into a free-stream flow having a velocity $\vec{V}_\infty$, taken to be spatially but not time dependent. The origin of the cartesian (x,y,z) axis system is at the injection point, while the natural (s,n,t) axis system moves and rotates as it follows the path of the jet axis which is traced out by the jet velocity V. The s-axis is located along the trajectory, while the n-axis is oriented perpendicular to the trajectory in the direction of the radius of curvature of the trajectory; the t-axis is perpendicular to both the s- and n-axes. A complete discussion of the natural coordinate system is given in Appendix B. The equations expressing conservation of mass and momentum in the direction of the natural axes are derived in the following sections.

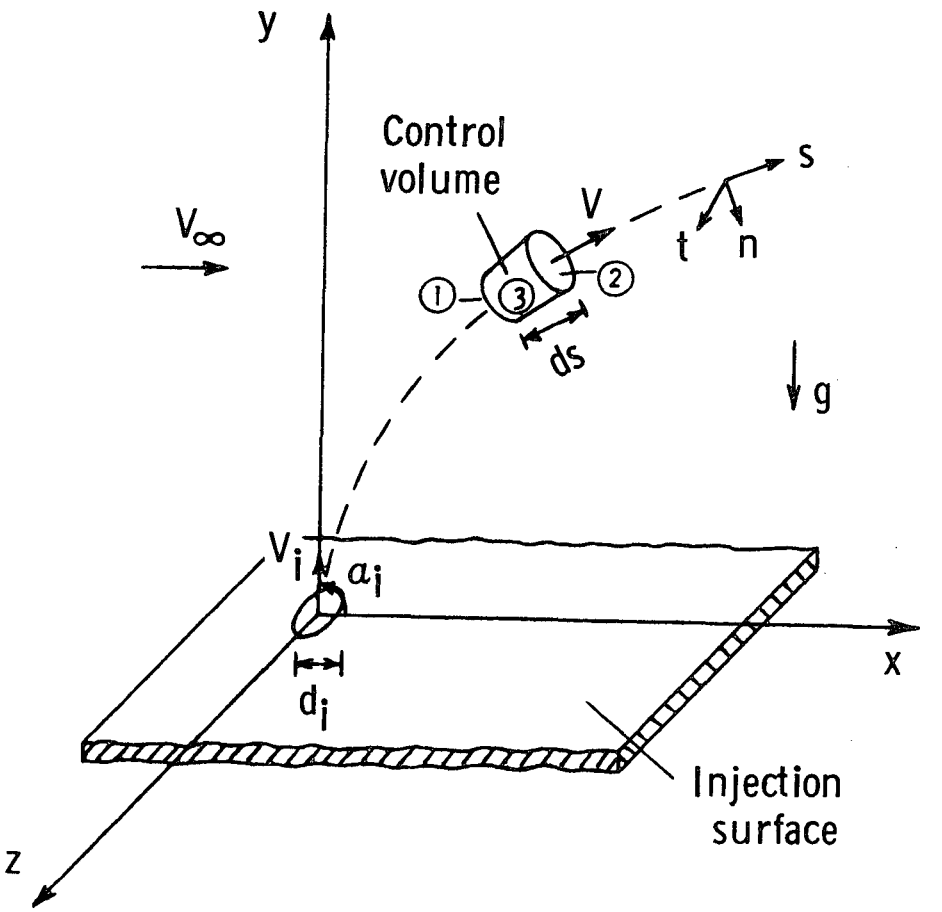

Figure 2.- Cartesian and natural coordinate systems.

Continuity

The following integral expression equates the net influx of mass into the control volume to the rate of increase in mass in the control volume:

$$\frac{\partial}{\partial t}\iiint \rho_\ell d\sigma = -\iint \rho_\ell \vec{V} \cdot \vec{e}_N d\delta \qquad (1)$$

where $d\delta$ and $d\sigma$ represent the elemental surface area and volume, respectively. It is assumed that the flow process is steady (in the mean), fully turbulent, and incompressible. The fact that we assume incompressibility does not imply that the flow process is one of constant density. Equation (1) thus becomes,

$$\iint \rho_\ell \vec{V} \cdot \vec{e}_N d\delta = 0 \qquad (2)$$

Carrying out the operations suggested by this equation leads to the mass flows through the surfaces of the control volume (①, ②, and ③ in Fig. 2).

It is noted that $d\delta = dA$ for surfaces ① and ②, which represent a cross-section of the jet flow; i.e. areas that are perpendicular to the trajectory. Since mass flow is a continuous, single-valued function of position along the trajectory, a Taylor expansion can be performed to obtain the mass flow through surface ② as a function of the mass flow through surface ①. The difference between mass flows through ① and ② represents the mass flow through

the sloping face (3), which defines the amount of free-stream fluid mass (per unit of jet length) that is entrained (E), or drawn, into the control volume. This can be written as,

$$E = \frac{d}{ds}\left[\iint_{(1)} \rho_\ell V_\ell dA\right] \tag{3}$$

The two most common profiles used in the literature to describe the velocity variation at a given cross-section in the jet flow are the Gaussian and Top-hat. The Gaussian representation is particularly useful for providing estimates of flow properties on the jet's centerline and was used in the development of Hirst[29]. In using the Gaussian profiles, however, the assumption is made that the jet flow is circular, i.e. axisymmetric, which is valid for free-jet flows and for co-flowing jet flows, but is of questionable use for a jet injecting into a cross flow, where the jet cross-section is not circular[16]. In addition, the theoretical results obtained by using a Gaussian velocity profile are only applicable in the region where the jet flow has become fully developed.

Top-hat profiles represent the average jet flow properties and have been used in a number of theoretical studies[19,23,24,26,28]. By using the average flow properties in the conservation equations, it is not necessary to place restrictions on the symmetry of, or to assume similarity in, the jet flow. This means that the governing equations can be used to describe the jet flow in the region where the jet is fully developed, or in the region where the jet is only partially

developed and a potential core still exists. Accordingly, the present study uses the averaged jet flow properties defined as follows:

$$V = \frac{\iint V_\ell \, dA}{\iint dA} \qquad \rho = \frac{\iint \rho_\ell \, dA}{\iint dA} \qquad T = \frac{\iint T_\ell \, dA}{\iint dA} \tag{4}$$

which state that at a given location along the trajectory the jet's local velocity, density, and temperature values are integrated over the jet cross-sectional area. This permits the conservation of mass in the jet, equation (3), to be expressed in differential form as,

$$E = \frac{d(\rho A V)}{ds} \tag{5}$$

Morton[21], Reilly[24], and Wooler et. al.[26] obtained continuity equations of this form.

In recent years it has been recognized that inclusion of the entrainment process in a jet injection analysis is important not only because of its influence on jet momentum, and hence trajectory, but also because this process allows for the mixing of jet and free-stream scalar properties such as temperature and salinity. The fact that entrainment occurs when there is relative motion between two flow fields has been used by different researchers to justify relating entrainment to the appropriate velocities normal and parallel to the jet axis. This type of representation of the entrainment function (E) results in a variety of empirical "constants" which must be adjusted in order to obtain suitable agreement with experimental data. Examples

of several attempts to approximate E in this fashion are seen in the works of Kamotani & Greber[18], Wooler et. al.[26], and Hoult et.al.[27,28] The model of entrainment presented by Wooler et. al. uses three constants, one of which is obtained by satisfying the Ricou-Spalding measurements[22] for an isothermal free-jet. Experimental trajectory data, rather than mass flux information, were used as the criterion for indirectly adjusting the other two constants. Experimental mass flow data are presented by Kamotani & Greber to support the constants used in their model of the entrainment function.

Because of the complex helical streamline pattern (usually interpreted as a pair of counter-rotating vortices) evident in the lee side of the jet, it is believed that the entrainment function cannot be split into two totally independent parts as assumed in the above description. One attempt to account for the free-stream fluid entrained into the jet as a result of the helical circulation pattern has been reported by Platten & Keffer[31]. Their entrainment model was extended by Hirst[29] to account for local buoyancy in the jet flow.

In consideration of the complicated nature of analytically predicting the entrainment function and the desire to keep empirical constants to a minimum, the present study defines this jet property by using the experimental data for an air jet obtained by Keffer & Baines[16]. Equation (6) represents

$$E = \frac{A}{C} \rho_\infty E^* (V - V_\infty) \qquad (6)$$

the entrainment parameter in functional form, where the entrainment coefficient (E^*) was obtained from measurements of mass flux along the jet axis[16]. In order to use this formulation for E, V must always be equal to or greater than V_∞. The entrainment coefficient is presented in Figure 3 for three injection velocities and, as noted, is a function of both injection velocity and distance along the trajectory. An empirical expression was obtained here to represent E^* in the present mathematical model and is shown compared with the experimental data. It is assumed that this function can be used at larger values of VR and s/d_i than those shown in the figure.

It should be noted that the empirical expression for E^* implies that as $s \to 0$, E^* (and hence E) $\to 0$. This is an unsettling possibility because, near $s = 0$, the jet flow in this type of injection process might be expected to resemble that of a free jet, having similar entrainment rates. Keffer & Baines[16] observed that as $s \to 0$ E^* was of the same order as that found by Morton[21] for simple jet flows. This is further substantiated if we consider the work of Ricou & Spalding[22] who measured entrainment for axisymmetric turbulent free-jets. The formula they suggested as best representing their data is,

$$\frac{\rho AV}{(\rho AV)_i} = 0.32 \frac{s}{d_i} \tag{7}$$

This can be differentiated with respect to s to get the entrainment in the free jet. Putting the results in the same form used by

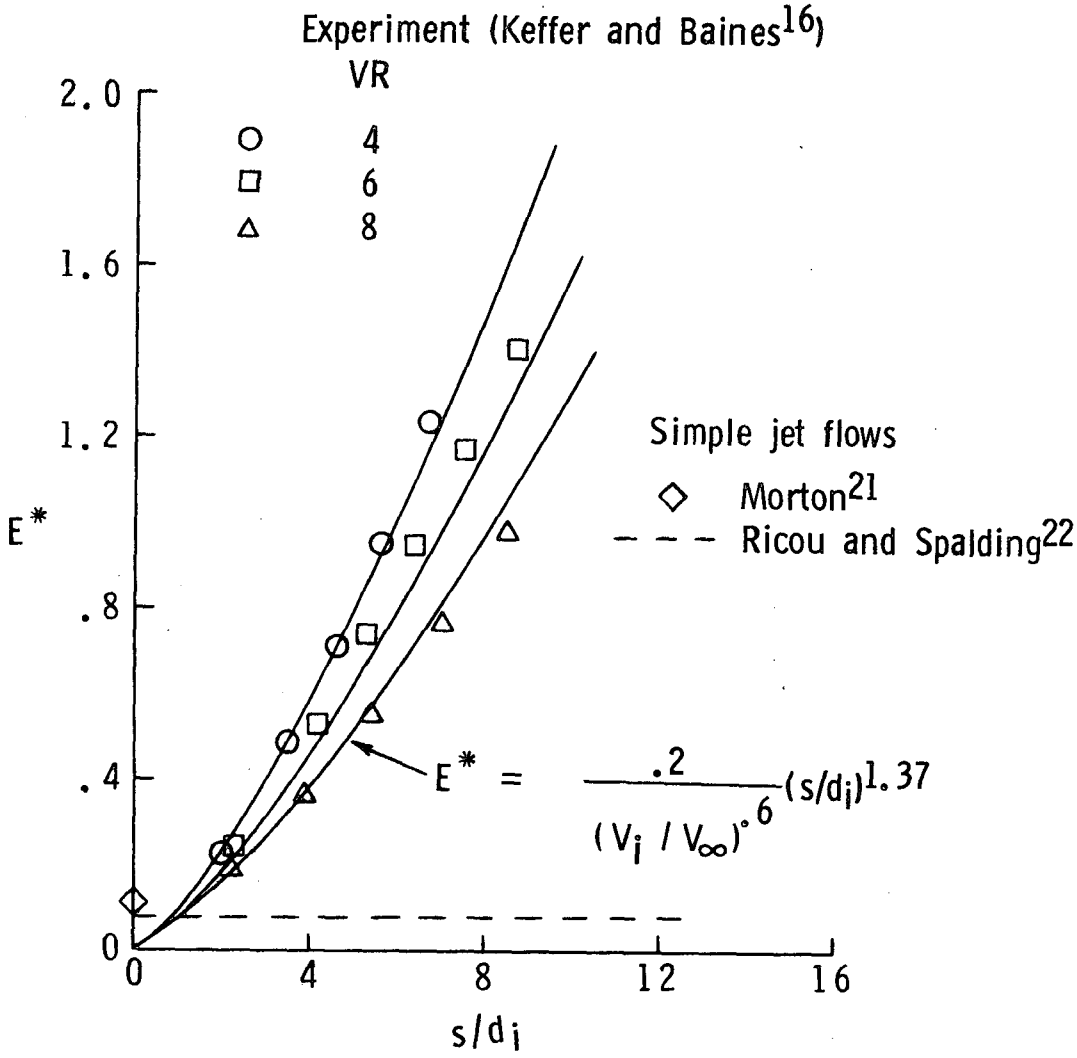

Figure 3.- Entrainment coefficient as a function of position along axis of isothermal air jet; $\alpha_i = 90°$.

Morton we get,

$$E = 0.08\, C_i \rho_i V_i \tag{8}$$

Thus the constant 0.08 compares favorably with Morton's value of 0.116.

It is assumed in the present study that $E^* = 0.08$ until the empirical expression presented in Figure 3 predicts a greater value, which is then used. This is reasonable in view of the fact that an increase in VR decreases E^* so that as $VR \to \infty$, E^* should approach the free-jet value.

Conservation of Momentum

The following integral expression equates the rate of increase of momentum in the control volume to the sum of forces acting on the control volume plus the net influx of momentum into the control volume:

$$\frac{\partial}{\partial t} \iiint \rho_\ell \vec{V}\, d\sigma = \iiint \vec{f}_b\, d\sigma + \iint \bar{\bar{\tau}} \cdot \vec{e}_N\, d\delta - \iint \vec{V}(\rho_\ell \vec{V} \cdot \vec{e}_N\, d\delta) \tag{9}$$

where the surface stress tensor ($\bar{\bar{\tau}}$) is taken to contain both shear and pressure terms and $\vec{f}_b \equiv$ body force per unit volume. Since we have assumed a time independent flow process, the term on the left-hand side of the equation is zero; hence,

$$\iiint \vec{f}_b\, d\sigma + \iint \bar{\bar{\tau}} \cdot \vec{e}_N\, d\delta - \iint \vec{V}(\rho_\ell \vec{V} \cdot \vec{e}_N\, d\delta) = 0 \tag{10}$$

where the equation will be shown to yield expressions for momentum in the direction of the natural coordinates.

Assuming the body forces are independent of the integral over $d\sigma$, we write

$$\iiint \vec{f}_b \, d\sigma = \vec{f}_b \iiint d\sigma = \vec{f}_b \, A \, ds \tag{11}$$

where, as a first approximation, the volume is assumed to be equal to Ads, which neglects the rate of change of A with s. Since the components of $\vec{f}_b$, and later $\vec{V}_\infty$, are desired in the s, n, and t directions, we can use a vector identify to obtain,

$$\vec{f}_b = (\vec{f}_b \cdot \vec{e}_s)\vec{e}_s + (\vec{f}_b \cdot \vec{e}_n)\vec{e}_n + (\vec{f}_b \cdot \vec{e}_t)\vec{e}_t \tag{12}$$

and

$$\vec{V}_\infty = (\vec{V}_\infty \cdot \vec{e}_s)\vec{e}_s + (\vec{V}_\infty \cdot \vec{e}_n)\vec{e}_n + (\vec{V}_\infty \cdot \vec{e}_t)\vec{e}_t \tag{13}$$

where $\vec{V}_\infty = V_\infty \vec{e}_x$.

There are two body forces considered to be acting on the jet flow. The first force is due to the buoyant condition which results from a difference in density between the jet and free stream fluids. This force acts in the y direction and is given by,

$$\vec{F}_b = F_b \vec{e}_y = g(\rho_\infty - \rho)\vec{e}_y \tag{14}$$

The second force results from centrifugal effects associated with the jet having mass and following a curved path. This force acts in the direction of the radius of curvature of the trajectory and is expressed as,

$$\vec{F}_c = F_c \vec{e}_n = \frac{m V^2}{R} \vec{e}_n \tag{15}$$

The total body force on the control volume ($\vec{f}_b$) is the vector sum of the buoyancy and centrifugal forces and is substituted into Eq. (12) to obtain,

$$\vec{f}_b = F_b(\vec{e}_y \cdot \vec{e}_s)\vec{e}_s + [F_b(\vec{e}_y \cdot \vec{e}_n) + F_c]\vec{e}_n + F_b(\vec{e}_y \cdot \vec{e}_t)\vec{e}_t \tag{16}$$

The pressure portion of the shear-stress tensor term in Eq. (10) can be written in component form as,

$$\oiint p\vec{e}_N \, d\delta = - \oiint_{(1)} p_\ell \vec{e}_s \, d\delta + \oiint_{(2)} p_\ell \vec{e}_s \, d\delta + \oiint_{(3)} p_\ell \vec{e}_n \, d\delta$$

$$+ \oiint_{(3)} p_\ell \vec{e}_t \, d\delta - \oiint_{(3)} p_\ell \vec{e}_s \, d\delta \tag{17}$$

where p_ℓ represents the local pressure on the respective surfaces indicated by the integration.

n-Momentum

The n-momentum equation is obtained by taking the n components

of the various vector quantities in the momentum integral equation (10). The term representing the body forces, for example, is extracted from Eq. (16) as,

$$f_{b_n} = [F_b(\vec{e}_y \cdot \vec{e}_n) + F_c] \, A \, ds \tag{18}$$

while the pressure force is obtained from Eq. (17) to be,

$$F_{p_n} = \iint_{(3)} p_\ell \, d\delta \tag{19}$$

This pressure force is combined with the shear stress integrated over surface (3) to obtain the total drag force (D_n) on the jet flow due to blockage of the free stream flow. It is noted that for many injection situations the centrifugal force is in the opposite direction from the drag force, the drag force being in the positive n direction.

Because of the complexity of the interaction between the jet and free-stream flows, the force resulting from the blockage effect is postulated to be the drag on an equivalent "solid" cylindrical jet shape inclined at an angle to the free-stream flow (after Abramovich[19]). This can be expressed as,

$$D_n = C_{D_n} q_{\infty_n} S_n \tag{20}$$

where the dynamic pressure of the free-stream flow perpendicular to the jet axis is given by

$$q_{\infty_n} = \frac{1}{2} \rho_\infty V_{\infty_n}^2 \tag{21}$$

Employing the definition $V_{\infty_n} = V_\infty(\vec{e}_x \cdot \vec{e}_n)$ results in

$$q_{\infty_n} = q_\infty(\vec{e}_x \cdot \vec{e}_n)^2 \tag{22}$$

The reference area for calculating the drag force is the frontal area of the control volume (the surface facing the free-stream direction):

$$S_n = h\, ds \tag{23}$$

where h is the local width of the jet measured in the t direction. Incorporating the expressions for q_{∞_n} and S_n into Eq. (20) allows the drag force to be finally expressed as,

$$D_n = C_{D_n} q_\infty (\vec{e}_x \cdot \vec{e}_n)^2 \, h \, ds \tag{24}$$

The third term in Eq. (10) accounts for the net influx of momentum into the control volume, which for the n direction, is due solely to the flux across the slanted surface of the cylinder. It is represented by the rate at which mass enters the sides of the control volume, see equation (3), multiplied by the free-stream velocity component in the n-direction. Thus,

$$\iint_{\vec{V}}(\rho_\ell \vec{V} \cdot \vec{e}_N \, d\delta) = V_{\infty_n} \frac{\partial}{\partial s}\left[\iint \rho_\ell V_\ell \, dA\right] ds = V_{\infty_n} E \, ds \qquad (25)$$

Equations (18), (24), and (25) are combined to yield the conservation of momentum in the n-direction:

$$\frac{\rho A V^2}{R} = g(\rho_\infty - \rho)(\vec{e}_y \cdot \vec{e}_n)A + C_{D_n} q_\infty h(\vec{e}_x \cdot \vec{e}_n)^2 + E \, V_\infty(\vec{e}_x \cdot \vec{e}_n) \qquad (26)$$

where the mass of the control volume is taken to be $m = \rho A ds$. The expressions for the dot products in terms of the cartesian coordinates as the dependent variables and the distance along the trajectory as the independent variable are given in Appendix B. Substituting the appropriate definitions the n-momentum equation becomes,

$$\frac{\rho A V^2}{R} = gA(\rho_\infty - \rho)R \frac{d^2y}{ds^2} + C_{D_n} q_\infty h R^2 \left(\frac{d^2x}{ds^2}\right)^2 + E \, V_\infty \, R \frac{d^2x}{ds^2} \qquad (27)$$

where the radius of curvature (R) of the trajectory is defined in Appendix B. Previous studies investigating the 2-D injection problem (usually vertical injection) proceed to put this equation into a form with the slope of the trajectory, or the angular orientation, as the dependent variable. Since the vertical and lateral injection problems will be treated here as special cases of the more general 3-D injection situation, it is desirable not to specialize the equations in that way. The reader will see in Appendix C how this

equation is nondimensionalized and put into the form used in obtaining a numerical solution on the computer. The direction cosines of the jet velocity vector (i.e. $\vec{e}_s$) were chosen as the dependent variables for several reasons, one of which is that the order of the governing eqns. is reduced by one. In addition, the algebra is thereby kept to a manageable level.

It is appropriate to mention that at this stage of the development, the approach used in a number of previous studies[19,23-25] has been to assume the area growth of the jet along the trajectory, the rate of growth being based on data measurements where $s/d_i \leq 10$. This was done in lieu of solving the s-momentum equation. The area growth can be obtained by assigning a certain shape for the jet cross-section (e.g., circular or elliptical) and by allowing the jet width to grow at a specified rate. Schetz and Billig[23] used the expression for mass flow in the jet, that is, the continuity equation, to eliminate velocity in the n-momentum equation, the resulting expression then being integrated to obtain a solution for the jet trajectory. Typical results obtained by this procedure are presented in Fig. 4 for a jet with an elliptical cross-sectional shape and are compared with experimental data acquired from the photographs in Ref. 25.

Comparison of the assumed cross-sectional areas with the values obtained from experiments shows that the two are in reasonable agreement in the proximity of the jet exit, but that the values diverge as the jet proceeds downstream. (It is noted that the

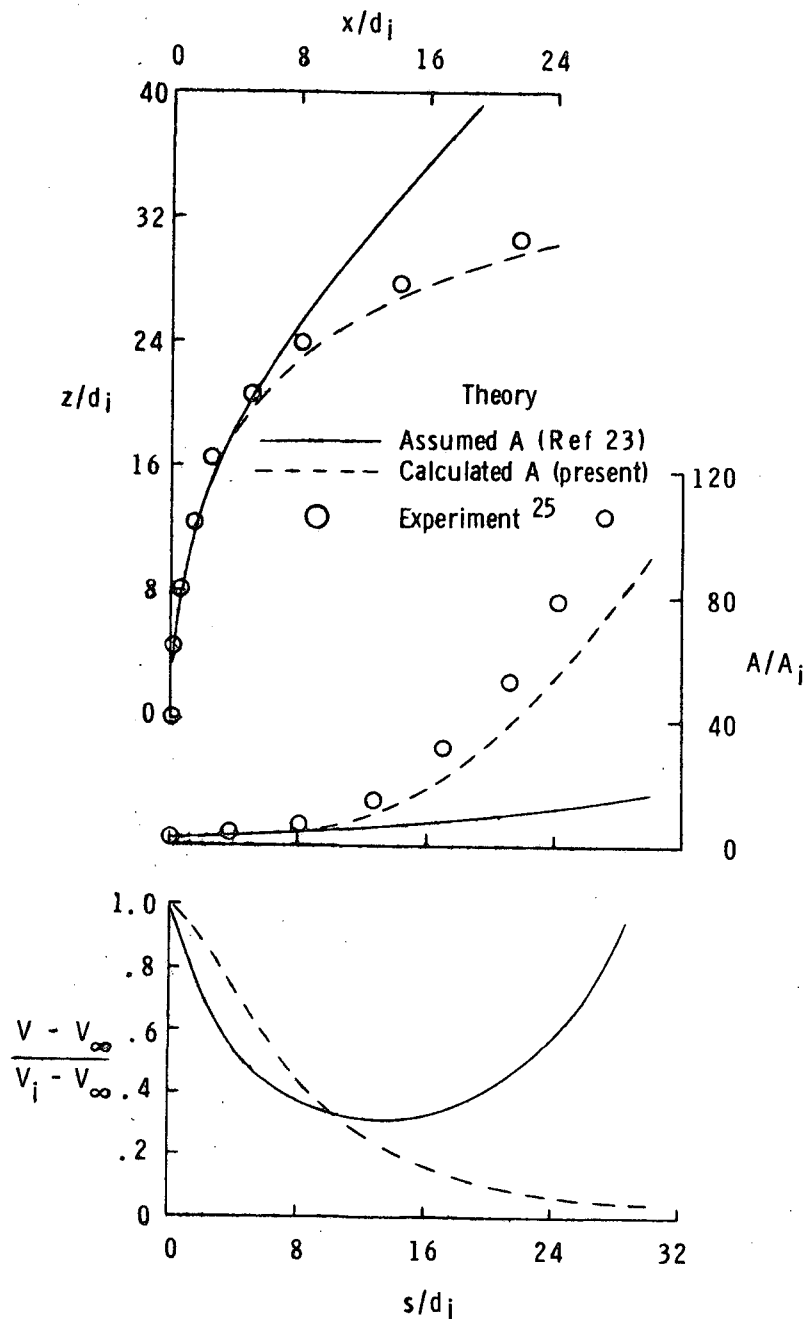

Figure 4.- Experimental and theoretical jet flow properties; VR = 18.2, $T_j/T_\infty = 1.0$, $\alpha_j = 90°$.

investigators who made the area-growth assumption were predominantly interested in the jet's trajectory in the proximity of the injection point.) the measured areas indicating a much more rapid rate of jet growth than the assumed values. This trend is reflected in the trajectory information where good agreement between the predicted and experimental trajectories is noted in the initial region after jet injection, but poorer agreement occurs farther downstream. Another effect of assuming area growth is seen in the erroneous trends for the theoretical jet velocity, illustrated in the figure by the velocity deficit curve. As noted, the jet velocity begins to increase at some point along the trajectory. The reader is aware, of course, that as long as the jet injection velocity is greater than the free-stream velocity, the jet velocity will decrease continuously along the trajectory and eventually approach the free-stream velocity value for downstream.

From these remarks it is obvious that an alternative approach should be considered such that the jet cross-sectional area is permitted to be an unknown in the governing equations. In order to do this it is necessary to have another equation to solve along with the continuity and n-momentum equations. The equation expressing conservation of momentum along the trajectory satisfies this need. By using this additional momentum equation, a more natural description of the jet flow properties is obtained as illustrated in Figure 4.

Although the area assumption is to be discarded, it is still necessary to provide information concerning the width of the jet in

order to calculate drag and shear stress terms in the governing equations. One approach is to follow Abramovich[19] and assume the growth of the jet width along the trajectory using an empirical expression based on limited experimental data. Another approach is to specify a shape for the jet cross section, and use this with the computed area to calculate the jet width. This latter approach is more appealing because it is easier to justify its use on the basis of available experimental data. Keffer and Baines[16], for example, have shown that a jet initially having a circular cross-section transforms to a "kidney" shape as the jet penetrates into the cross flow. This shape remains approximately the same with increase in s as illustrated in Fig. 5.

Prior attempts by researchers at approximating the jet cross-section have been limited to the elliptical shape, where the circle is a degenerate case. Hirsh[29], for example, approximated the jet cross section as a circle, which was a useful assumption in his development because then he assumed the jet flow to be axisymmetric. It would appear that the ellipse would be a more suitable approximation, particularly near the injection point where the jet flow is deformed by the large pressure and shear stress fields. An ellipse with a major-to-minor axis ratio of 5:1 was employed in Ref. 19, and later in Refs. 23-25, while Ref. 26 assumed a 4:1 ellipse. The approximation used in Ref. 26 had the added advantage of accounting for the change from the circular shape at the jet exit to the 4:1 ellipse at a specified point along the trajectory.

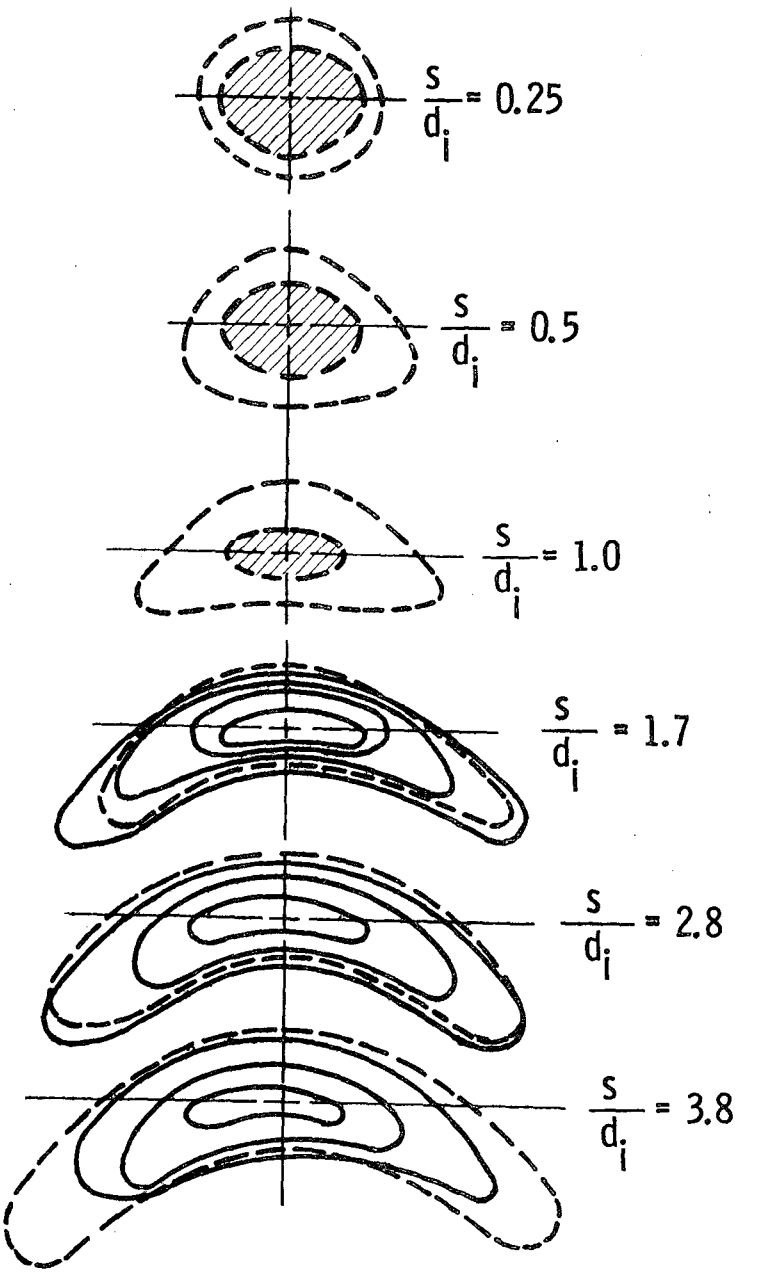

Figure 5.- Cross-sectional pressure contours of a jet injected normally into a cross flow, $V_j/V_\infty = 2.2$ (after Abramovich[19]); solid and dashed lines represent lines of constant total and static pressure, respectively, and the shaded areas indicate the potential core region.

For the present study, the jet cross-section shape is assumed to be elliptical with a ratio of major-to-minor axes of 5 to 1, the major axis being the jet width. It is also assumed that at the injection point (s = 0) the elliptical area is equal to that of a circle with diameter d_i. The change of jet width, h, along the trajectory is accounted for by the expression,

$$h = \sqrt{\frac{20\ A}{\pi}} \tag{28}$$

The change in h with distance along the trajectory was calculated with the present theory and is shown in Fig. 6 compared to experimental data obtained from Kamotani and Greber[18]. The data points from Ref. 18 were obtained from contours of constant velocity normal to a jet cross section, where the velocity excess had decreased to 10% of the maximum excess. The theory predicts the trend of increase in h/d_i with increase in s/d_i, although the predicted values are higher than the measured values at large s/d_i. The small effect of VR on h/d_i near the injection point is reflected by the theory. The empirical expression used by Abramovich[19] in his theory is shown for comparison.

The value of C_{D_n} associated with the 5:1 elliptical shape is taken to be 1.6 in keeping with the equivalent "solid" body argument and is assumed to be independent of the Reynolds number of the flow over the ellipse (Re_d). Wooler et. al.[26] used a value of 1.8 in their analysis, while Abramovich[19] used 3.0, a value which was pointed out by

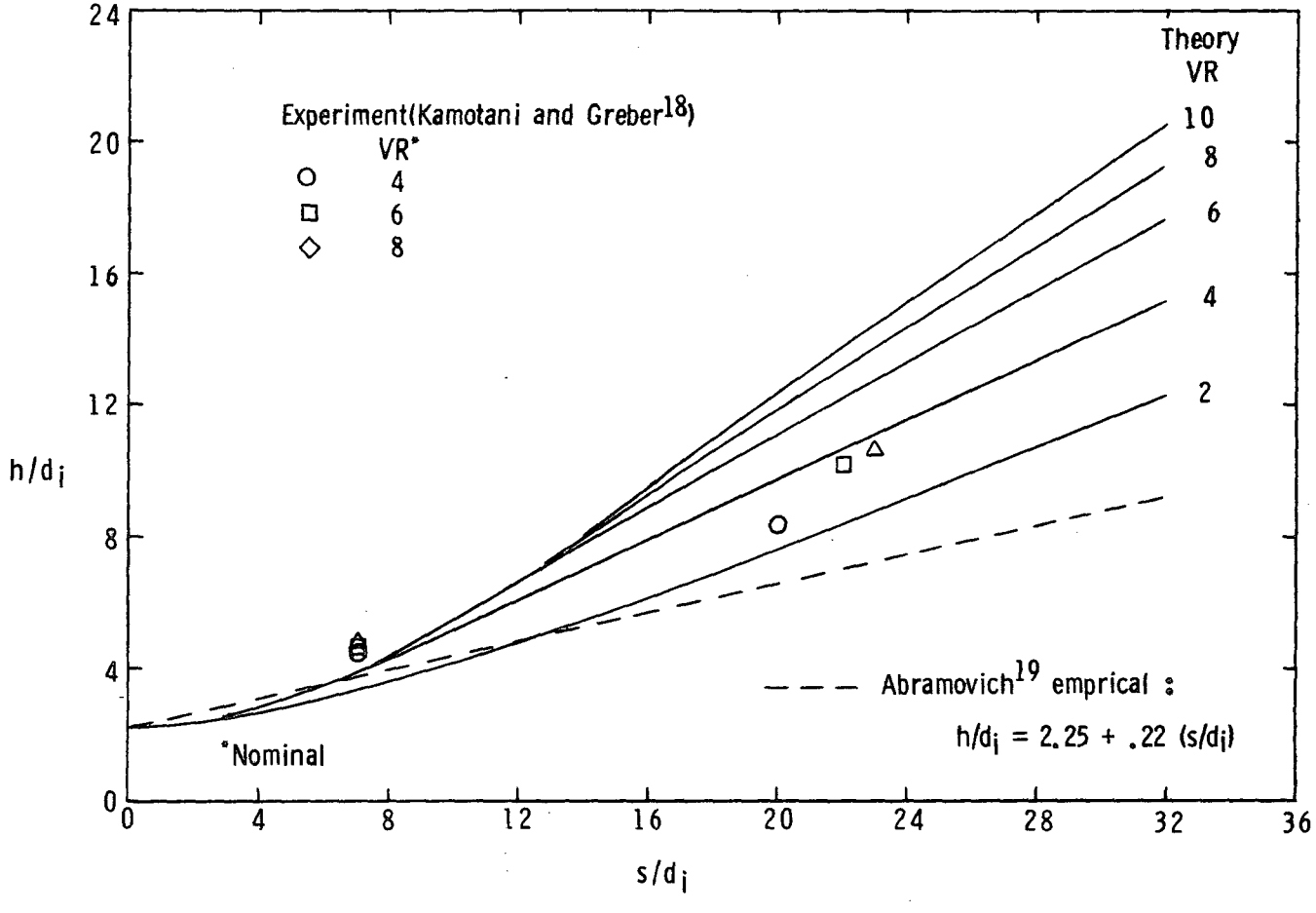

Figure 6.- Variation of jet width with distance along trajectory for a range of injection velocities; $\alpha_i = 90^\circ$, $T_i/T_\infty = 1.0$.

Schetz and Billig[23] as being totally unrealistic. An indication of how sensitive the theory is to the choice of cross-section shape and blockage coefficient can be seen in Figure 7 where experimental and theoretical trajectory results are compared for VR = 4.0. The effect of changing ellipse-axis ratio is presented in part (a) where $C_{D_n} = 1.6$ is used in the theoretical calculations, while the effect of varying C_{D_n} for a specific ellipse-axis ratio (5:1) is shown in part (b). As noted, increasing either ellipse-axis ratio or blockage coefficient results in progressively lower theoretical trajectories. The trends discussed here for the case of VR = 4.0 are typical of other injection velocities. The fact that the theoretical results obtained with $C_{D_n} = 1.8$ (Fig. 7(b)) are in better agreement with the experimental trajectories than the results obtained with $C_{D_n} = 1.6$ is misleading. It will be demonstrated later (Fig. 47) that the theory estimates mass flows in the jet that are too low, so that if this disparity was corrected the results obtained with $C_{D_n} = 1.6$ would show improved agreement with the experiment.

s-momentum

The s-momentum equation is obtained by taking the s-components of the various vector quantities in Eq. (10). The resulting expression represents a balance between the rate of change of jet momentum and the forces on the jet due to changes in mean jet pressure, to buoyancy

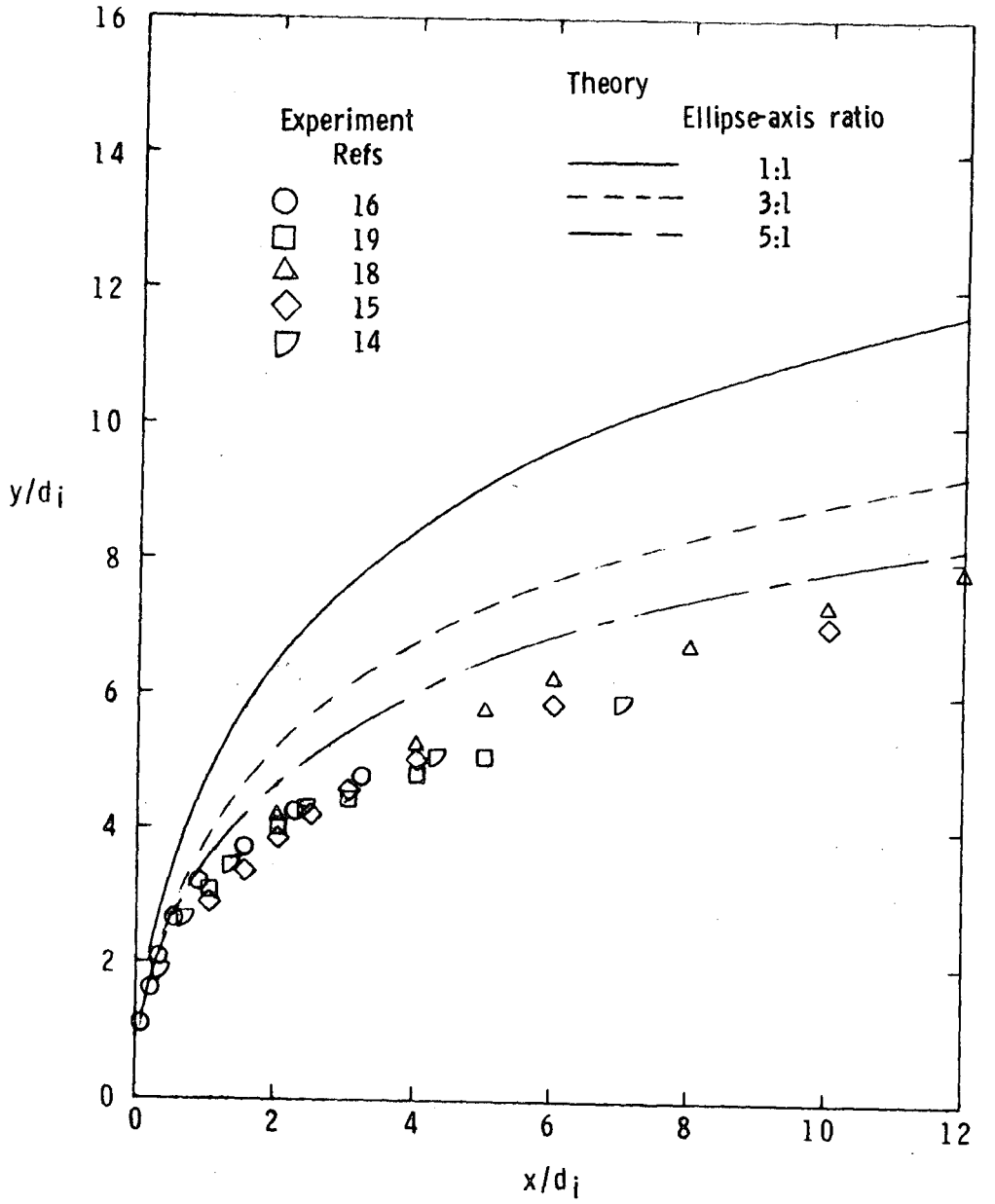

(a) $C_{D_n} = 1.60$.

Figure 7.- Effect of jet cross-sectional shape and blockage coefficient on theoretical trajectories for VR = 4; $\alpha_i = 90^\circ$, $\beta_i = 0^\circ$.

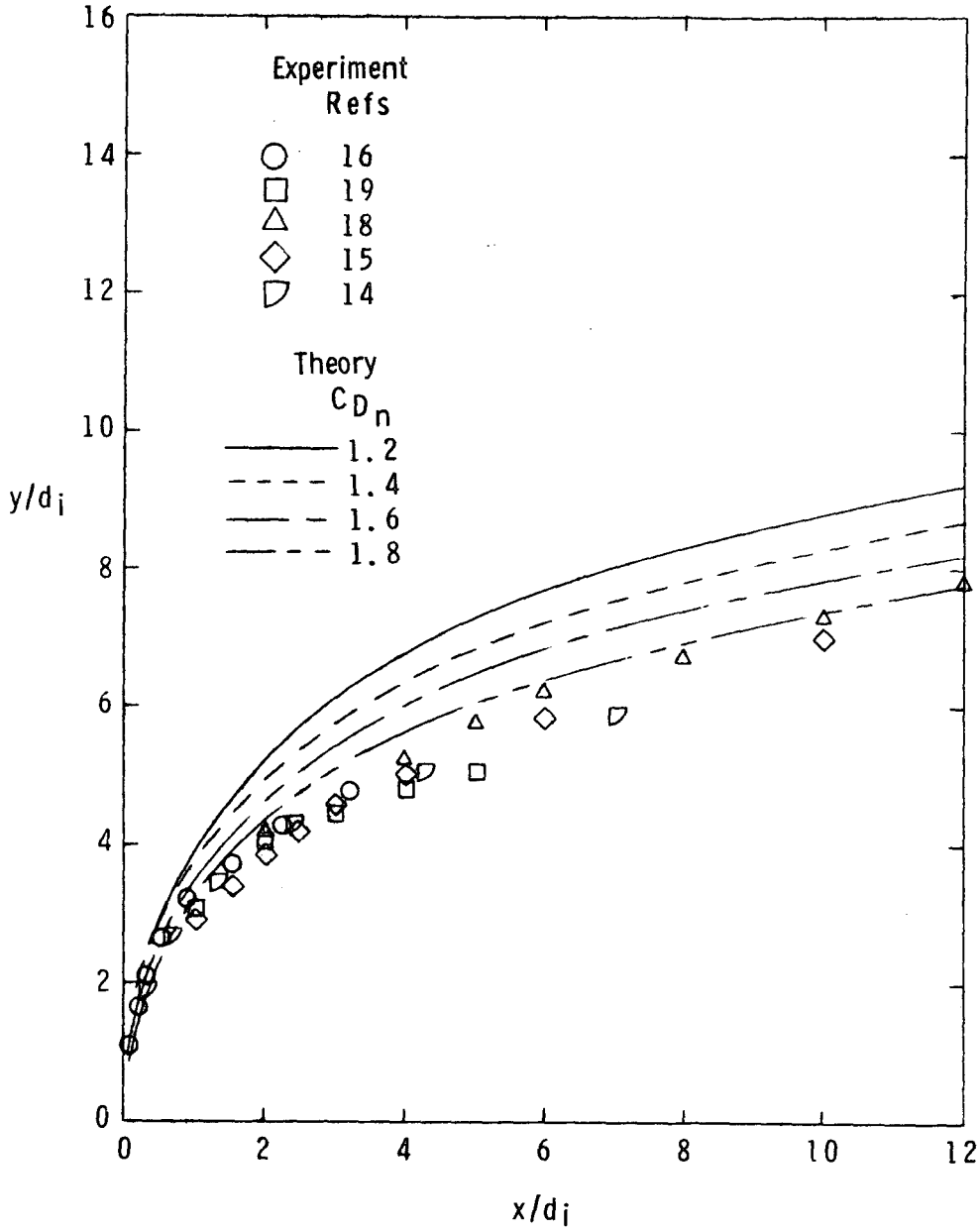

(b) 5:1 ellipse.

Figure 7.- Concluded.

caused by density differences between the jet and free-stream fluids, to entrainment of ambient fluid into the jet, and to shear stress between the jet and free-stream fluids.

In the s-direction the shear and pressure forces are not combined as they were in the n-direction. The appropriate pressure force acquired from Eq. (17) is,

$$F_{p_s} = - \iint_{(1)} p_\ell \, d\delta + \iint_{(2)} p_\ell \, d\delta - \iint_{(3)} p_\ell \, d\delta \quad (29)$$

where the local pressures are integrated over the control surface to get,

$$F_{p_s} = - \bar{p}_{(1)} A_{(1)} + \bar{p}_{(2)} A_{(2)} - \bar{p}_{(3)} A_{(3)} \quad (30)$$

A Taylor expansion can be performed to obtain the pressure and area at surface (2) in terms of the appropriate variables at surface (1), while $\bar{p}_{(3)}$ is taken to be the average of $\bar{p}_{(1)}$ and $\bar{p}_{(2)}$, and $A_{(3)}$ to be the difference between $A_{(1)}$ and $A_{(2)}$. Substituting these expressions into Eq. (30) and neglecting terms having higher orders of ds, the pressure force in the s-direction is found to be,

$$F_{p_s} = A \frac{\partial \bar{p}}{\partial s} ds \quad (31)$$

The force contribution of the surface stress tensor in the s-direction is approximated by,

$$\iint_{(3)} \tau_\ell \, d\delta = \tau \iint_{(3)} d\delta = \pi h \tau \, ds \qquad (32)$$

where τ_ℓ is the local shearing stress in the jet flow acting on the slanted surface of the control volume. The integrated local shear stress is represented by an average shear stress τ, which is assumed to act on a surface having the area $\pi h \, ds$. Although the physical problem is much more complicated than is described here, this approach will provide for a viscous force in the s-momentum equation, which has not been done in most of the previous studies using integral techniques.

The contribution of the net influx of momentum into the control volume to the force balance in the s-direction is obtained by performing the operations suggested by the third term in equation (10) and is found to be:

$$\iint \vec{V}(\rho_\ell \vec{V} \cdot \vec{e}_N \, d\delta) = \frac{\partial}{\partial s}(\rho A V^2) \, ds - E \, V_\infty (\vec{e}_x \cdot \vec{e}_s) \, ds \qquad (33)$$

The definition of averaged jet properties was used to derive this equation and the momentum flux entering the sloping surface of the control volume was represented by the rate that mass flows across the surface multiplied by the free-stream velocity component in the s-direction. Equations (31), (32), and (33) are combined with the body force term from Eq. (16) and the dot product expressions from Appendix B to obtain the s-momentum equation,

$$\frac{\partial(\rho A V^2)}{\partial s} = gA(\rho_\infty - \rho)\frac{dy}{ds} - A\frac{\partial \bar{p}}{\partial s} - \pi h \tau + E\, V_\infty \frac{dx}{ds} \qquad (34)$$

To evaluate the static pressure gradient along the trajectory, $(\partial\bar{p}/\partial s)$, the assumption is made that the free-stream static pressure field around the jet perimeter imposes itself on the jet flow. This is the usual type of assumption made concerning other free turbulent processes, such as jet injection parallel to a mainstream (coaxial flow) or jet injection into a reservoir (free jet flow). For the present case where the jet structure is considered as an elliptical cylinder inclined at an angle to the free-stream flow, there are large variations in the free-stream pressure field around the jet due to the blockage effect that the jet has on the free-stream flow. Some idea of the static pressure variation around the perimeter of a jet cross section, idealized as a circular cylinder, can be obtained by observing the experimental pressures in Fig. 8. An assumed pressure distribution to be used in the theory is also presented. As noted, the assumed pressures on the front of the cylinder ($0 \leq \theta \leq \pi/2$) are in functional form and were obtained from potential flow theory, while the pressures on the back of the cylinder ($\pi/2 < \theta \leq \pi$) are assumed to be equal to the free-stream pressure. Several researchers (e.g. Ramsey[17] and Kamotani and Greber[18]) have approximated the pressure field around the jet by examining the potential flow over various cylindrical shapes. Although the pressure field resulting from the turbulent jet injection process is very complicated and does not lend itself to be categorized

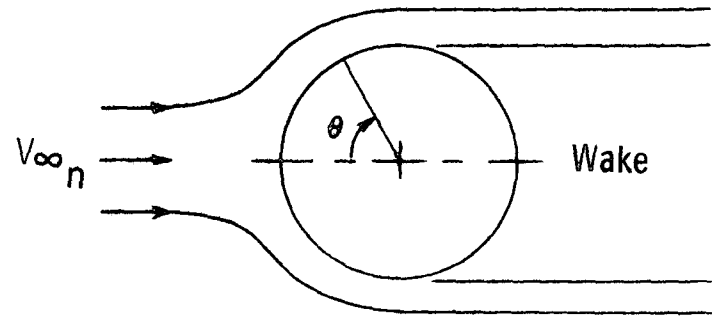

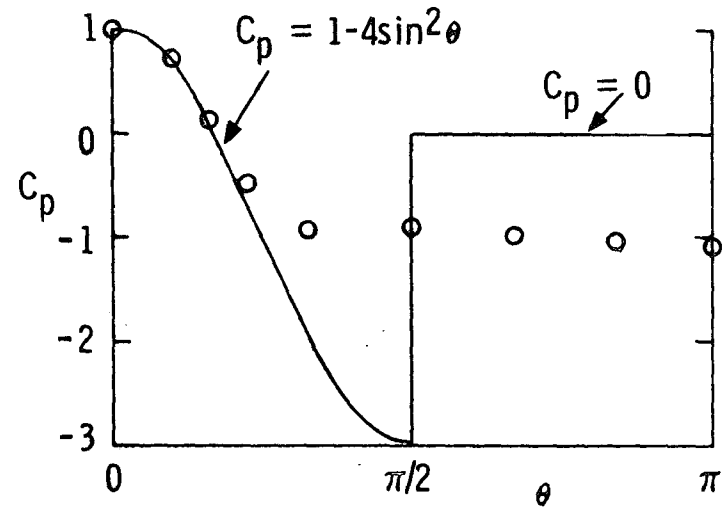

Figure 8.- Static pressure variation around the perimeter of a circular cylinder.

in this simple a fashion, the pressure variation in Fig. 8 is adequate for use in the present mathematical model. The local surface pressure $(C_p q_{\infty_n} + p_\infty)$ is used in the expression

$$\bar{p} = \frac{\int_0^\pi p \, d\theta}{\int_0^\pi d\theta} \tag{35}$$

to obtain the average static pressure acting on the cylinder. Performing the integrations in Eq. (35) using the pressure distribution shown in Fig. 8 we obtain,

$$\bar{p} = p_\infty - \frac{1}{2} q_{\infty_n} \tag{36}$$

where it is recalled that q_{∞_n} is the free-stream dynamic pressure normal to the trajectory (see Eq. (22)). This equation implies that the average static pressure on the jet cross section is less than the free-stream static pressure but approaches p_∞ as q_{∞_n} approaches zero. This occurs when V_∞ approaches zero and/or when the jet becomes parallel to the free-stream flow (i.e., $\alpha = 0$). Assuming that the average pressure imposes itself on the jet flow (i.e., the pressure in the jet flow becomes $\bar{p}$), $\bar{p}$ can be differentiated with respect to s to get:

$$\frac{d\bar{p}}{ds} = -q_\infty \left[R \frac{dR}{ds} \left(\frac{d^2x}{ds^2} \right)^2 + R^2 \frac{d^2x}{ds^2} \frac{d^3x}{ds^3} \right] \tag{37}$$

It is noted that if the jet trajectory is in either the vertical (x-y) or lateral (x-z) planes, the above expression for the pressure gradient simplifies to,

$$\frac{d\bar{p}}{ds} = -q_\infty (\sin \alpha)(\cos \alpha) \frac{d\alpha}{ds} \tag{38}$$

which is the form used by Campbell and Schetz[30].

One of the basic properties of a viscous fluid is that a velocity gradient or discontinuity in the flow results in a frictional shear stress. For the present case of a jet injecting into a cross flow, we envision the shear stress in the s-direction to be proportional to the differences between the jet velocity and the free-stream velocity component tangent to the jet flow. These shear stress can be approximated by,

$$\tau = \rho(\nu + \varepsilon) \frac{\partial U}{\partial n} \tag{39}$$

where U represents a velocity in the s-direction and $\frac{\partial U}{\partial n}$ represents the gradient of that velocity in the n-direction. The kinematic viscosity (ν) will be neglected for the present study since, for turbulent mixing flows, it is small compared to the virtual (eddy) viscosity, ε. The method used to estimate the eddy viscosity for this jet injection process is based on Prandtl's hypothesis[32] and is valid only for free turbulent flows. The viscosity is represented by,

$$\varepsilon = K_1 b(U_{max} - U_{min}) \tag{40}$$

where K_1 is an empirical constant and b is the width of the mixing zone. The minimum velocity is defined as the free-stream velocity component tangent to the direction of the jet flow (V_{∞_s}), while the maximum velocity is defined as the mean jet velocity in order to be compatible with previous mean flow assumptions. This representation is illustrated in Fig. 9.

The velocity gradient is approximated by,

$$\frac{\partial U}{\partial n} = \frac{U_{max} - U_{min}}{b} = \frac{(V - V_\infty \frac{dx}{ds})}{b} \tag{41}$$

so that the shear stress can be written as,

$$\tau = \rho K_1 (V - V_\infty \frac{dx}{ds})^2 \tag{42}$$

Incorporating the pressure gradient term, Eq. (37), and the shear stress term, Eq. (42), into equation (34) yields the final form of the s-momentum equation:

$$\frac{\partial(\rho A V^2)}{\partial s} = gA(\rho_\infty - \rho)\frac{dy}{ds} + q_\infty A\left[R\frac{dR}{ds}\left(\frac{d^2x}{ds^2}\right)^2 + R^2\frac{d^2x}{ds^2}\frac{d^3x}{ds^3}\right]$$

$$- \pi h\rho K_1 (V - \frac{dx}{ds} V_\infty)^2 + E V_\infty \frac{dx}{ds} \tag{43}$$

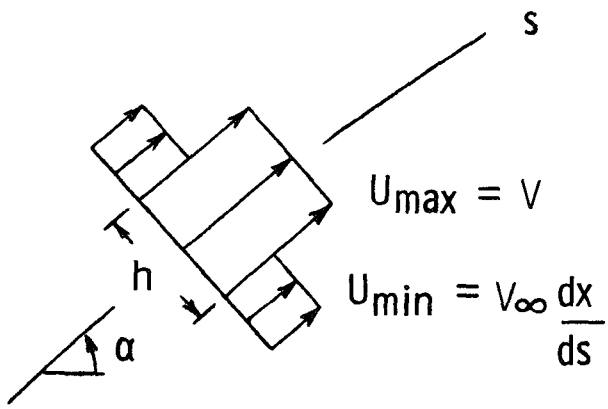

Figure 9.- Representation of velocities used to estimate shear stress in s-direction.

In order to obtain an estimate for the empirical constant K_1, it is necessary to rely on existing information related to less complex turbulent flows than the transverse jet injection process considered in the present study. The procedure used here is to estimate K_1 at the beginning of the injection by assuming that a two-dimensional free jet boundary exists between the jet velocity and the free-stream velocity component tangent to the jet flow. Schlichting's description of a free-jet boundary is used to obtain the expression,

$$K_1 = \frac{0.00137}{c\lambda} \tag{44}$$

where c is the rate of spread of the mixing zone and λ is a velocity parameter. Although c might be expected to be a function of both s and V_i/V_∞, it is assumed to be a constant for the present study. The value of c is taken to be 0.32 which is more representative of the rate of spread observed for the experimental data in Fig. 6 than is Abramovich's value of 0.22.

The velocities U_{max} and U_{min} in the analysis of the free-jet boundary are considered to be constant as the jet proceeds away from the point of initial flow interaction. In the present situation, U_{max} and U_{min} continuously change as the jet flow is decelerating and bending over. Accordingly, the velocity parameter used in Ref. 32 is re-defined as,

$$\lambda = \frac{V - V_\infty \frac{dx}{ds}}{V + V_\infty \frac{dx}{ds}} \tag{45}$$

which forces K_1 to be dependent on the local velocity conditions along the trajectory. It is noted that at the initial point of a normal injection $\lambda = 1.0$ which is the value Schlichting uses in his discussion. Equation (44) is used until K_1 attains the following value prescribed by a circular free-jet analysis[32]:

$$K_1 = \frac{0.00217}{c} \tag{46}$$

This description of K_1 is assumed to apply for the remainder of the jet's trajectory. An example of the variation of K_1 along the trajectory is shown in Figure 10 for several injection conditions.

t-momentum

The t-momentum equation is obtained by taking the t-components of the various vector quantities in Eq. (10). The resulting expression represents a balance of forces on the control volume due to buoyancy, to blockage of the free-stream flow, and to entrainment of ambient fluid into the jet. Similar to the derivation of the n-momentum equation, the pressure force is combined with the shear stress integrated over surface (3) to obtain the total drag force (D_t) acting on the jet in the t-direction. Accordingly,

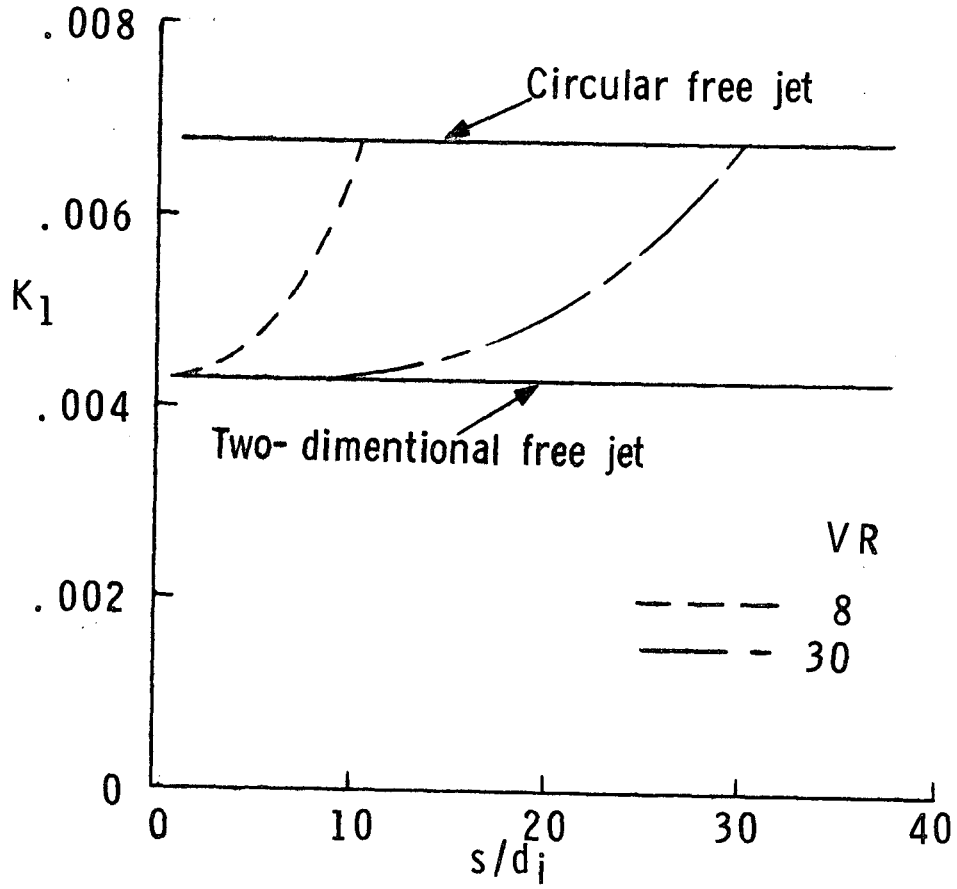

Figure 10.- Variation of empirical constant K_1 along the trajectory for several injection conditions; $\alpha_j = 90^o$, $\beta_j = 0^o$.

$$D_t = C_{D_t} q_{\infty_t} S_t \tag{47}$$

where

$$q_{\infty_t} = q_\infty (\vec{e}_x \cdot \vec{e}_t)^2 \tag{48}$$

If the jet cross-section were circular, then C_{D_t} would equal C_{D_n}, and S_t would equal S_n. However, since the shape is elliptic and not circular, then $C_{D_t} \neq C_{D_n}$ and $S_t \neq S_n$. Recalling that the elliptical shape has an axis ratio of 5 to 1, we have $S_t = \frac{h}{5}\, ds$ so that

$$D_t = C_{D_t} q_\infty (\vec{e}_x \cdot \vec{e}_t)^2 \frac{h}{5}\, ds \tag{49}$$

where C_{D_t} is taken to be 1.0.

The net flux of momentum in the t-direction entering through the sloping surface of the control volume is represented by the rate at which mass flows across the surface multiplied by the free-stream velocity component in the t-direction. This results in,

$$\iint \vec{V}(\rho_\ell \vec{V} \cdot \vec{e}_t\, d\delta) = E\, V_\infty (\vec{e}_x \cdot \vec{e}_t)\, ds \tag{50}$$

The body force term from Eq. (16) is combined with Eqs. (49) and (50) to obtain the t-momentum equation:

$$gA(\rho_\infty - \rho)(\vec{e}_y \cdot \vec{e}_t) + C_{D_t} \frac{h}{5} q_\infty (\vec{e}_x \cdot \vec{e}_t)^2 + E\, V_\infty (\vec{e}_x \cdot \vec{e}_t) = 0 \qquad (51)$$

After substituting for the dot products (Appendix B), the torsion (τ_o) associated with the trajectory is arranged so that it is in the numerator of the terms. The reason for this section is that τ_o is expected to have a small value for the present study ($\tau_o = 0$ for a two-dimensional trajectory). The resulting expression is,

$$\begin{aligned}
&\tau_o gA(\rho_\infty - \rho) \frac{dR}{ds} \frac{d^2y}{ds^2} + \tau_o gA(\rho_\infty - \rho)\, R \frac{d^3y}{ds^3} + \tau_o \frac{gA}{R} (\rho_\infty - \rho) \frac{dy}{ds} \\
&+ C_{D_t} q_\infty \frac{h}{5} \left(\frac{dR}{ds}\right)^2 \left(\frac{d^2x}{ds^2}\right)^2 + C_{D_t} q_\infty \frac{h}{5} R^2 \left(\frac{d^3x}{ds^3}\right)^2 + C_{D_t} \frac{q_\infty h}{5R^2} \left(\frac{dx}{ds}\right)^2 \qquad (52) \\
&+ \frac{2}{5} C_{D_t} q_\infty h\, R \frac{dR}{ds} \frac{d^2x}{ds^2} \frac{d^3x}{ds^3} + \frac{2}{5} C_{D_t} q_\infty h \frac{dx}{ds} \frac{d^3x}{ds^3} + \frac{2}{5} C_{D_t} q_\infty \frac{h}{R} \frac{dR}{ds} \frac{d^2x}{ds^2} \frac{dx}{ds} \\
&+ \tau_o E\, V_\infty \frac{dR}{ds} \frac{d^2x}{ds^2} + \tau_o\, E\, V_\infty R \frac{d^3x}{ds^3} + E\, V_\infty \frac{\tau_o}{R} \frac{dx}{ds} = 0
\end{aligned}$$

For the case where the jet follows a two-dimensional path, the t-momentum equation is an identity (see Appendix C), and hence its use is not necessary in the procedure for obtaining a solution of the jet trajectory and flow properties.

Heat Energy

Until this point only the mass and momentum aspects of the jet injection process have been discussed, however, since the present investigation is concerned with heated discharges, it is necessary

to also consider appropriate methods of describing the thermal characteristics of the flow. In particular, it is advantageous to determine the change in mean jet temperature resulting from the penetration of the jet into the cross flow. This can be accomplished by monitoring the heat loss from the control volume, this heat loss resulting from several heat-transfer mechanisms.

The first type of heat-transfer mechanism pertains to the reduction in energy content per unit volume ($\rho c_p T$) of the jet fluid due to the entrainment of free-stream fluid at a different energy level $(\rho c_p T)_\infty$. Applying this concept to the control volume results in the expression,

$$(m\ c_p\ T)_2 = (m\ c_p\ T)_1 + m_e(c_p\ T)_\infty \tag{53}$$

where $(mc_pT)_1$ represents the energy level in the control volume that would exist if there were no entrainment, and $(mc_pT)_2$ represents the equilibrium energy level resulting from the complete mixing of the jet and entrained fluids. Since the specific heat (c_p) of water is fairly insensitive to temperature changes, the various specific heats in Eq. (53) are assumed to have the same value.

Forced convection, the second type of heat transfer mechanism being considered, results when the free stream flows around the heated jet fluid and extracts heat energy from the jet in the process. This heat transfer is analogous to the forced convection in separated flow over a heated cylinder, where the cylinder is cooled by the fluid

flowing normal to the cylinder's axis. To be consistent with our previous arguments, the convective heat transfer is estimated by considering the jet structure as a cylinder inclined at an angle to the free-stream flow.

Eckert and Drake[33] give several examples of film heat-transfer coefficients occurring in this type of flow situation and suggest the following expression for estimating an average Nusselt number:

$$Nu_d = 0.43 + 1.11\ \psi\ (Re_d)^{\xi}\ (Pr)^{0.31} \tag{54}$$

Values of Prandtl number for water at different temperatures were obtained from tables in Ref. 33 for use in the above expression. The Reynolds number is defined using the "effective" diameter of the jet as the reference length and the free-stream velocity component perpendicular to the jet axis as the reference velocity, so that Nusselt number will be sensitive to the changes in local flow conditions as the jet penetrates into the crossflow. The Reynolds number is thus,

$$Re_d = \frac{\rho_\infty V_{\infty_n} d}{\mu_\infty} = \frac{d\ V_\infty R}{\nu_\infty} \frac{d^2x}{ds^2} \tag{55}$$

For vertical or lateral injection this reduces to,

$$Re_d = \frac{d\ V_\infty}{\nu_\infty} \sin(\alpha) \tag{56}$$

The values of Re_d occurring in the present study suggest the selection of $\psi = 0.45$ and $\xi = 0.50$ for use in Eq. (54).

The definition of Nusselt number ($\bar{h}d/k$) is used to obtain the average film heat-transfer coefficient ($\bar{h}$) which yields the rate of heat loss from the jet fluid,

$$Q = \bar{h}\, B(T_\infty - T) \tag{57}$$

where B denotes the cylindrical area of the jet control volume. This, in turn, results in a temperature change in the jet flow due to this convective heat loss.

An example of the temperature results obtained when these two heat-transfer mechanisms are incorporated into the analytical model is shown in Fig. 11, where the theoretical calculations were made with the same injection conditions as the data with VR = 5.2. The trend of temperature decrease along the trajectory measured in the present study is adequately estimated by the theory, the predicted average temperature values falling below the measured maximum temperatures. These results are substantiated by the temperature data for air injection processes measured by Ramsey[17] and Kamotani and Greber[18]. The theoretical temperatures obtained by considering only the effects of entrainment are presented to demonstrate the relative magnitudes of the two types of heat-transfer mechanisms. Convection is seen to be the dominant mechanism for determining

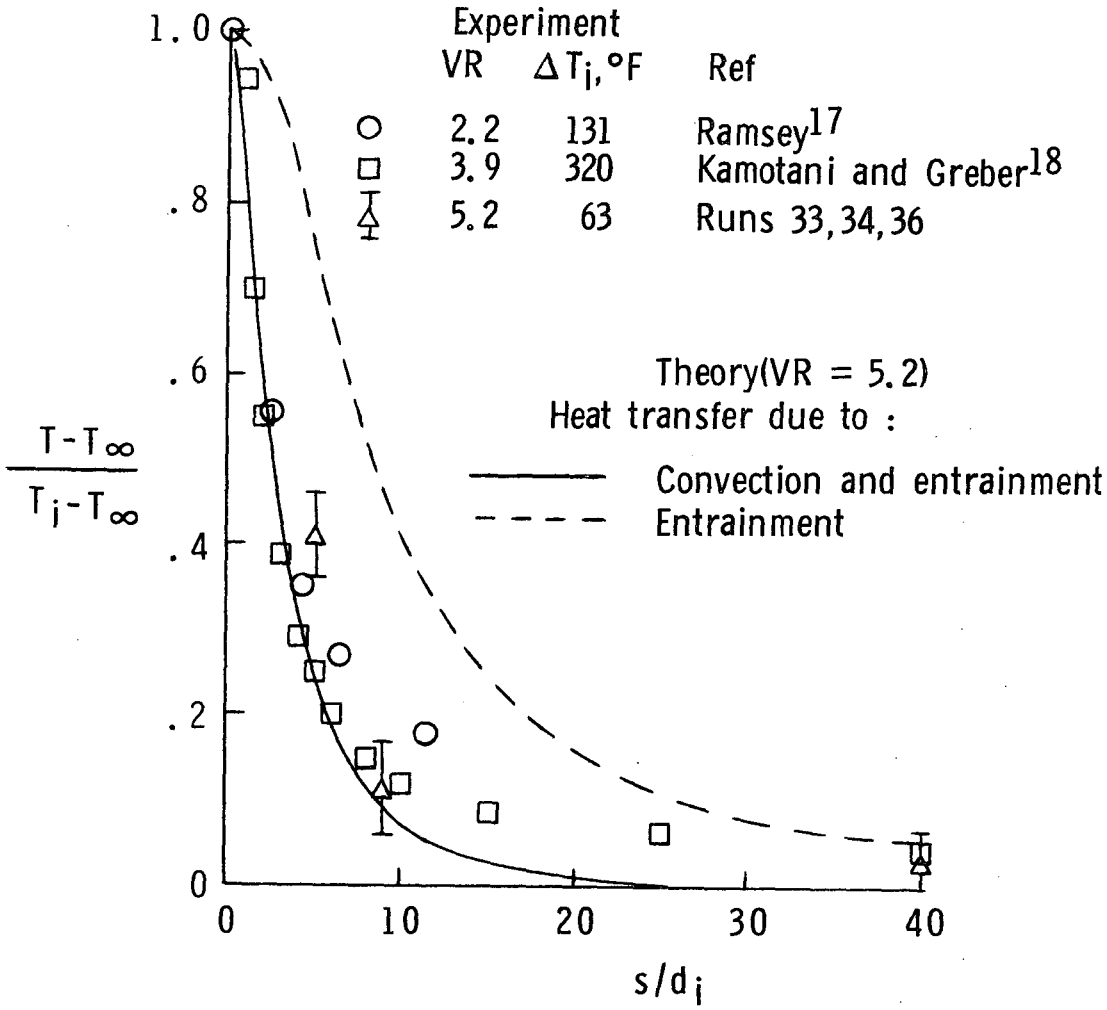

Figure 11.- Variation of jet temperature with distance along trajectory for heated injection process; $T_i > T_\infty$.

temperature loss in the early stages of the jet injection process, while the effects of entrainment become dominant as the jet proceeds downstream.

Solution Procedure

An iterative method is employed to obtain a numerical solution of the highly nonlinear governing differential equations at specific locations along the jet trajectory. Appendix C shows how the s,n, and t-momentum equations are non-dimensionalized and put into the forms used in the numerical technique. It was found that the equations could be simplified somewhat by using direction cosines (u and w) as the dependent variables rather than x,y, and z. This means that at each point (j+1) on the trajectory a solution to this initial value problem involves determining values for u_{j+1}, w_{j+1}, ρ_{j+1}, A_{j+1}, and V_{j+1}.

The basic solution procedure is to solve the s-momentum equation for the jet momentum in the control volume, where the coefficients in that equation are estimated using the flow property values obtained from the solution at the previous location on the trajectory. The s-momentum is used in conjunction with the continuity equation to provide an update on V_{j+1} and the heat loss from the control volume is calculated to provide new estimates for T_{j+1} and ρ_{j+1}. The current flow property values are then used in the coefficients of the n-momentum equation to obtain a solution for $(du/ds)_{j+1}$, where a central difference scheme provides u_{j+2}. Information acquired from the s- and n-momentum equations is used to solve the t-momentum

equation for $(d^2w/ds^2)_{j+1}$, from which w_{j+2} is obtained using a central difference scheme. The most recently calculated values of the direction cosines and flow properties are used to iterate back through the governing equations, convergence to a satisfactory solution occurring in only a few iterations.

Incremental values of x, y, and z are obtained from the final value of trajectory slope and from the assigned value for Δs. These increments are added to the coordinates of the previous location on the trajectory to obtain new x, y, z trajectory coordinates. This procedure is repeated at each incremental "step" along the trajectory to provide a solution for the trajectory and cross-sectional area of the jet, as well as the jet flow properties of mass, velocity, momentum, and temperature. The theoretical results presented herein were obtained with a constant incremental step size of $0.01\ d_i$.

For the case where the jet path is two-dimensional the information from the t-momentum equation is redundant; therefore, it is only necessary to solve the s- and n-momentum equations, along with Continuity, to obtain the desired solution. This is amplified in Appendix C where further observations are made concerning the numerical solution of the governing equations.

IX. EXPERIMENT

The experimental portion of the present investigation was conducted in a water channel located in the Hydraulics Laboratory at Virginia Polytechnic Institute and State University. A description of the test hardware and the test results is presented in the following section.

Apparatus

Water supply

A centrifugal pump (1200 gal./min. capacity) was the primary source for providing the desired flow conditions in the water channel. The sketch in Figure 12 shows the path of the water after it has been extracted from the sump by the pump, the bulk of the water being directed through the 10" line back to the sump. The necessary water flow for the channel was bleed from the 10" line by a 2" supply line. A globe valve located on the 2" line upstream from the water channel was used to control the flow rate to the channel. The actual flow rate before and after a test sequence of the main stream was determined with a weigh tank and a stopwatch.

After the pump was started, the sump valve was adjusted to give a predetermined reading on a flow meter located on the 10" line upstream from the sump valve. This reading was used for all the tests using the pump so that repeating test conditions in the water channel would be possible. The centrifugal pump experienced problems with a foot valve after Run #37 (see test log in Chapter XIII), so that water flow

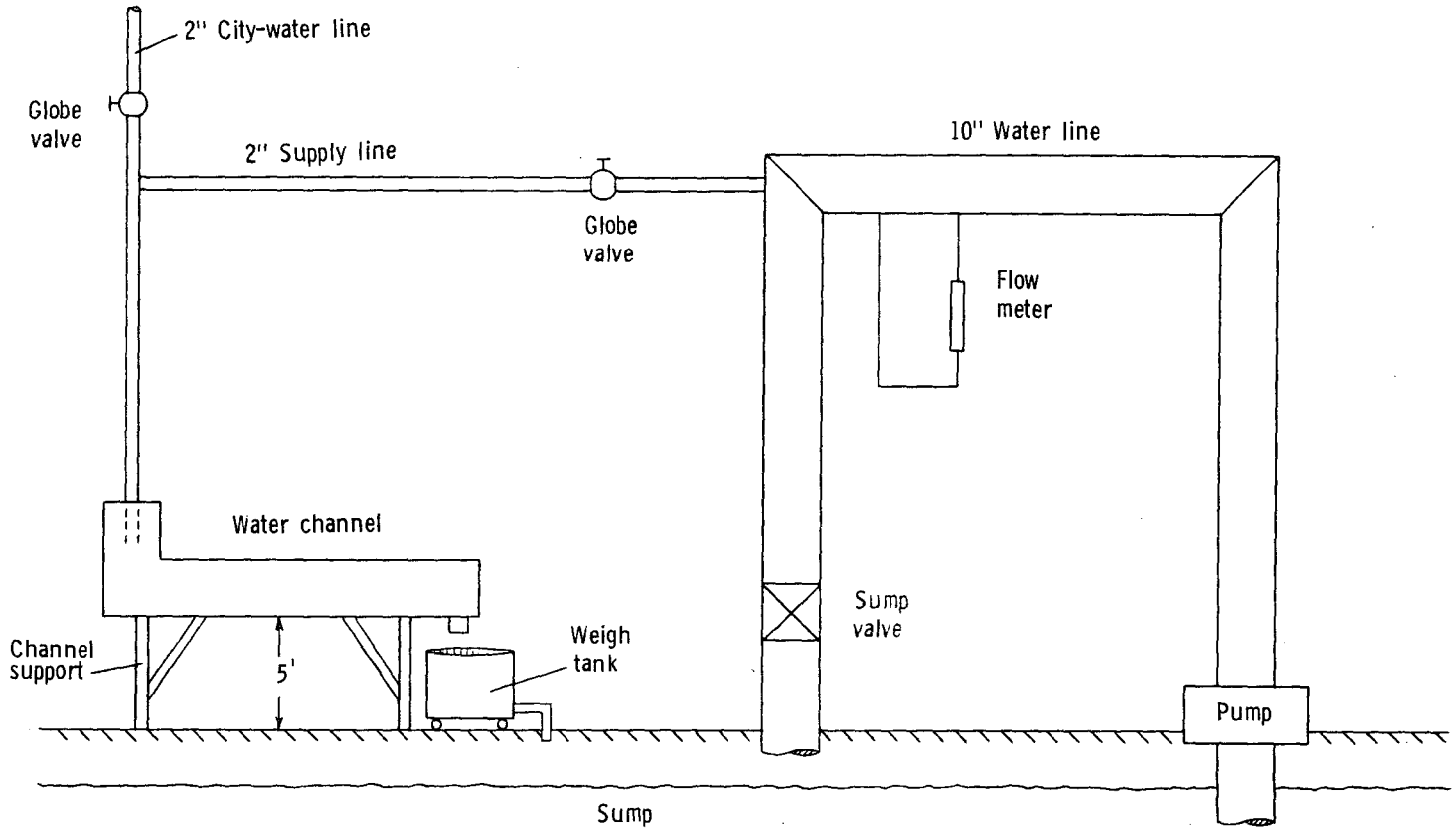

Figure 12.- Sketch of water circuit.

in the channel was provided by city water for the remainder of the tests. The water from both sources was at room temperature and was clear and bubble free, as the photographs to be presented subsequently will show. A flow diverter was provided at the discharge from the channel so that water could be routed either into the weigh tank and hence into the sump, or into a drain. This diverter facilitated the flow rate measurements and provided a way to prevent the returning of dyed water (resulting from the jet injection process) to the sump.

Main-flow channel

The main-flow channel was a Hydraulic Demonstration Channel, Serial 116221, by Hydraulic Design and Products Company, Minneapolis, Minnesota and was constructed of plexiglass throughout except for some of the support points which were made of aluminum. The passage of the channel consisted of a 6" x 12" cross section approximately 8 feet long (Figure 13). Because of influences on the flow near the entrance to and exit from the passage, the usable test area was restricted to the region midway between the entrance and exit stations. The channel was equipped with a sluice gate and weir both of which could be adjusted to alter the flow through the passage. The sluice gate was set so that the bottom of the gate was below the water level in the header, thus minimizing the number of air bubbles that passed through the gate to the channel's passage. The weir was adjusted to get the desired water depth at the jet exit stations.

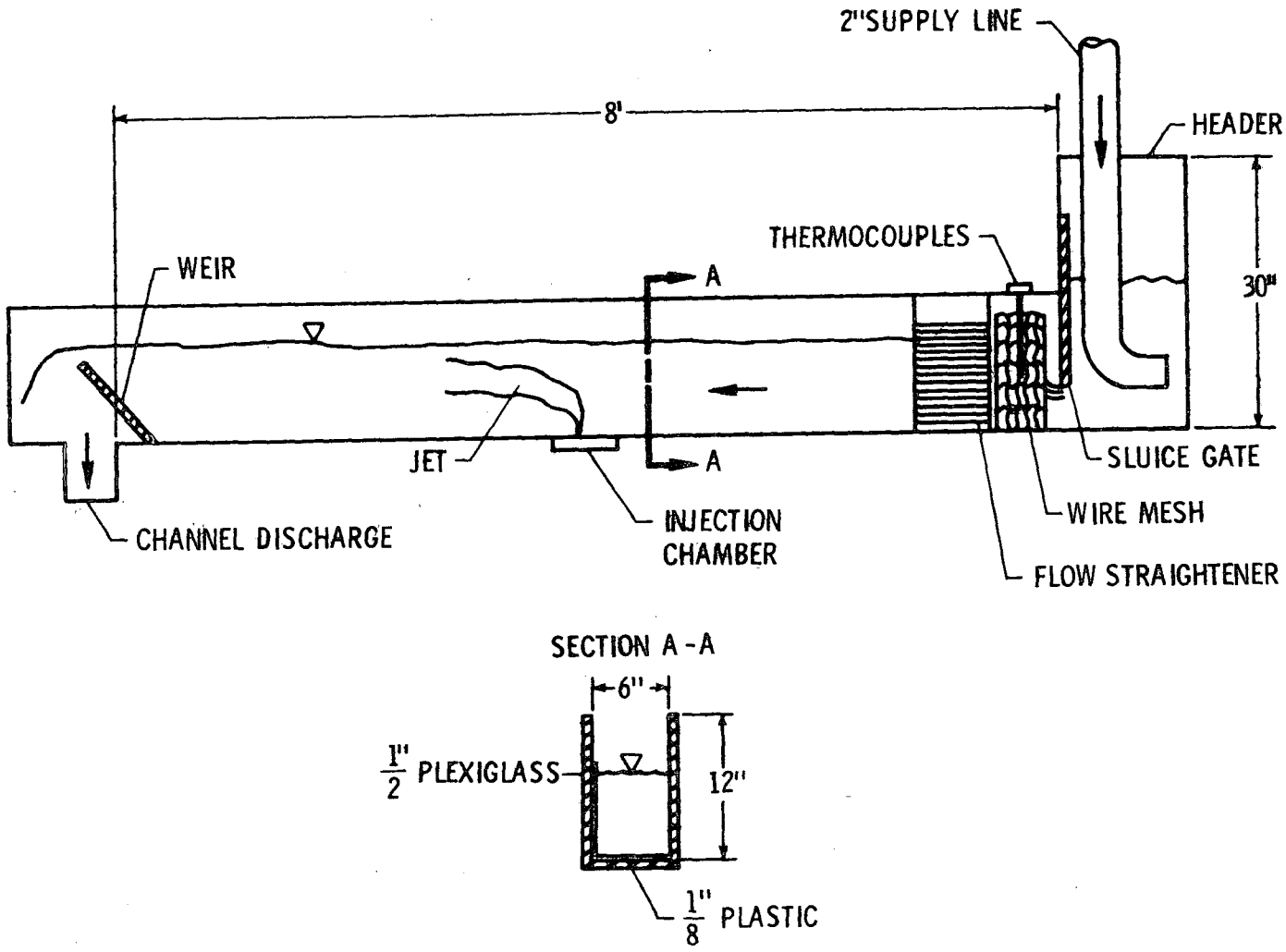

Figure 13.- Sketch of main-flow system.

Several arrangements were investigated for the discharging of the water from the 2" supply line into the header. Initially, a straight section of pipe was used to discharge the water into the header, but this arrangement resulted in very large disturbances in the flow in the test area of the passage. It was found that utilizing an elbow on the supply line so that the water is discharged towards the back of the header greatly reduced the disturbances noted in the channel. This is the arrangement shown in Figure 13 and was used throughout the tests.

The basic water channel was altered in several ways for use in the present experimental study. Flow visualization tests indicated that, even with the elbow on the supply line, some degree of flow angularity and disturbances existed in the vicinity of the jet exit station. A flow straightening system was installed just downstream of the sluice gate to alleviate this problem. The system consisted of several layers of 1/8 inch wire mesh followed by a unit which held a bank of plastic soda straws (1/4 inch in diameter). These straws were 3 inches long, arranged streamwise, and were retained fore and aft by window screening. Subsequent flow visualization tests indicated that this flow straightening system provided a flow near the jet exit station that had few disturbances and had no apparent flow angularity.

The second alteration was to drill 2.50-inch diameter holes through the bottom and one side of the channel 27 inches downstream of the flow straightener to permit insertion of the injection chambers. The third alteration was to cover the bottom and one side of the channel with 1/8

inch thick white plastic sheets that were ruled with 1-inch squares in black paint. Each of the lines in these squares was 1/16 inch in width.

Last, the channel was fitted with two instream copper-constantan thermocouples located upstream of the flow straightener but downstream of the sluice gate. One of these was used to measure the main flow, or free-stream, temperature while the second was used in conjunction with thermocouples in the injection chambers to permit direct measurement of the temperature difference between the injected and free stream fluids (ΔT_i).

Injection system

The various components of the injection system which control the flow rate and temperature of the injected fluid are shown in Figure 14. The injectant was water which was dyed with equal parts of red and green food coloring, 2 ounces per gallon. Propylene Glycol which has a specific weight of 64.8 lbf/ft^3 at 68°F, accounted for 15% of the food coloring volume.

An aluminum heating vessel 8" in diameter and 20" in length served as a reservoir for the injectant and had a fluid capacity slightly greater than 2-1/2 gallons. The fluid was driven from the heating vessel by means of air pressure (10 - 15 psig) which was controlled by a regulator. The water-flow rate was controlled by a needle valve and monitored with a Fisher-Porter P4 105711 flow meter. The tubing connecting the heating vessel to the flow meter and hence to the

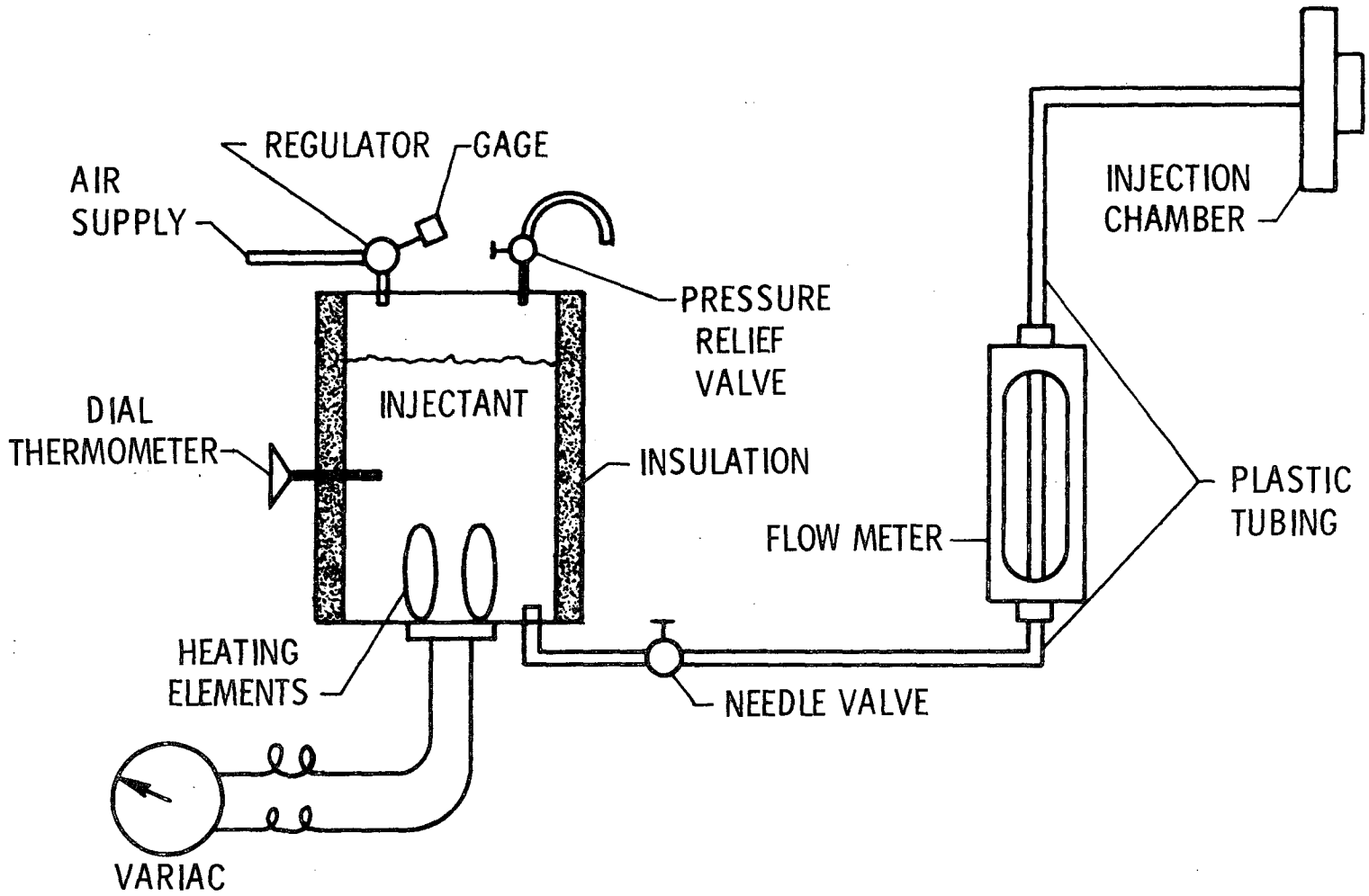

Figure 14.- Schematic of injection system.

injection chamber was 1/4 inch (o.d.) polyethylene to reduce heat loss. Heating of the injectant was accomplished electrically by a General Electric 150-watt immersion heater that was regulated by a Variac. Fiber glass insulation material was used to reduce heat loss from the vessel.

The injection chambers, machined out of solid lucite to minimize heat losses, were inserted through the channel wall and floor such that the surface facing the flow was flush with the white plastic surfaces. This is illustrated in Figure 15 which shows details of the wall injection chamber. A 9/16" flat bottomed hole was drilled to within 1/8" of the surface facing the flow, and a .0625" hole bored through to form the injection port. Two injection ports were used in the wall chamber during the duration of the experimental study; an injection port parallel to the chamber center-line was used for the lateral injection tests, and a port at a 45° angle to the center-line was used for the oblique injection tests. Both of these ports were located away from the chamber center-line so that a change in injection conditions could be obtained simply by rotating the injection chamber. For example, a change in vertical position for both ports was obtained by rotating the chamber, while an additional change in injection orientation occurred for the 45° port. The details of the injection chamber located in the channel floor are similar to those described for the wall chamber, except that the floor chamber had one 0.0595" injection port which was located on and parallel to the chamber center-line.

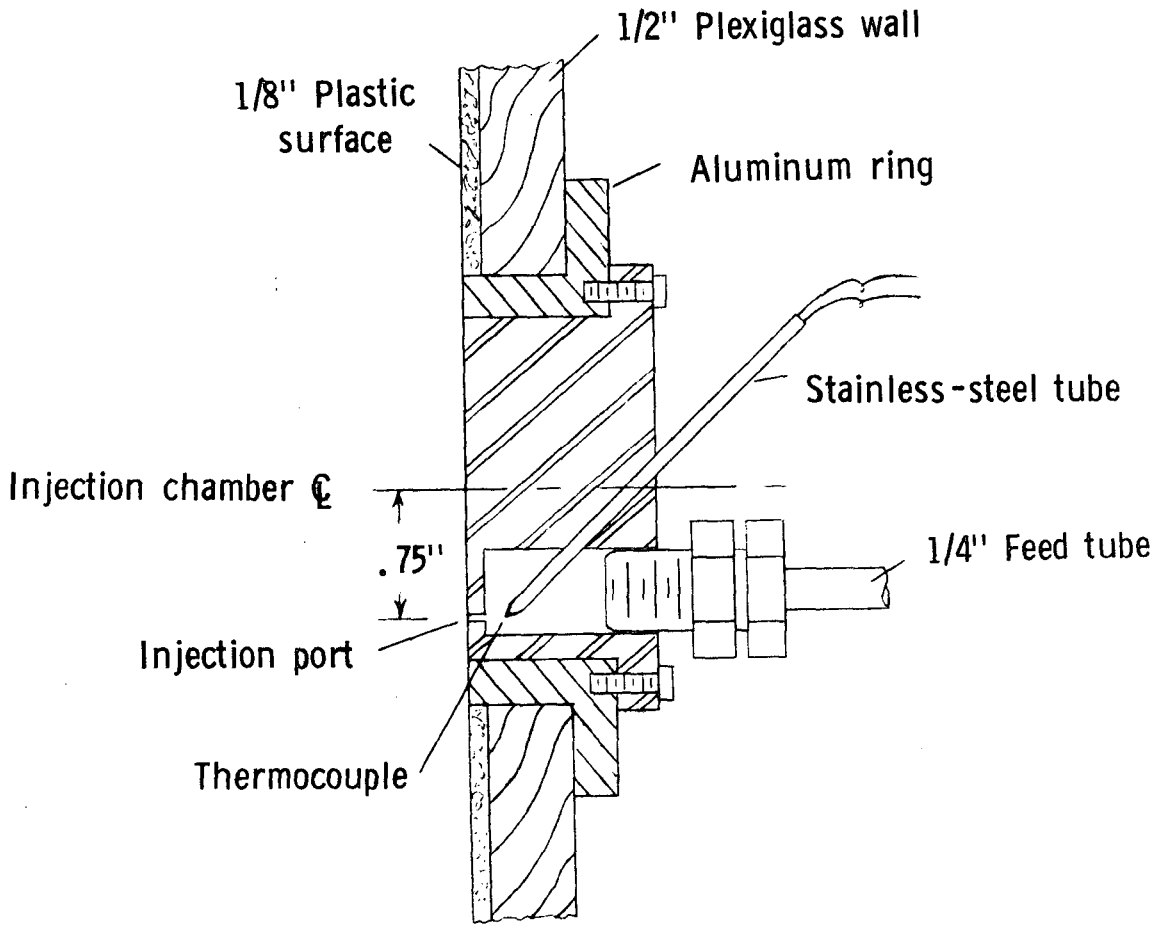

Figure 15.- Details of wall injection chamber used for lateral injection tests.

The outer portion of the 9/16" hole was tapped for 1/4" NPT for connection with the feed tube by means of a compression fitting. A 1/8" stainless-steel tube housing a copper-constantan thermocouple was inserted at approximately 45° from the outside into the 9/16 inch hole. This thermocouple measured the injectant temperature and was positioned so that it was about 1/4" from the injection port. It was connected with one of the thermocouples in the free-stream flow to directly read the temperature difference between the injectant and the free-stream fluid. All of the thermocouples were coated with a thin epoxy coating to avoid corrosion, and although the epoxy coating increased the response times, calibration showed the response to be more than sufficient for the type of tests conducted herein.

Instrumentation

The two thermocouples placed in the free-stream flow were encased in 1/8" stainless-steel tubes, similar to the arrangement used to measure injectant temperature. The outputs from these thermocouples were recorded on a Hewlett-Packard 7100B strip chart recorder. An electric ice junction by Joseph Kaye & Company was used to provide a reference for one of the thermocouples measuring free-stream temperature. The other thermocouple in the free-stream flow was connected with the thermocouple in the injection chamber by connecting the constantan leads of the two thermocouples together, and the respective copper leads to the recorder terminals. This arrangement allowed the direct measurement of the difference between the injected fluid and the free-

stream fluid. The millivolt output was converted to ^{o}F using a standard copper-constantan thermocouple calibration. Before each test sequence the outputs from the thermocouples were checked by using a beaker of water and an accurate thermometer.

Two Graflex 4-in. x 5-in. cameras were arranged above and to the side of the channel opposite the injection ports (see Fig. 16a) and were fitted with 127 mm, f/4.7, lenses. These lenses were operated at f/22, 1/400 sec to provide most of the photographic information obtained during the tests. Several photographs were obtained using a longer exposure (f/32, 1/15 sec) to provide a time-average of the fluid motion. For the free-stream velocities of this study, a fluid particle would move 3 to 6 jet diameters downstream during the long exposure. Illumination was accomplished with front lighting from a single 500-watt photo hood. Poloroid type 57, ASA 3000, film in sheet film holders was used by both cameras.

The requirement that the pictures be taken simultaneously by both cameras lead to the setup illustrated in Figure 16(b). Heavy duty 6-volt lantern batteries were used to provide the necessary current to a solenoid mounted on the side camera. By tripping the shutter on the top camera, a circuit is completed allowing the solenoid to trip the shutter on the side camera.

A calibration of the Fisher-Porter flow meter was performed because the flow meter was marked to read pounds per minute for a fluid with specific gravity of 1.32, and the injectant for the present study was predominantly water having a specific gravity of 1.0. The calibration

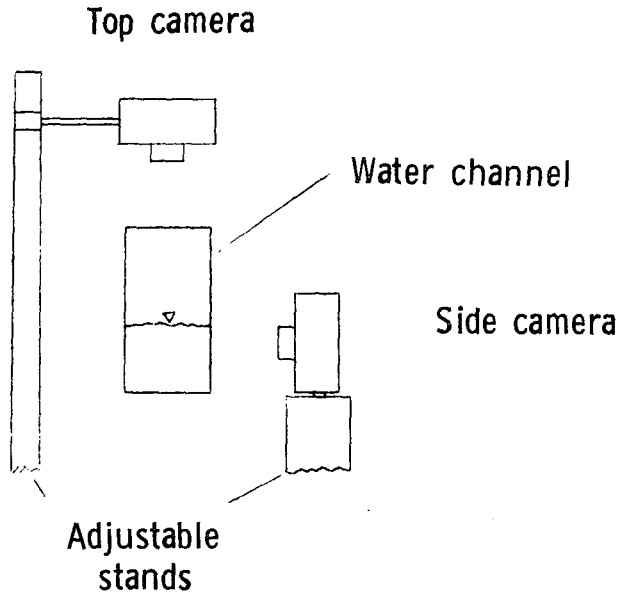

(a) Camera arrangement.

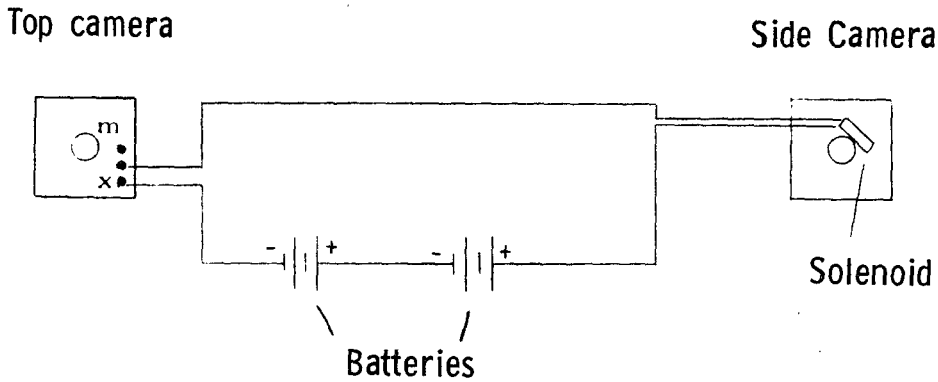

(b) Shutter arrangement.

Figure 16.- Schematic of camera arrangement and shutter operation.

was conducted for both the unheated and heated conditions of the injectant for a range of flow rates. The procedure was to adjust the needle valve to give a constant reading on the flow meter for a fixed period of time (usually 60 seconds), while collecting the injectant for a later temperature and weight measurement. The unheated injectant temperatures were about $70^{\circ}F$, and the temperatures of the heated injectant ranged from $125^{\circ}F$ to $148^{\circ}F$. The results of the calibration are presented in Figure 17 where the measured values for flow rate of the heated injectant are represented by the ticked symbols. Since no discernible trend of temperature on flow rate was observed, a curve was faired through the data to represent the calibration for all temperatures. This calibration curve was used for all test conditions and provided the values of $\dot{m}_i$ listed in the test conditions presented in Appendix A.

Tests

Experimental procedure

The procedure for obtaining the temperature and photographic information for a given injection test began with the establishment of the desired flow conditions in the water channel. The centrifugal pump was used to provide the necessary flow in the water channel for the lateral injection tests, while city water was used for the channel flow for the vertical and oblique injection tests. Several measurements were made of the flow rate in the water channel using the weigh tank, and the weir was adjusted to set the water depth of the main flow at the

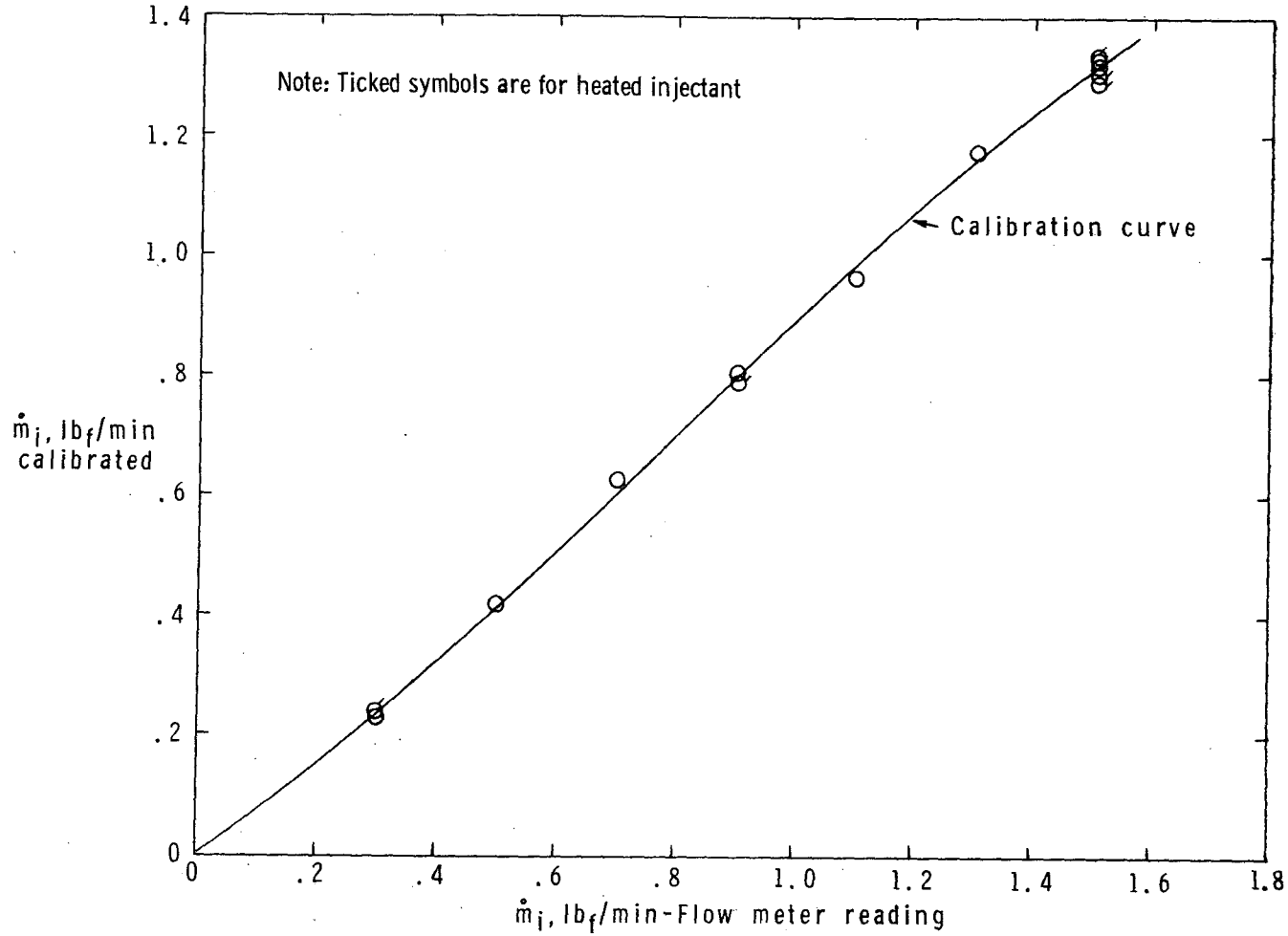

Figure 17.- Calibration of flow meter for heated and unheated injectant.

injection station at a certain value. This water depth was 2-15/16" for the lateral injection tests, and 4-13/16" for the vertical and oblique injection tests.

The injection system was checked to see that the heating vessel was supplied with an adequate amount of dyed injectant, and then the vessel was pressurized. If a heated jet test was to be conducted, approximately 15 minutes was necessary for the injectant to reach a desired temperature. The jet flow was turned on briefly to see that the flow meter and jet orifice were free from any restrictions, as well as to focus both cameras. When a test was ready to be conducted, the jet flow meter was set at a desired setting. If it was a heated injectant test, the needle valve was opened wide to 'purge' the injection system with the heated fluid, before setting it at the desired setting. The effects of increased injectant temperature on the jet flow characteristics were investigated by setting the flow rate of the jet at a fixed value regardless of the temperature of the injected fluid. As is shown in the test log in Appendix A, the resulting injection velocities are practically the same since the density of the injectant has only a small variation with temperature within the temperature range investigated.

When the photographs were taken simultaneously with the two cameras the strip chart was marked so that the temperature readings would coincide with the photographs. The strip chart recorded continuous readings of the two temperature measurements. The values of T_∞ and ΔT_i shown in the test log were those values read off the strip chart at

this point.

Test conditions

The tests were conducted for the submerged injection of the jet fluid into the main flow in three ways. These will be referred to as lateral, vertical, and oblique injection throughout the report. A cartesian coordinate system is defined such that the x axis is parallel to the direction of the free stream flow, and the y axis is in the vertical direction (i.e. in line with the gravity force). The z axis is the perpendicular to both the x and y axes. The orientation of the jet's axis at the injection point is defined by using the angles α_i and β_i, where α is the angle between the jet axis and the x axis, and β is the angle between the jet axis and the y axis. The angular orientation of the jet axis is shown in Table II for the different injection situations, the jet fluid being injected perpendicularly into the main stream for the lateral and vertical injection cases. The vertical distance of the injection port from the channel floor (a) and the horizontal distance from the flow straightener (L) are defined in Figure 18 to aid in describing the locations of the ports in the water channel. These distances are listed in the test conditions that are tabulated in Appendix A.

The different orifice locations for the lateral and oblique injection cases were obtained by rotating the wall injection chamber. For lateral injection, this gave the effect of changing the distance from the jet flow to the free surface of the main flow. For oblique

injection, this completely changed the orientation of the injected jet with respect to the main flow, as evidenced by the α_i and β_i values shown in Table II. Only one orifice location was investigated for the vertical injection case and it was located on the channel floor mid-way between the two channel walls.

TABLE II.- Angle of jet axis at injection point.

Injection	α_i	β_i	Orifice
Lateral	90°	90°	1 and 2
Vertical	90°	0°	3
Oblique	90°	50°	4
	140°	90°	5
	40°	90°	6

The experimental tests were conducted for the injectant having a range of injection velocities and temperatures, and the resulting test conditions are presented in tabular form in Appendix A. Each test is assigned a Run number for easy identification with the experimental results presented in the text. The tables list the measured values for the mass flows of the jet and free-stream flows, and for the temperatures of the jet and free-stream fluids. An explanation of how the other properties are deduced from the measurements is included in the appendix. The reader should note that the values for velocity ratio (VR) and temperature difference (ΔT_i) presented in the text are "rounded off" versions of the values listed in the tables.

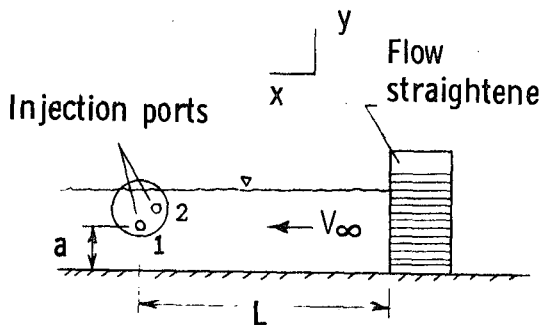

Orifice	a	L
1	1.25	27.00
2	1.90	26.10

(a) Lateral injection.

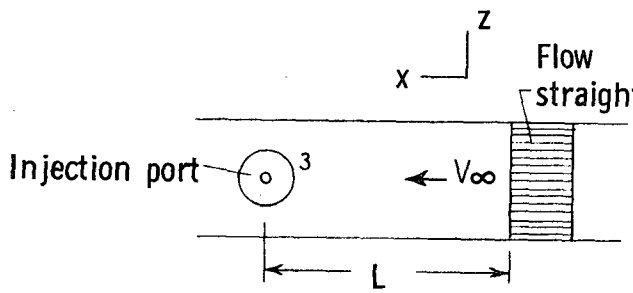

Orifice	a	L
3	0	26.90

(b) Vertical injection.

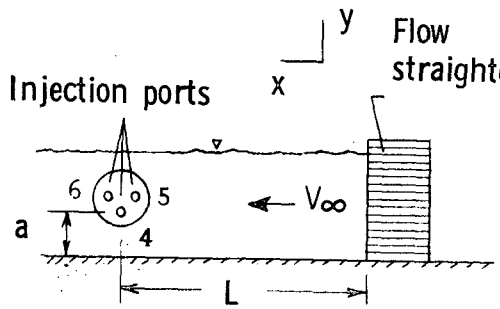

Orifice	a	L
4	1.50	27.00
5	1.95	26.50
6	1.95	27.50

(c) Oblique injection.

Figure 18.- Jet orifice location for different injection conditions; a and L are shown in inches.

The physical dimensions of and flow properties in the water channel were such that fully developed flow (where the mean velocity profiles across the channel are not changing with distance downstream) could not occur. Using nominal flow conditions for the vertical and oblique injection tests (V_∞ = 0.33 ft/sec and T_∞ = 68.0°F), the Reynolds number based on the length along the channel measured from the flow straightener was 6.8×10^4 at the injection station. Similarly, Re_L was 12.8×10^4 for the lateral injection tests. These values of Reynolds number imply a laminar condition for the free-stream flow. Assuming that the flow along the channel walls is equivalent to laminar flow along a flat plate, rough estimates for the laminar boundary-layer thicknesses on the channel walls at the injection point were found from equation (58) to be

$$\frac{\delta}{L} = \frac{5}{\sqrt{Re_L}} \tag{58}$$

0.5 inches for the vertical and oblique injection tests and 0.38 inches for the lateral injection tests. In terms of jet diameters, δ/d_i would be 8 and 6, respectively. These values for δ/d_i are much larger than those usually encountered for air injection tests. For example, the studies of Kamotani and Greber[18] and Ramsey[17] had δ/d_i values of 0.1 and 0.6, respectively. Because the estimated boundary-layer thicknesses are many times larger than the injection port diameters, it is natural to express concern about the influence of the nonuniform free-stream velocity field on the injected jet characteristics. Since no

experimental measurements were made of free-stream velocities, an exercise was performed to assist in a better definition of the free-stream environment into which the jets were injected. This information is presented in Appendix A.

It should be mentioned that the laminar condition of the main flow and of some of the injectant flows(to be shown subsequently) is not compatible with the turbulent nature of actual, full-scale problems. However, since the flow in the mixing region of the jet became turbulent at or near the injection point in all test cases, it is believed that the simulation is reasonable. Also, no attempt was made during the tests to predetermine the relative magnitudes of the buoyancy and momentum forces in the jet flow. The ratio of inertia to buoyancy forces at the injection point (Froude number, Fr_i) is presented in Appendix A for the variety of tests conducted.

RESULTS

The three-dimensional trajectory information for the different injection orientations was obtained for the jet flow having a range of initial velocities and temperatures. The primary output of these experimental tests is photographs which are presented in this section. In all of the photographs the free stream is flowing from right to left. The "effective" velocity ratio (VR) utilized throughout the present paper has been suggested by Margason[13] and Kamotani and Greber[18] as the proper parameter with which to compare different injection situations.

Lateral Injection

Tests were first conducted with the injectant and free-stream temperatures equal in order to provide a basis of comparison for the heated jet results. Photographs of the unheated lateral injection process are presented in Fig. 19 for three injection velocities and show that an increase in jet injection velocity results in further penetration of the jet into the mainstream. The photographs also indicate that for the higher injection velocities the area occupied by the jet fluid begins to grow immediately after injection, and this growth continues as the jet structure bends over under the influence of the free-stream flow and body forces. At some point downstream of the injection station (dependent on the magnitude of the jet velocity compared to the free-stream velocity), the jet flow becomes parallel to the free-stream flow. The turbulent nature of the injection process

Side view

Top view

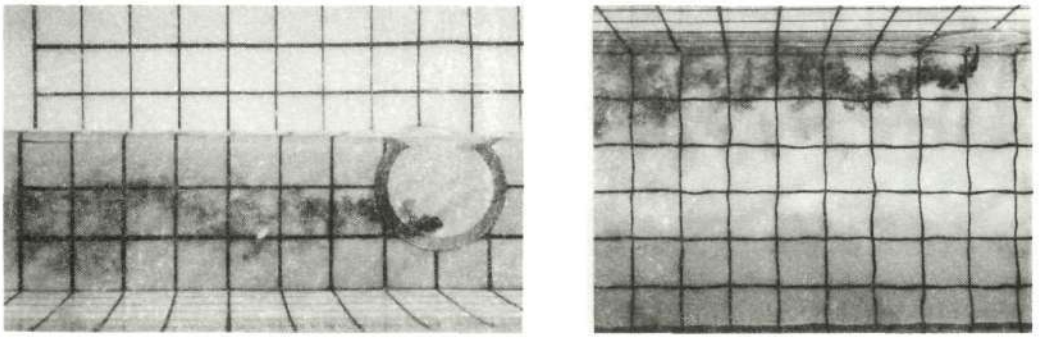

(a) VR = 5.3, Run 9.

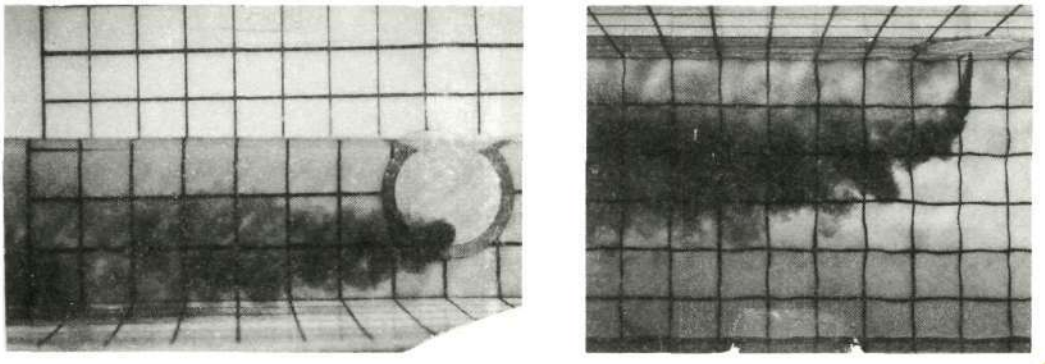

(b) VR = 18.2, Run 8.

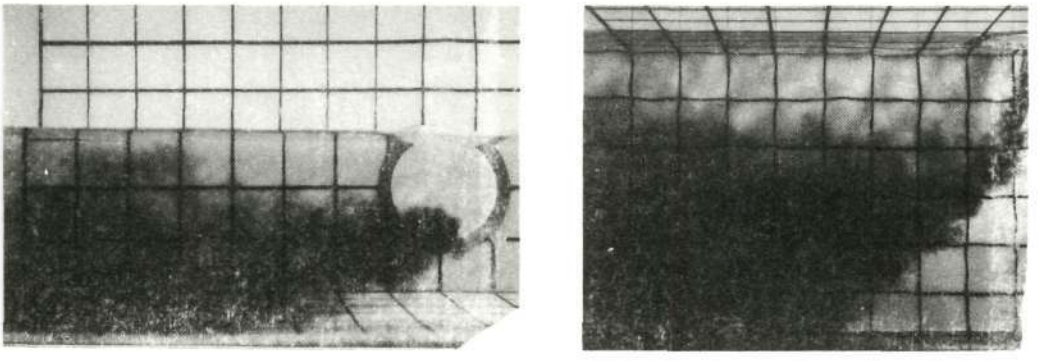

Figure 19.- Photographs of lateral injection process for a range of injection velocities; $\Delta T_i = -2^{\circ}F$.

can be seen by the very irregular boundary of the jet which is indicative of large-scale eddies in the flow. Abramovich[19] and Keffer and Baines[16] provide excellent descriptions of the evolution of a jet injecting into a cross flow.

The basic characteristics of the injection process are the same for the lowest injection velocity (VR = 5.3) except that the jet fluid appears to penetrate a discrete distance into the free-stream flow before beginning to spread. This indicates that the jet flow is laminar at the injection point and undergoes transition to turbulent flow at some point along the trajectory. This laminar flow situation results because the Reynolds number of the jet flow at the injection point (Re_{d_i}) is less than the critical value of Reynolds number ($\simeq$2300) below which the jet flow cannot be turbulent. For example, $Re_{d_i} \approx 1400$ for the VR = 5.3 case. The higher injection velocities in Fig. 19 result in larger values of Re_{d_i} and hence allow the jet flow to begin spreading immediately after injection. The injection studies of Kamotani and Greber[18] and Hoult and Weil[28] are concerned with jets whose flows are initially laminar. In Hoult and Weil's investigation a buoyant plume issuing from a smoke stack was experimentally simulated and several tests were performed to determine when the plume became turbulent.

Centerline trajectories were measured from the photographs in Fig. 19 and are presented in Fig. 20 compared with trajectories estimated by the present theory. As noted, the theory gives a reasonable estimate of the path of the jet as it proceeds downstream

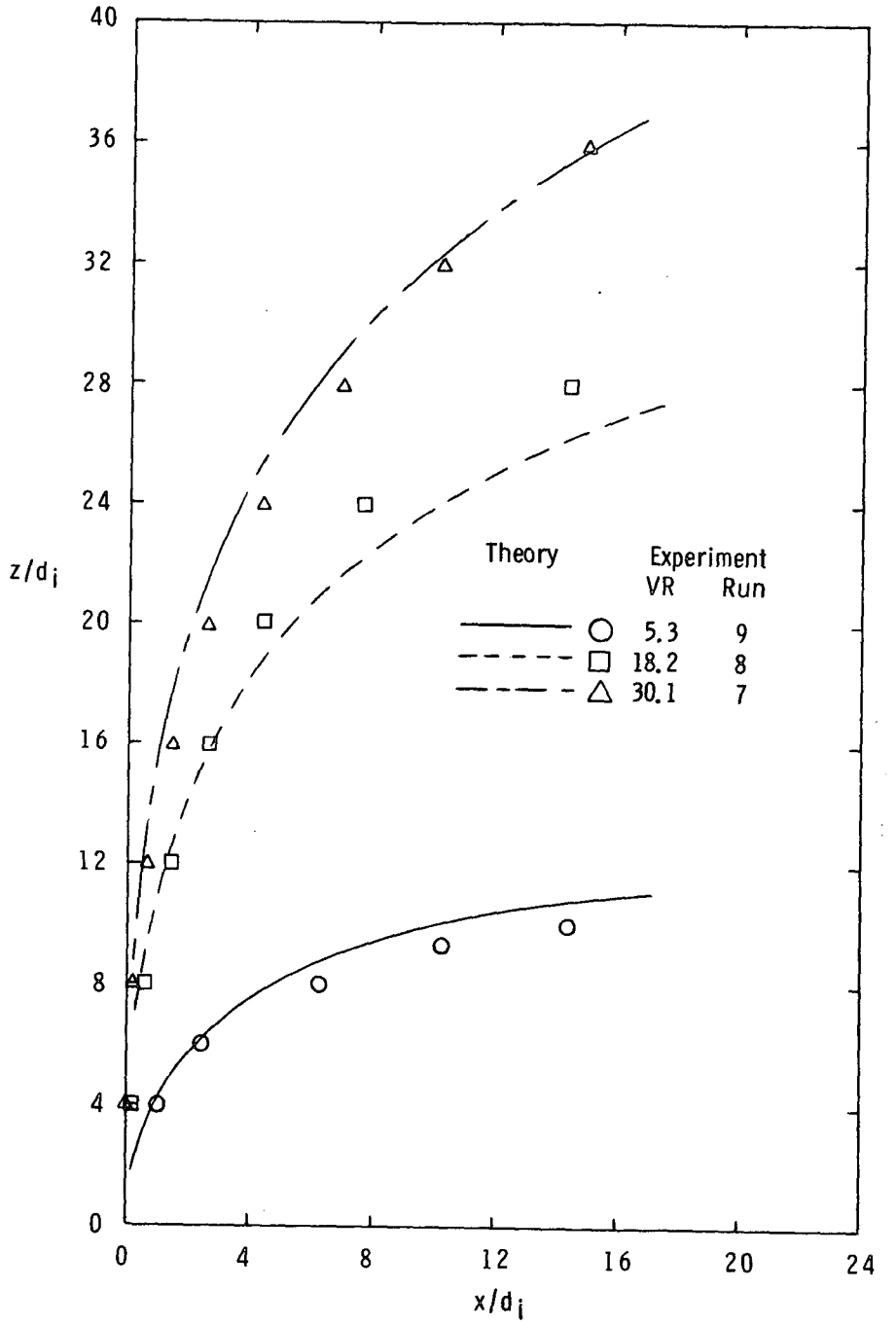

Figure 20.- Experimental and theoretical trajectories for lateral injection process; $\Delta T_i = -2^{\circ}F$.

and predicts the further penetration of the jet into the mainstream that results from increased injection velocity. Unless otherwise noted, the average free-stream velocity (V_∞) listed in Appendix A is used in the theoretical calculations which are compared with the present experimental data.

One of the interesting flow phenomena resulting from a fluid injecting into a cross flow is illustrated in Figure 21 which presents several long exposure photographs for lateral injection with VR = 5.3. The tendency for the jet fluid to gather or collect away from the jet center line (side view) and towards the rear of the jet flow (top view) is indicative of the strength of the rotational velocity field, usually interpreted as a pair of counter-rotating vortices (Fig. 22). These vortices are a product of the complex interactions that take place between the jet and free-stream flows and have been discussed and measured by a number of researchers[16-20]. Keffer and Baines[16], in fact, suggest that far downstream the limiting condition for the jet injection process is a pair of counter-rotating turbulent line vortices moving with the speed of the main stream. During the present study several observations were made with flow visualization devices to confirm the presence of the vortices, however no attempt was made to measure the vortex size or strength.

The effect of adding heat to the injectant is illustrated by the photographs in Figure 23, where the injectant temperature is at least $54^{\circ}F$ greater than the temperature of the free-stream fluid. The gross features of this heated jet injection process are the same as those

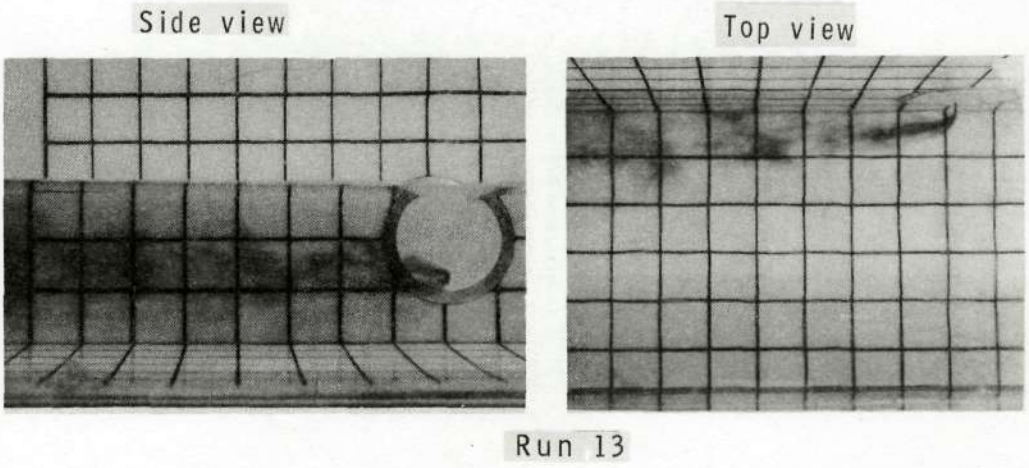

Figure 21.- Long exposure photographs of lateral injection process; VR = 5.3, ΔT_i = -1°F.

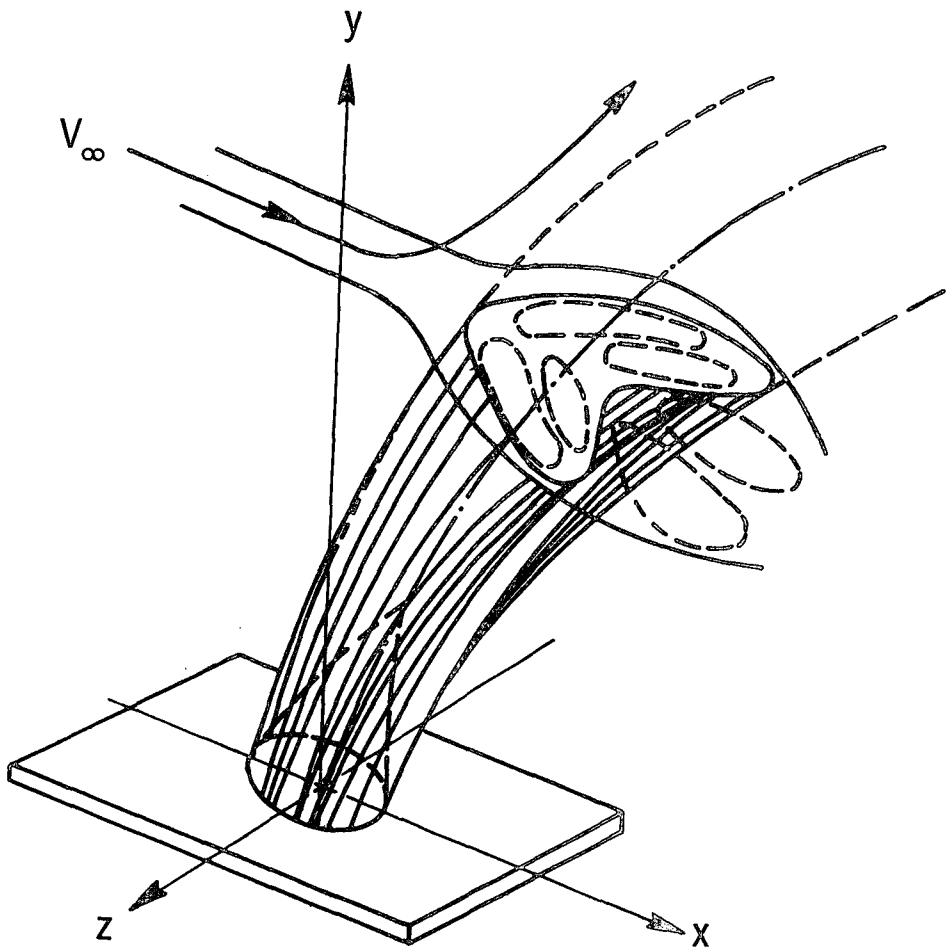

Figure 22.- Diagram of the interaction resulting from jet injection into a cross flow (after Abramovich[19]).

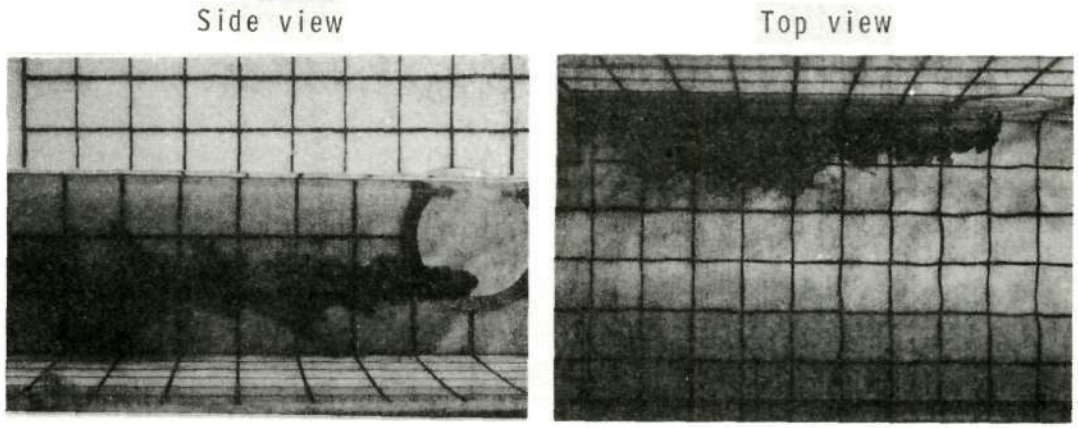

(a) VR =5.2, ΔT_i = 54°F, Run 32.

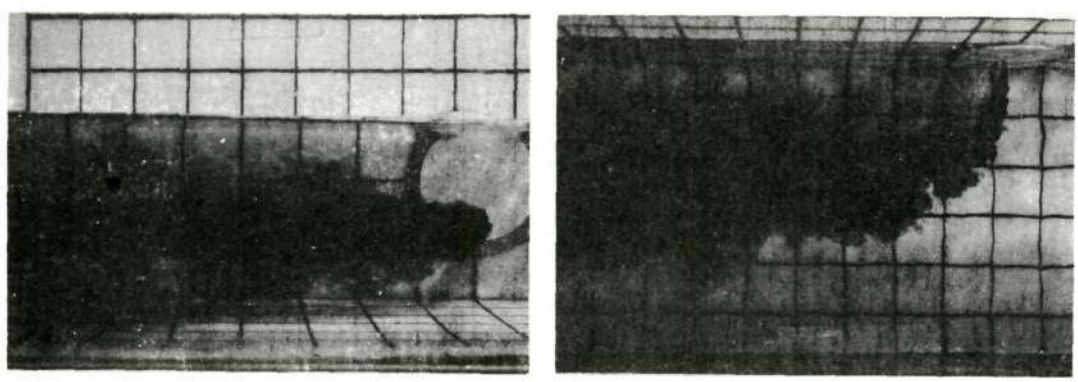

(b) VR = 17.9, ΔT_i = 65°F, Run 31.

Figure 23.- Photographs of heated, lateral injection process for several injection velocities.

discussed for the unheated jet in Figure 19. One noticeable effect is that the fluid for the heated jet appears to spread at a slightly greater rate immediately after injection; this is particularly evident for the lowest injection velocity case (VR = 5.2). This effect on spreading is related to the larger values of Re_{d_i} which result when the jet fluid is heated.

Comparing the photograhs of Figures 19 and 23 we see that there is no discernible effect of the higher injectant temperatures on the jet trajectory. The lack of any significant effect of temperature on the trajectory is believed to be due to the combination of three factors: (1) water density is relatively insensitive to temperature change, (2) momentum forces dominate any buoyancy forces present at these conditions, i.e. the Froude number representing the flow is very large, and (3) the jet fluid experiences a rapid heat loss along the trajectory. To obtain an idea of how rapidly the jet flow losses heat, jet temperature was measured with a thermocouple probe at several locations along the trajectory. Time averages of these temperatures are presented in Figure 11 for VR = 5.2 and are shown plotted in the form of a temperature deficit. The measurements indicate a rapid drop in jet temperature as the jet begins to penetrate into the free-stream flow, and that after this rapid drop the jet temperature slowly approaches the free-stream temperature (T_∞) with increased distance downstream. The photographs in Figure 24 were taken in conjunction with two of the temperature measurements for the VR = 5.2 case.

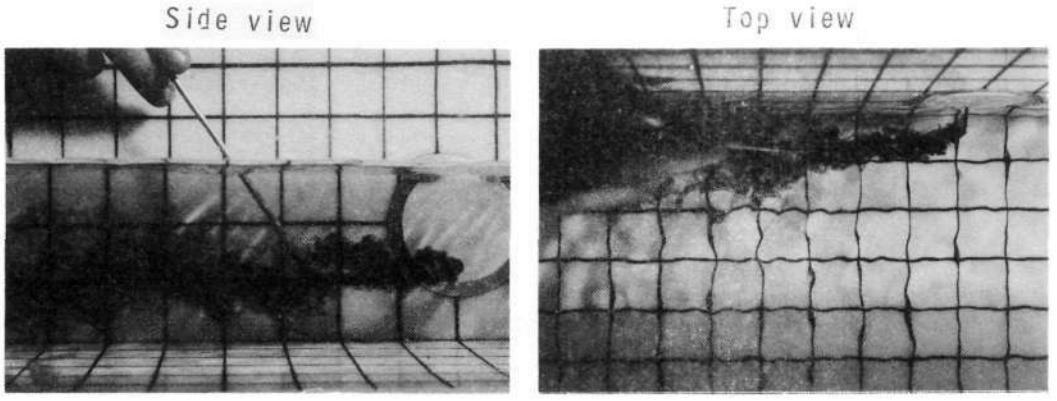

(a) ΔT_j = 63°F, Run 34.

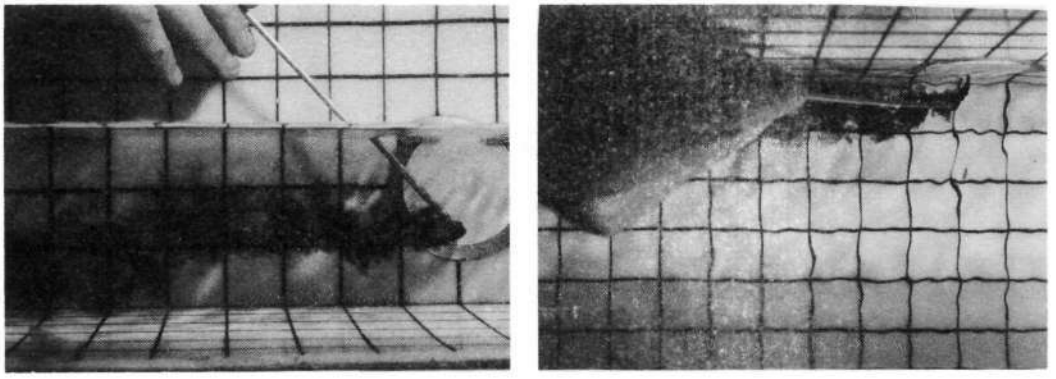

(b) ΔT_j = 62°F, Run 33.

Figure 24.- Photographs of thermocouple probe measurement of heated jet injected laterally with VR = 5.2.

The photographs presented in Figure 25 illustrate the effect of decreasing the vertical distance between the injection port and the free surface of the water channel. The basic characteristics of the injection process for the three injection velocities shown are the same as those discussed in Figure 19 for the lower position of the injection port. The one obvious effect of injecting closer to the free surface is observed for the highest injection velocity (VR = 28.5). The wave pattern that is generated on the free surface (top view) is an indication of how severely the free-stream flow is disturbed, or blocked, by the jet flow.

Vertical Injection

The effect of increasing the velocity of a jet injecting vertically into the main stream is shown in the photographs of Figure 26 where the injectant and free-stream temperatures are essentially the same. The basic characteristics of the injection process are the same as those discussed previously for lateral injection. The jet flow for VR = 8.8 shows evidence of laminar flow immediately after injection, similar to the lateral jet flow (VR = 5.3) noted in Figure 19. In fact, the initial laminar region appears to be more pronounced for the vertical injection case than for the lateral injection case. In comparing these two runs, it should be noted that the free-stream conditions are different. The vertical injection situation has a lower free-stream velocity than the lateral injection case, and hence has a larger boundary layer thickness at the injection point. This larger value of

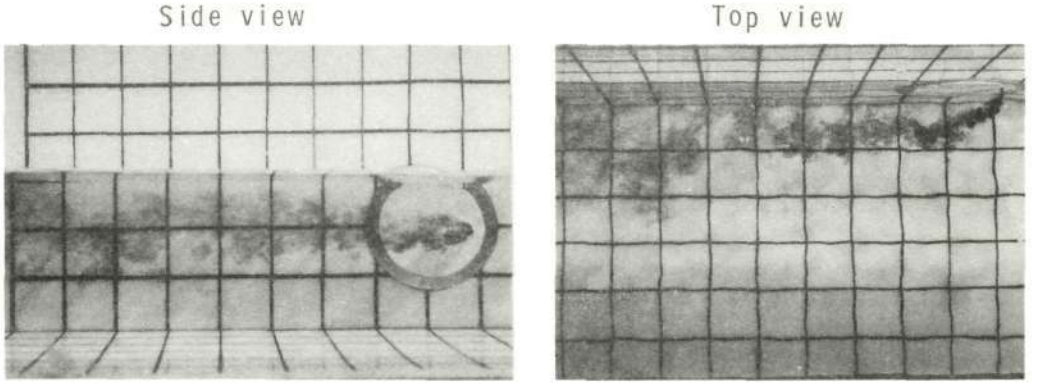

(a) VR = 5.0, Run 16.

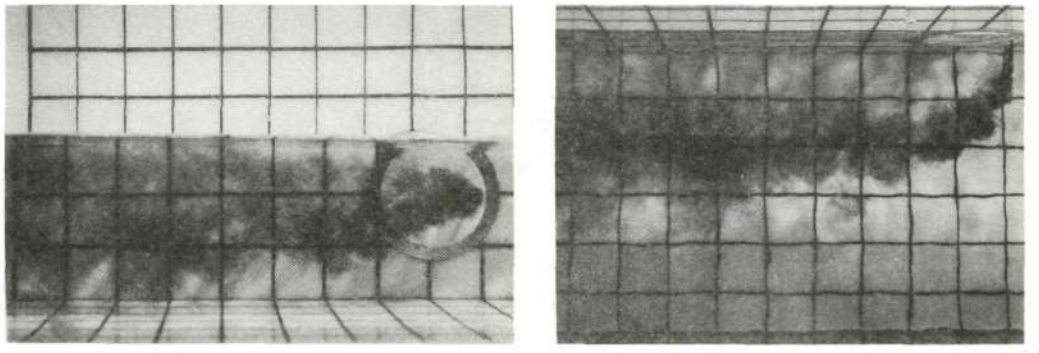

(b) VR = 17.2, Run 15.

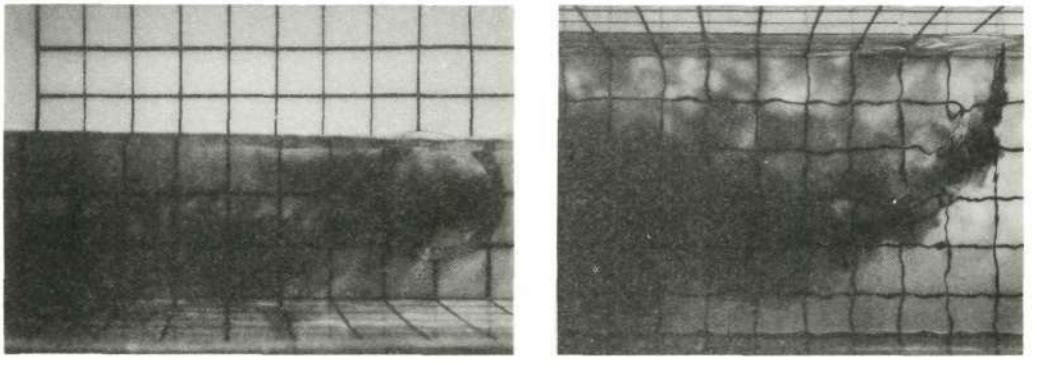

(c) VR = 28.5, Run 14.

Figure 25.- Photographs of lateral injection near the free surface for a range of injection velocities; $\Delta T_i = 0^{\circ}F$.

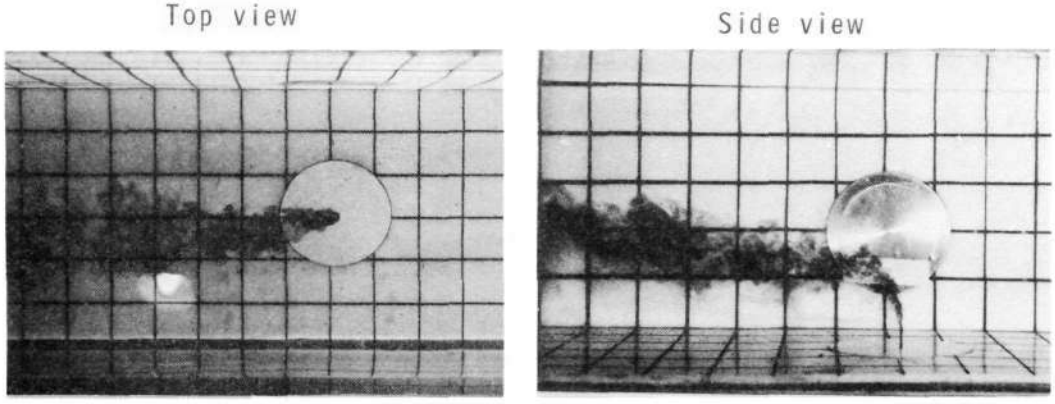

(a) VR = 8.8, Run 38

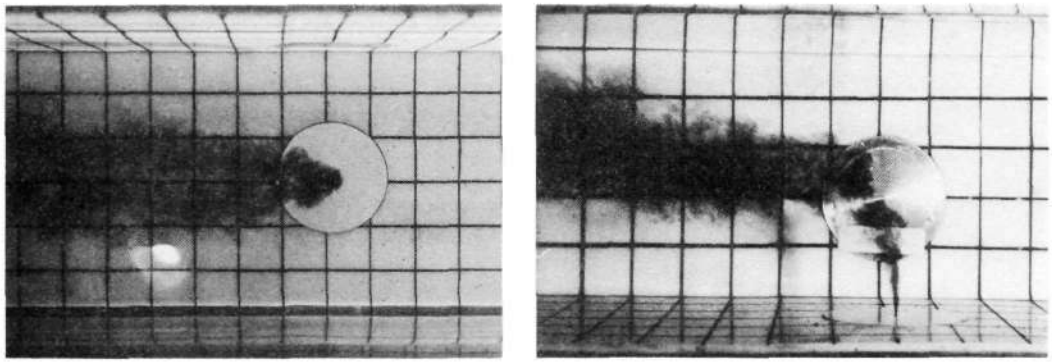

(b) VR = 17.2, Run 39.

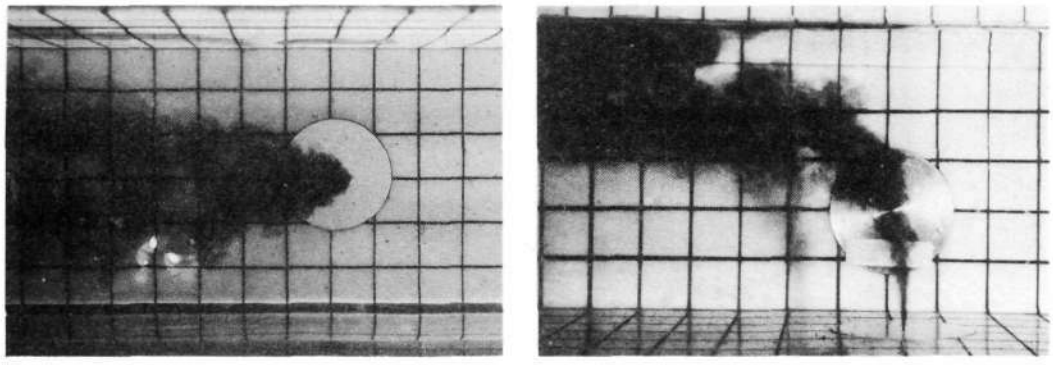

(c) VR = 28.9, Run 40.

Figure 26.- Photographs of vertical injection process for a range of injection velocities; $\Delta T_i = -3^{\circ}F$.

δ coupled with a lower value of Re_{d_i} can account for the more pronounced laminar flow condition for the vertical injection than for the lateral injection.

The center-line trajectories for the three injection velocities presented in Figure 26 are shown in Figure 27 compared to the theoretical trajectories (solid line) which represent fully turbulent jet flows. As noted, the experimental mixed-flow jets penetrate much further into the free stream than would be theoretically expected for fully turbulent jets. In order to estimate the trajectories for this mixed-flow situation, the present theory was adjusted to account for the initial laminar portion of the jet flow. This was accomplished by assuming that the jet begins its turbulent growth at a point (y_o/d_i) specified in the photographs in Fig. 26. Since the location and extent of the transition region in the flow are functions of injection conditions (e.g. Re_{d_i}), as well as free-stream conditions (e.g. VR), it is expected that the values of y_o/d_i will change accordingly. The appropriate values of y_o/d_i used to modify the theory are shown in Fig. 27 and the resulting calculations represented by the dashed lines.

The effects of increasing injectant temperature on the vertical injection process are presented in the photographs in Figure 28. The slight increase in spreading of the jet fluid with increase in temperature is seen in the jet flow immediately after injection. This is particularly the case for the jet with the lowest injection velocity, this trend being similar to the temperature effects discussed for

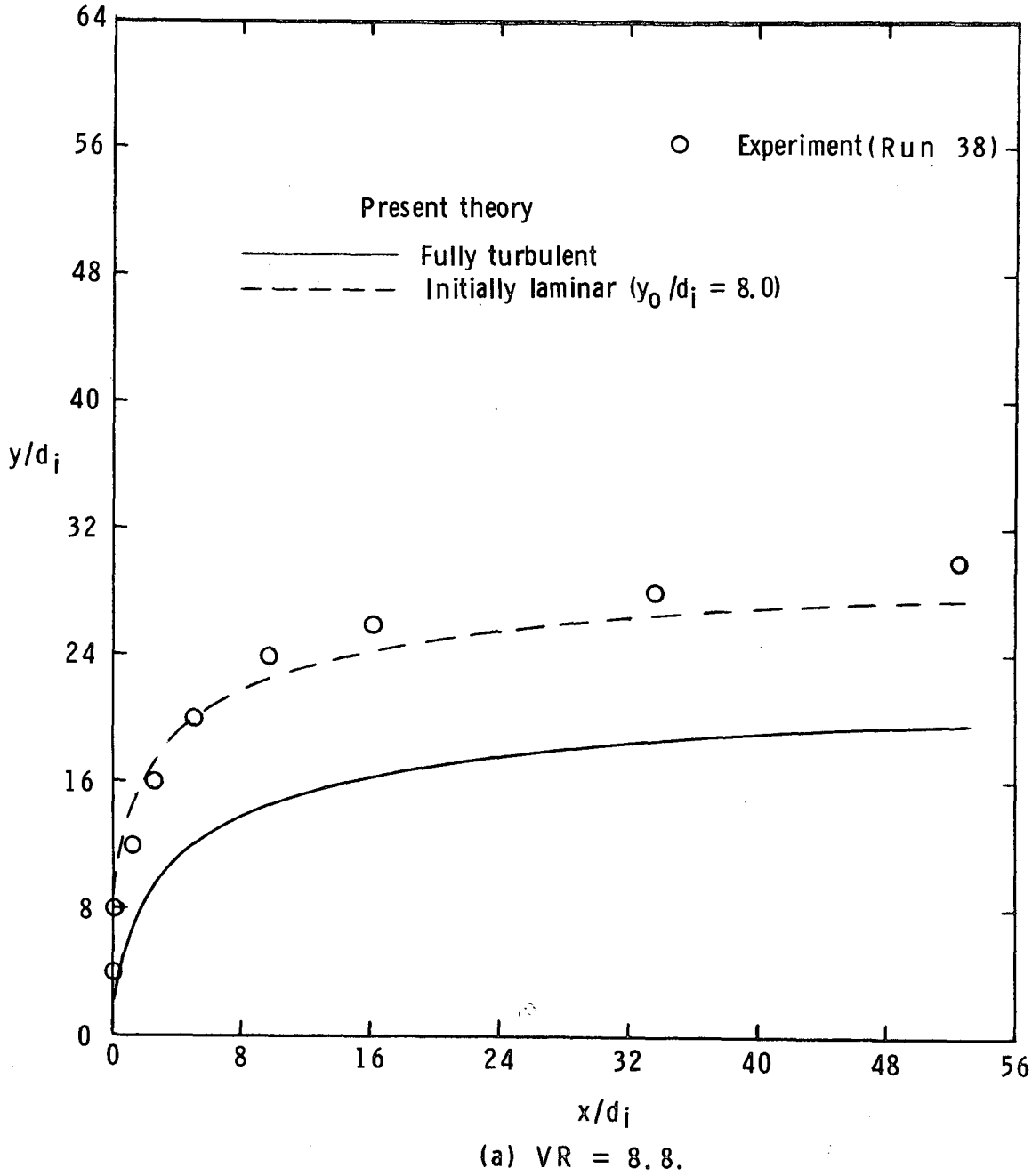

Figure 27.- Experimental and theoretical trajectories for the vertical injection process, $\Delta T_i = -3^{\circ}F$; experimental trajectories are for jets with initially laminar flow.

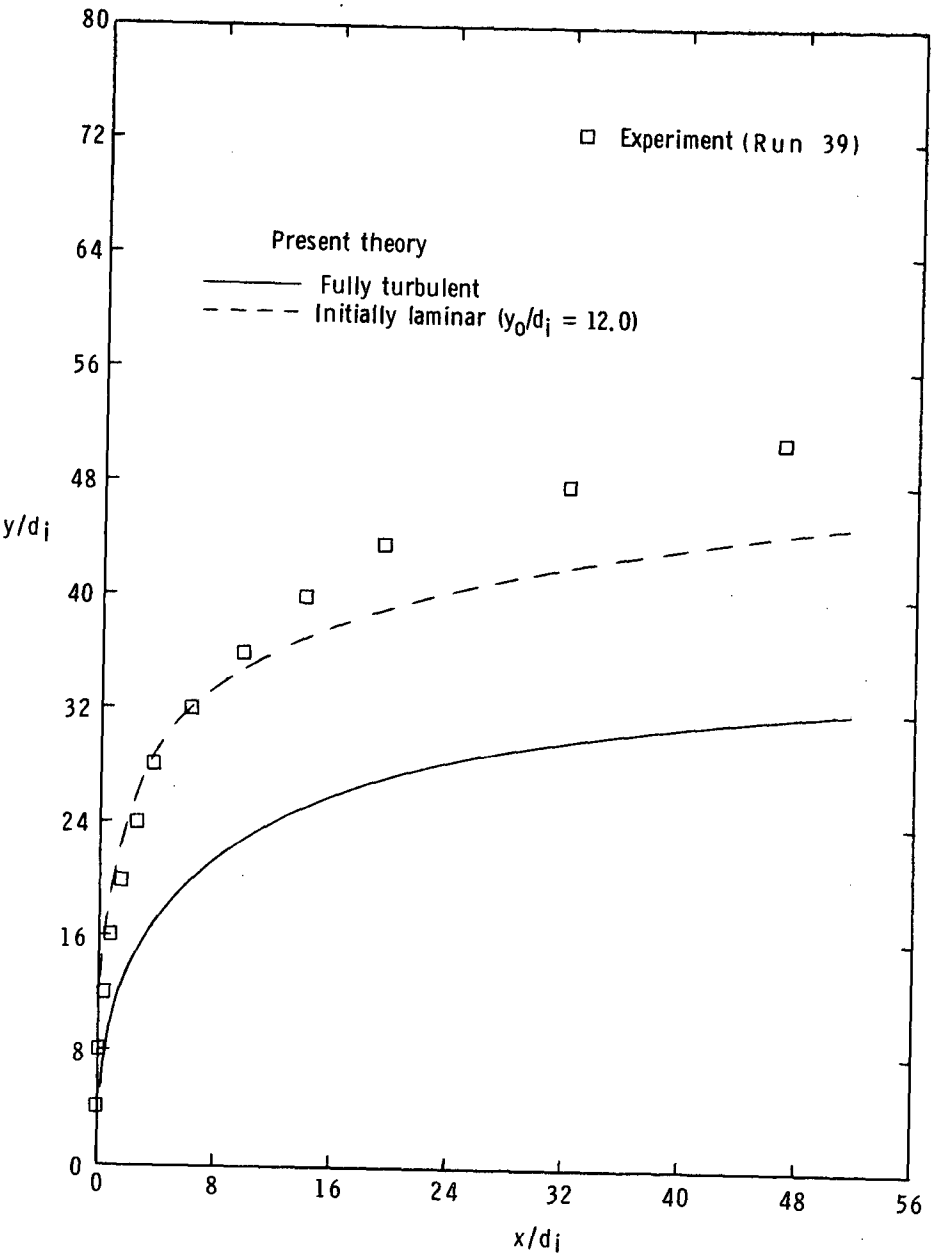

(b) VR = 17.2.

Figure 27.- Continued.

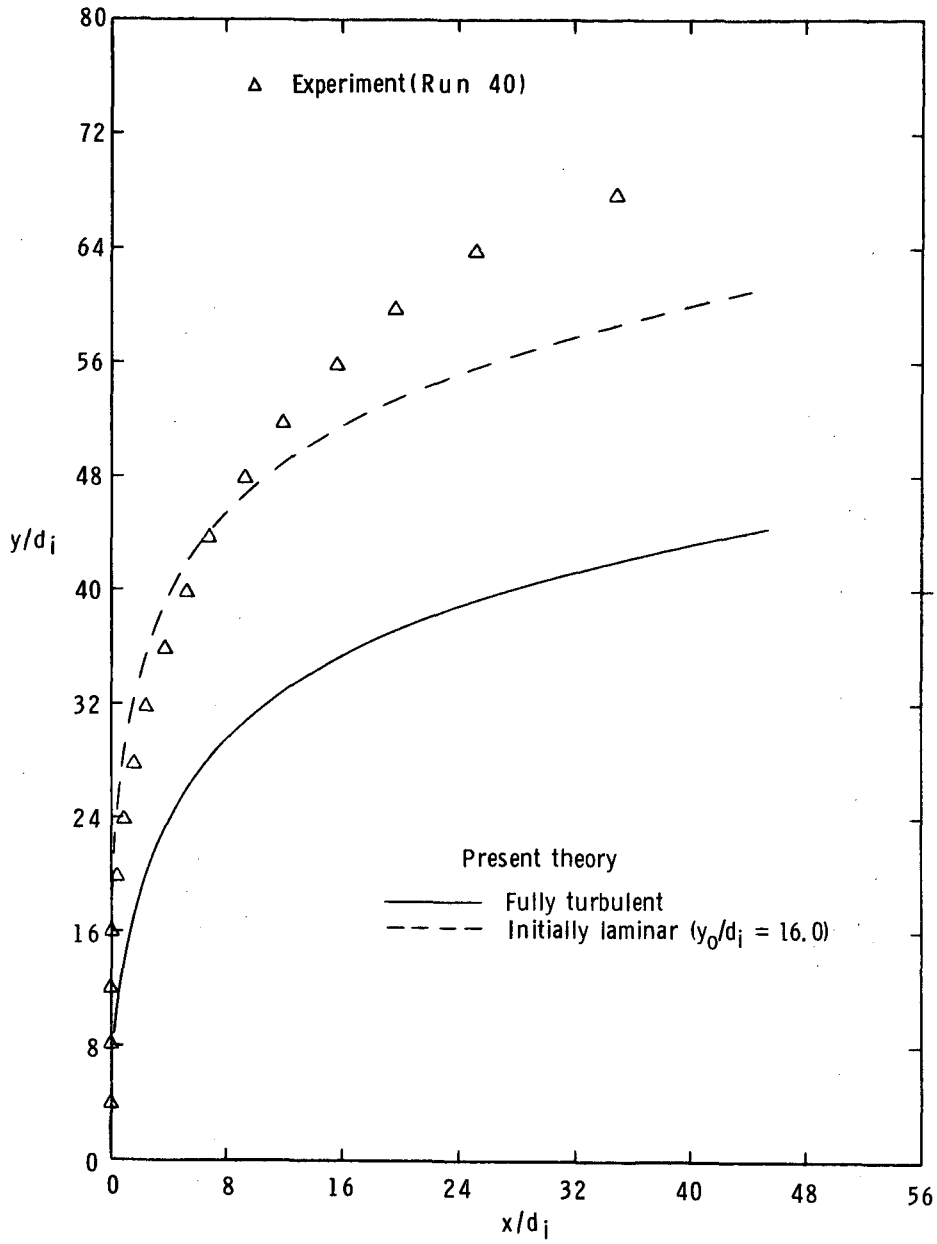

(c) VR = 28.9.

Figure 27.- Concluded.

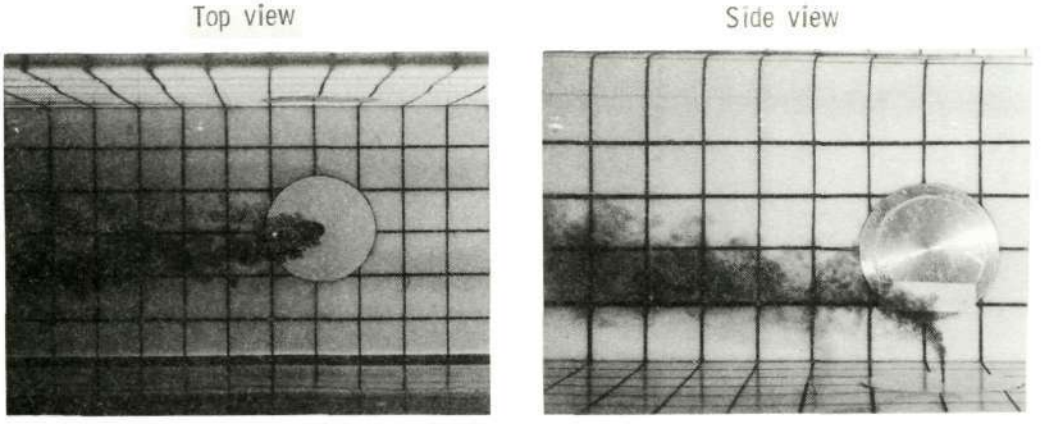

(a) VR = 8.8, ΔT_j = 26°F, Run 45.

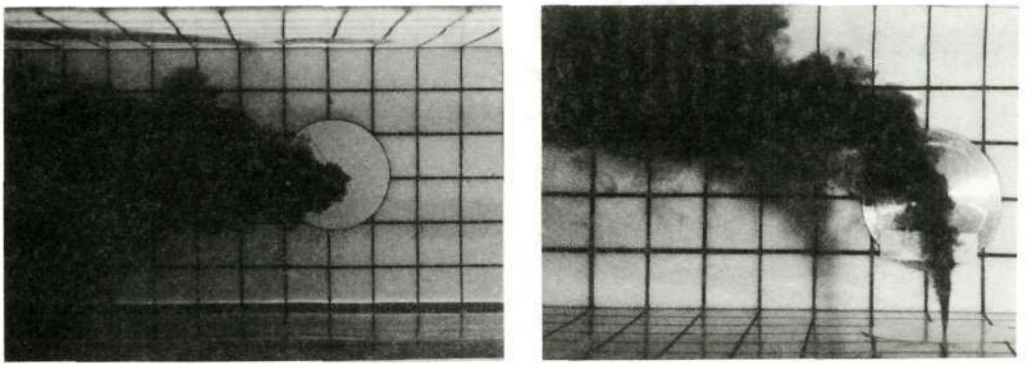

(b) VR = 29.0, ΔT_j = 25°F, Run 46.

Figure 28.- Effect of increasing injection temperature on vertical injection process for a range of injection velocities.

Top view

Side view

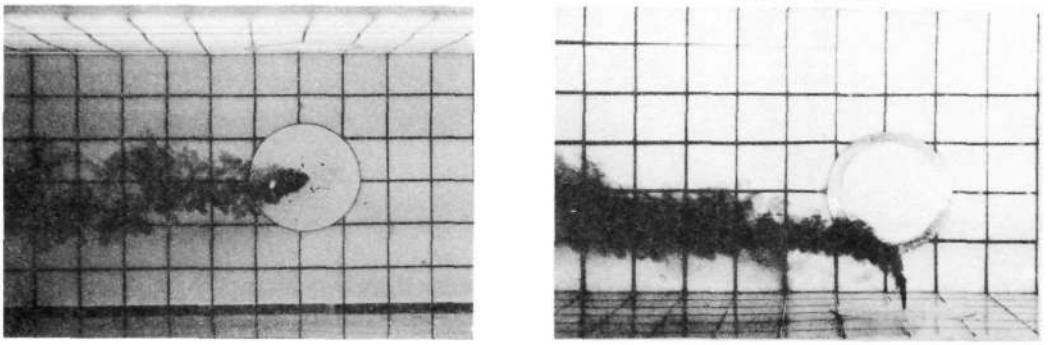

(c) VR = 9.6, ΔT_i =46°F, Run 65.

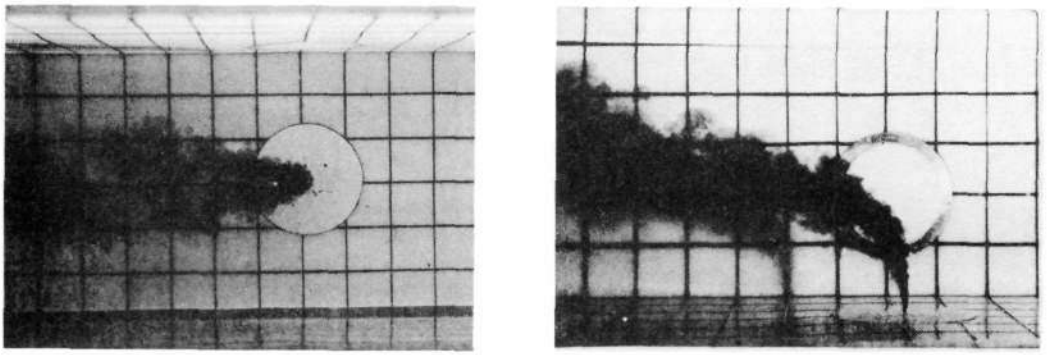

(d) VR = 18.7, ΔT_i = 44°F, Run 64.

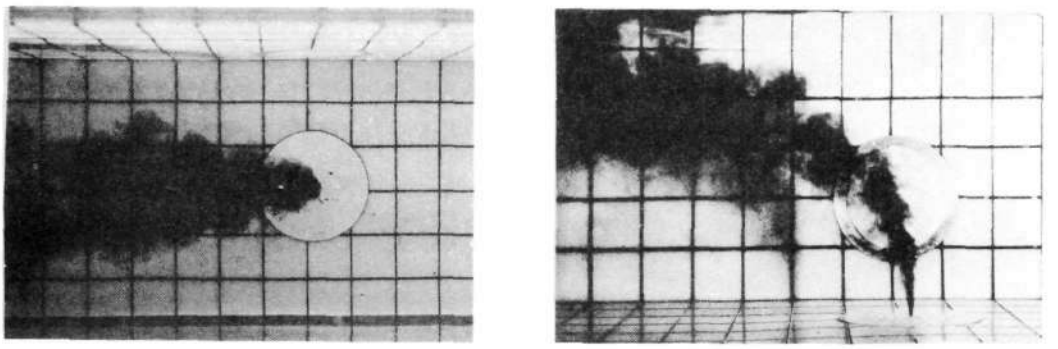

(e) VR = 31.4, ΔT_i = 44°F, Run 63.

Figure 28.– Concluded.

lateral injection. The photographs for vertical injection indicate that increasing injectant temperature tends to decrease the amount of penetration for the jet, even though heating the injectant causes slightly higher values of VR. This result is better illustrated in Figure 29 where the center-line trajectories are shown for the various injection velocities and temperatures investigated. The effect of injectant temperature on trajectory is mainly the result of the temperature effect on the transition of the jet flow, where an increase in temprature increases Re_{d_i} and hence decreases the extent of the laminar portion of the flow. Theoretical calculations are shown for comparison with the experimental trajectories obtained with the highest injectant temperature, where the fully turbulent flow condition is represented by a solid line, and the initially laminar flow condition by a dashed line. The procedure for adjusting the theory to account for the initial laminar flow is the same as that reported for the results in Fig. 27, although the values of y_o/d_i are smaller.

Oblique Injection

The primary characteristics obtained by injecting obliquely ($\alpha_i = 90^\circ$, $\beta_i = 50^\circ$) into the main stream are seen in Figure 30 to be similar to those discussed for the lateral and vertical injection processes. The condition of laminar jet flow near the injection point that was observed for the lowest injection velocity cases for the previous injection processes is not as apparent here even though the value of Re_{d_i} is comparable. This may be due to the increased

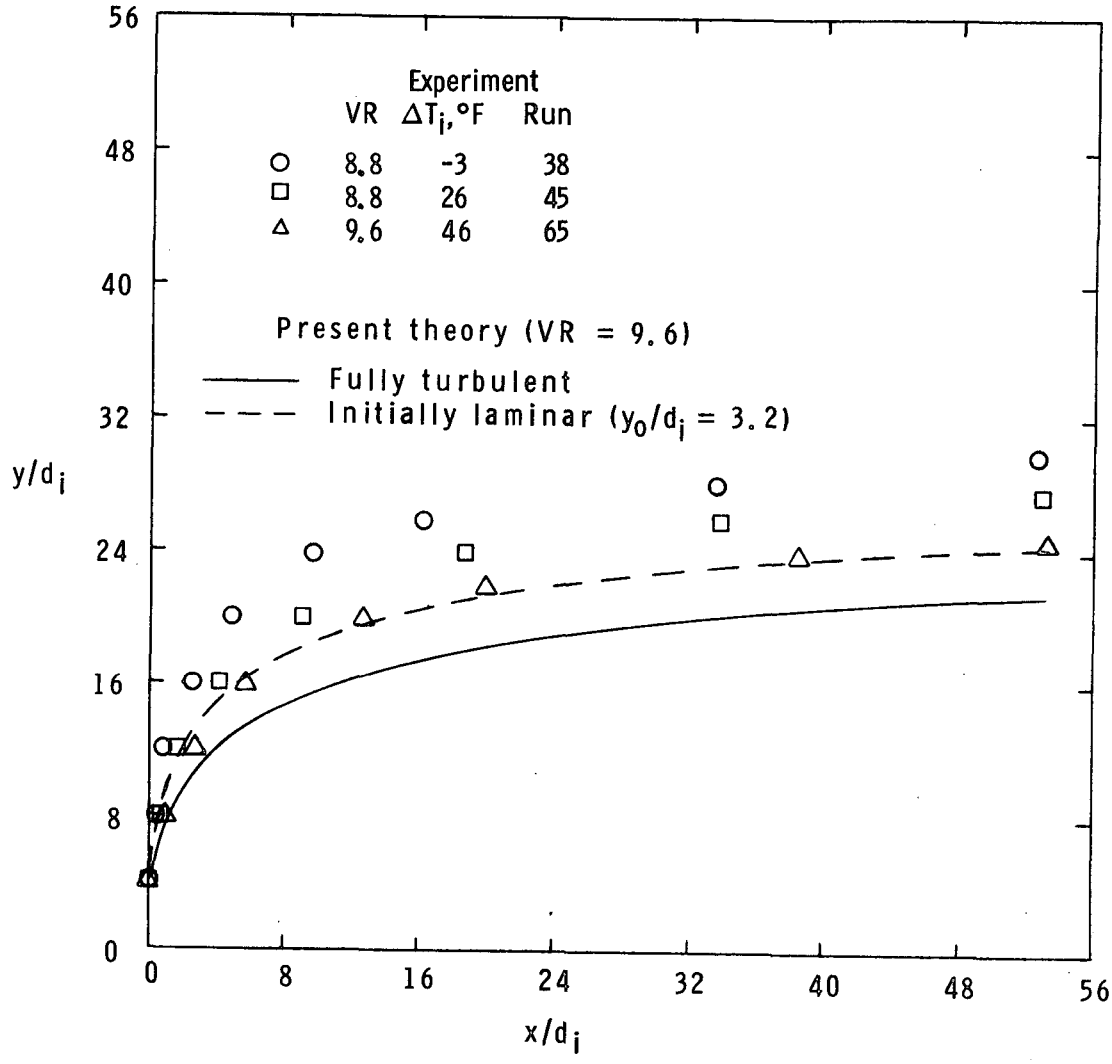

Figure 29.- Effect of injectant temperature on trajectory for vertical injection process; experimental trajectories are for jets with initially laminar flow.

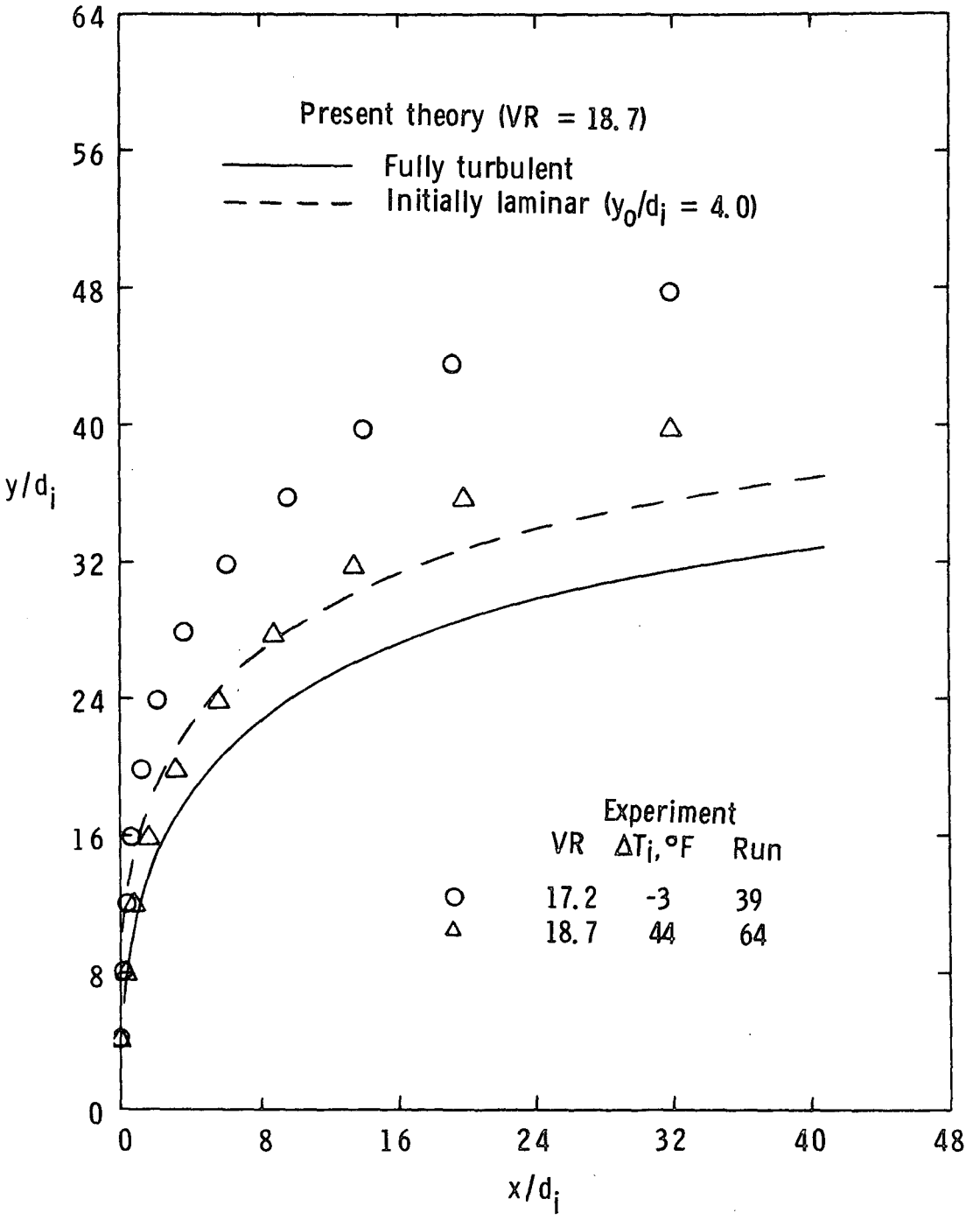

Figure 29.- Continued.

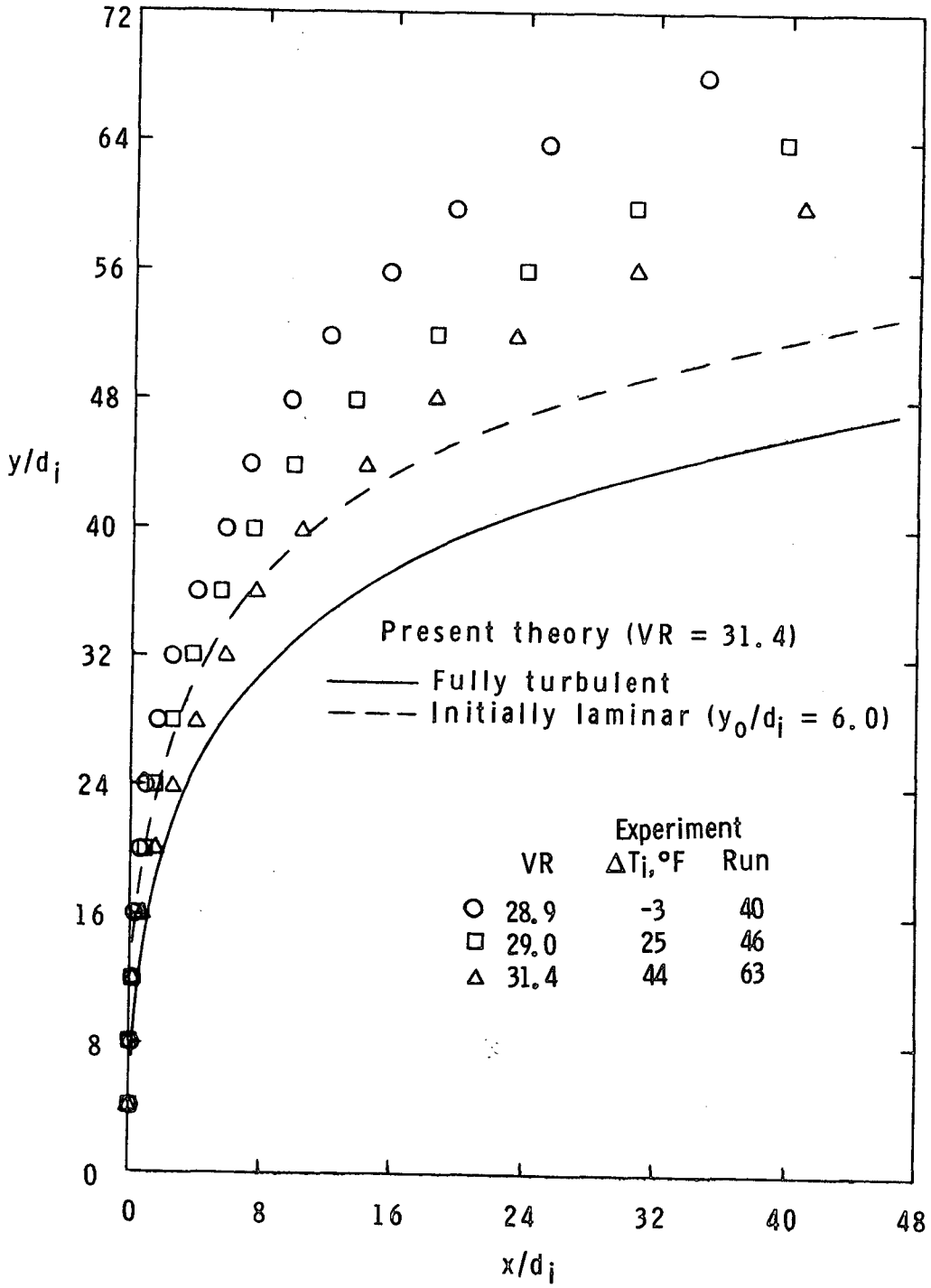

Figure 29.- Concluded.

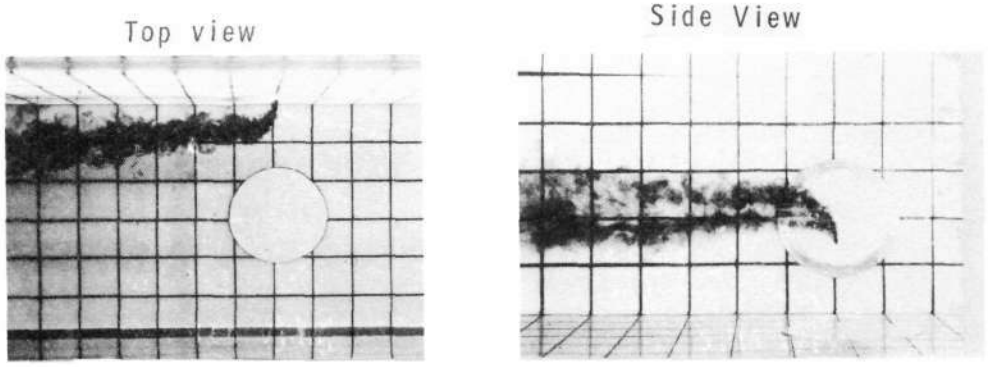

(a) VR = 8.1, ΔT_j = 5°F, Run 55.

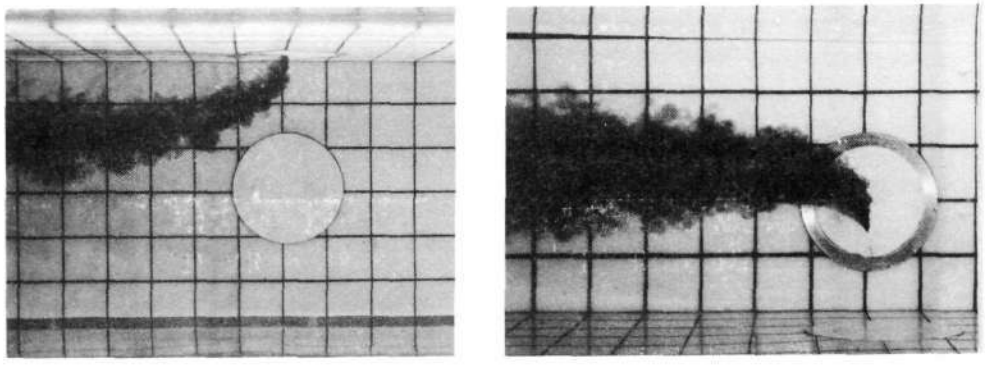

(b) VR = 15.8, ΔT_j = 4°F, Run 54.

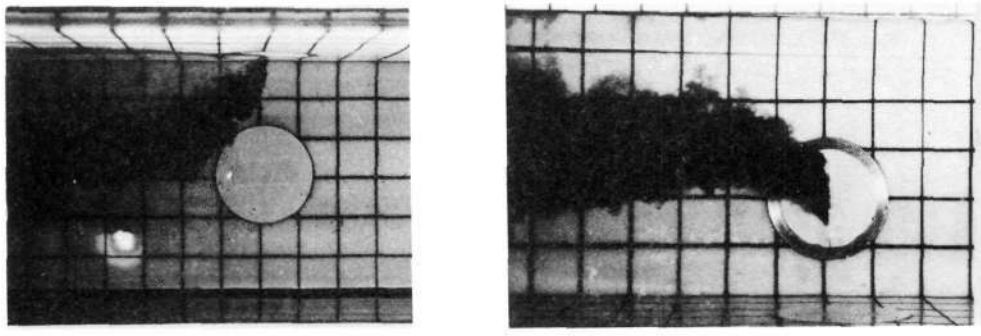

(c) VR = 26.6, ΔT_j = 9°F, Run 53.

Figure 30.- Photographs of oblique injection process for a range of injection velocities; $\alpha_i = 90°$, $\beta_i = 50°$.

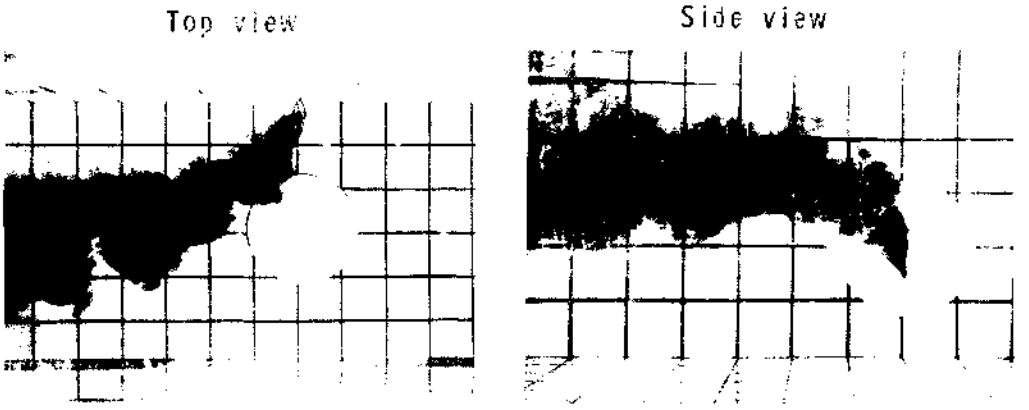

(d) VR = 37.8, ΔT_i = 5°F, Run 56.

Figure 30.- Concluded.

vorticity interaction that occurs between the jet flow and the wall boundary layer. For this type of oblique injection the effects of increasing injection velocity on trajectory are observed in two planes instead of just one plane as is the case for lateral and vertical injections. Centerline trajectories in the X-Y and X-Z planes are measured from the photographs (Figure 30) and presented in Figure 31. From these data it is evident that the jet flow penetrates farther into the free stream in the lateral (Z) direction than in the vertical (Y) direction. This trend is more obvious at the higher injection velocities and results because the lateral momentum of the jet is larger than the vertical momentum at the injection point where $\beta_i = 50^\circ$. The projections of the trajectory onto the two planes would be expected to be identical if the oblique injection process had $\beta_i = 45^\circ$ and was void of any wall or boundary-layer effects. Trajectories estimated by the present theory are shown in Fig. 31 for comparison with the experimental data. The theory does predict the experimental trends discussed above, although it estimates slightly less vertical penetration and more lateral penetration for a given value of VR than is indicated by the data.

The effect of adding heat to the injectant can be seen in the photographs in Figure 32, where increasing injection temperature causes a slightly greater rate of spreading by the jet fluid near the injection point, particularly for the lower injection velocities. Also, the higher temperature jets generally penetrate farther into the free-stream flow than those in Figure 30. The effect of injection

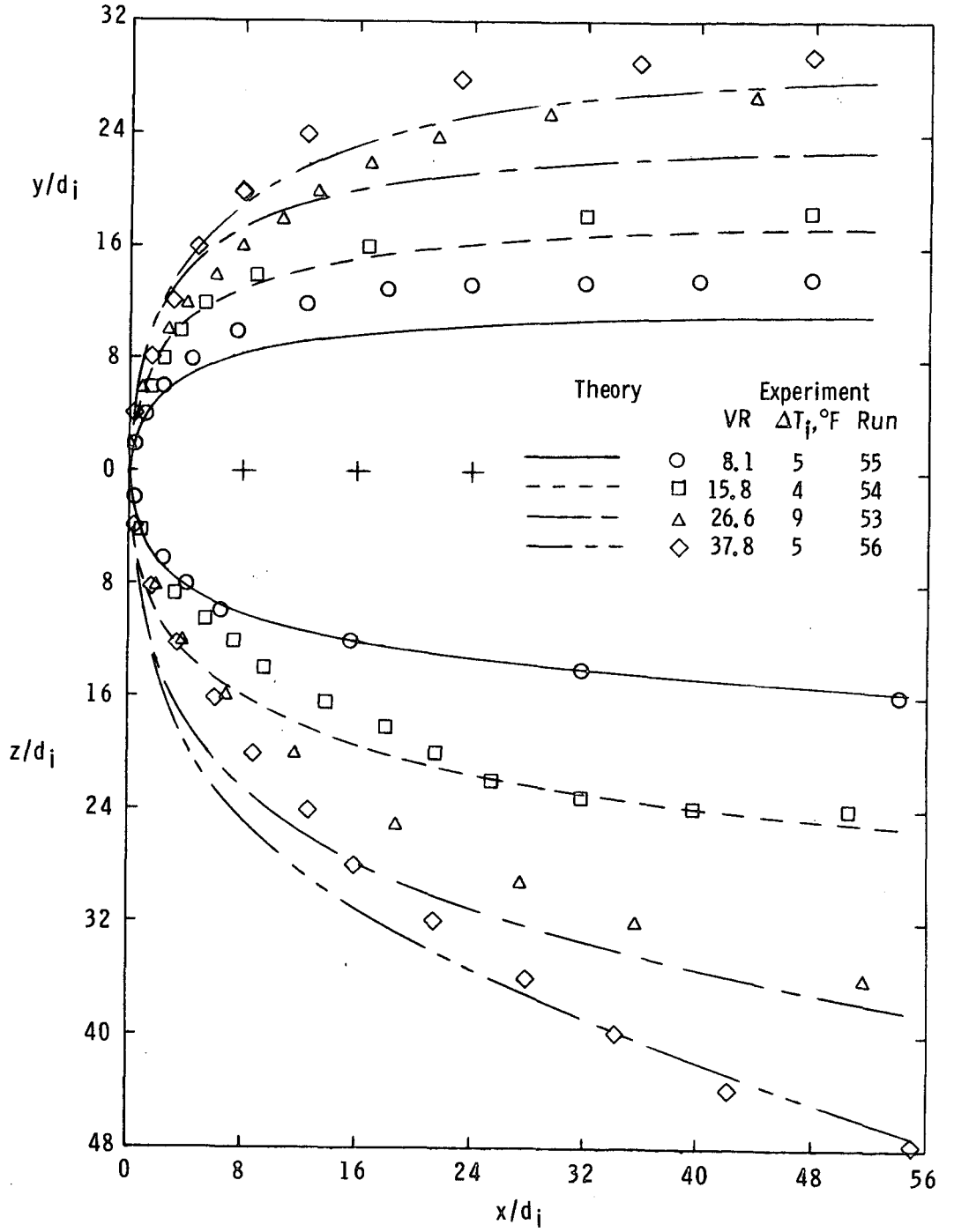

Figure 31.- Experimental and theoretical trajectories for oblique injection process; $\alpha_i = 90^\circ$, $\beta_i = 50^\circ$.

Top view

Side view

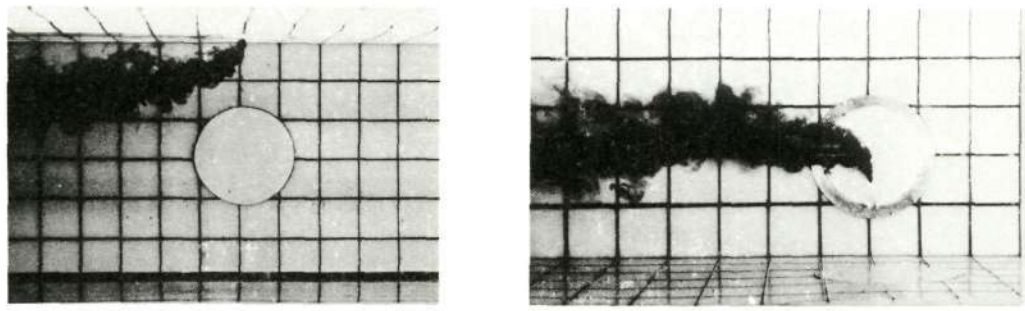

(a) VR = 8.1, ΔT_i = 46°F, Run 60.

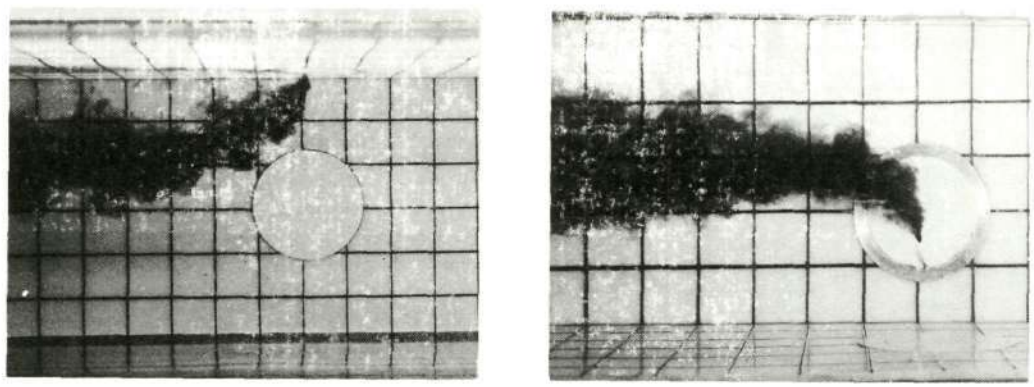

(b) VR = 15.9, ΔT_i = 44°F, Run 59.

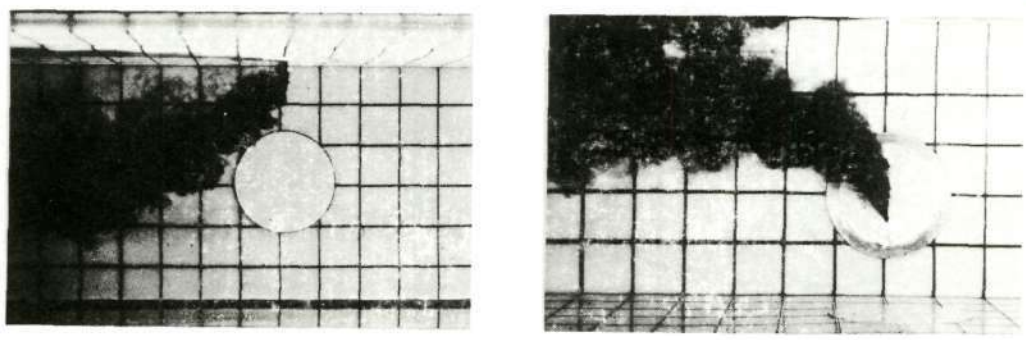

(c) VR = 26.7, ΔT_i = 48°F, Run 58.

Figure 32.- Photographs of heated, oblique injection process for a range of injection velocities; α_i = 90°, β_i = 50°.

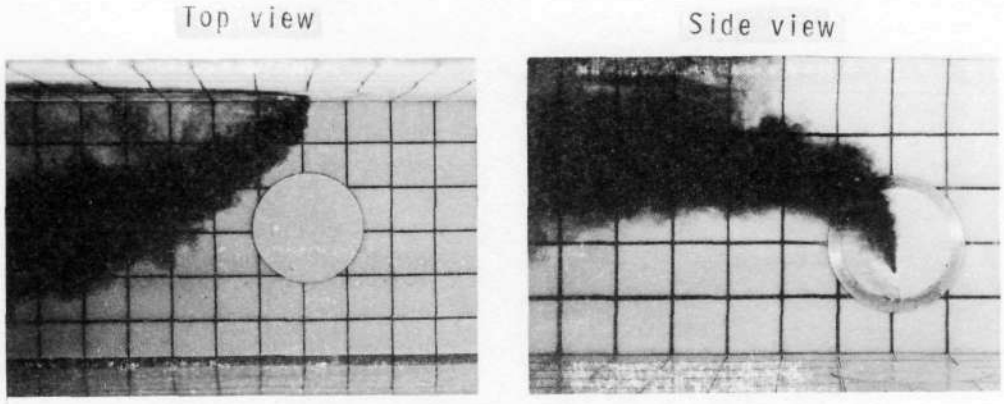

(d) VR = 38.0, ΔT_j = 63°F, Run 61

Figure 32.- Concluded.

temperature on centerline trajectory for oblique injection is shown in Figure 33 for the different injection velocities investigated.

The fact that the oblique injection condition demonstrates an increase in jet flow penetration with increase in injectant temperature, while the vertical and lateral injection conditions do not demonstrate this effect, draws attention to a subtle difference between these injection cases which is related to the orientation of the counter-rotating vortices in the respective jet flows. For the lateral and vertical injection situations, the jet is injected perpendicularly through the boundary layer on the adjacent wall. The vortices formed during these injection processes are located symmetrically on either side of the jet center-line, such that a line drawn between the vortex centers would be parallel to the vorticity vector associated with the boundary-layer velocity field. This description is not completely accurate for oblique injection through the boundary layer. From observations of the oblique injection experiments, it appeared as if the vortex pair was "twisted" immediately after injection so that the pair was oriented in a manner similar to the vortices generated by a lateral injection, that is, where the line between the vortex centers is vertical. Although detailed measurements are necessary to validate these comments, it is believed that the observed effects of injection temperature on the jet path for the three injection conditions are due to differences in vortex formation in the respective jet flows.

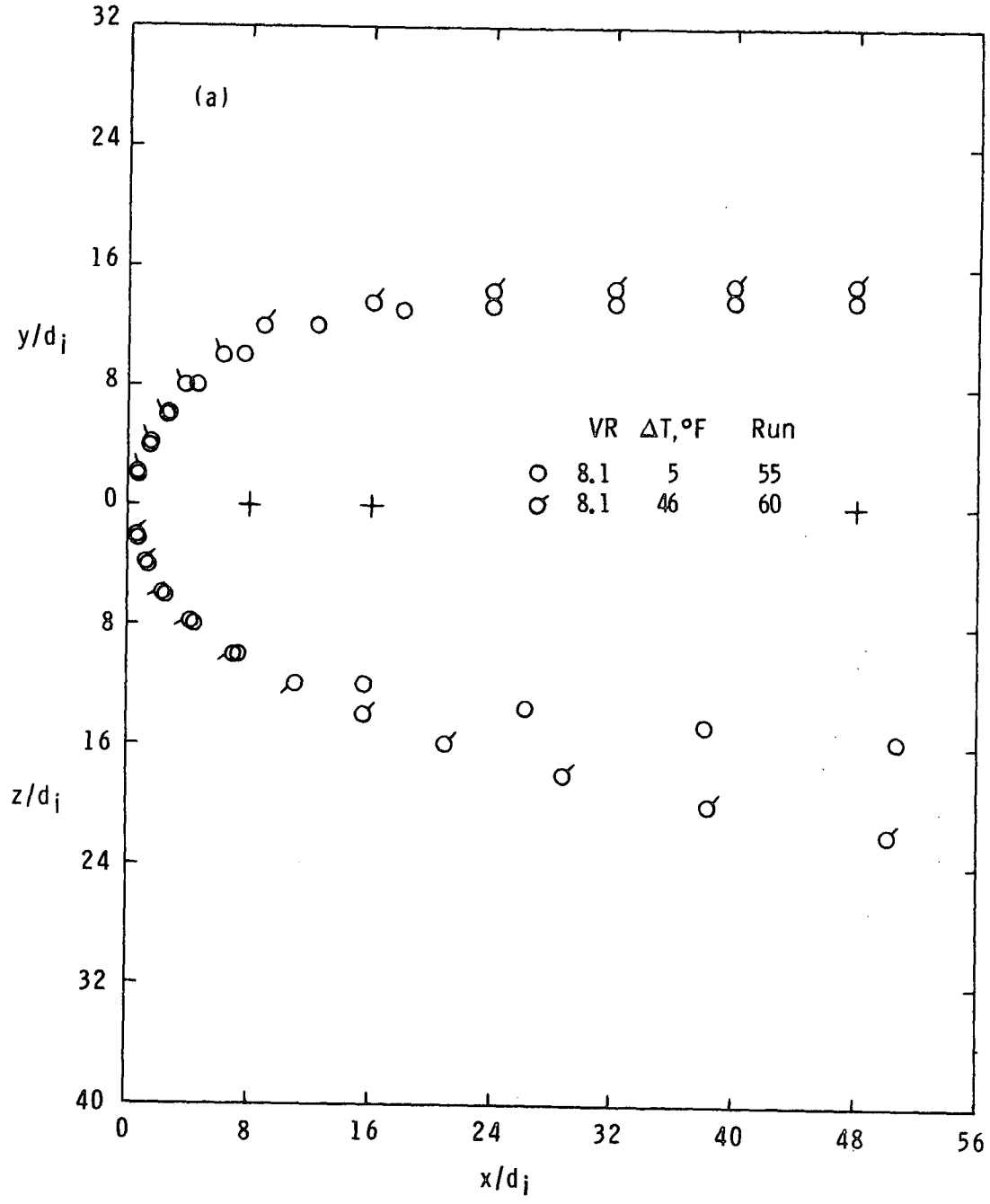

Figure 33.- Effect of injectant temperature on trajectory resulting from oblique injection; $\alpha_i = 90°$, $\beta_i = 50°$.

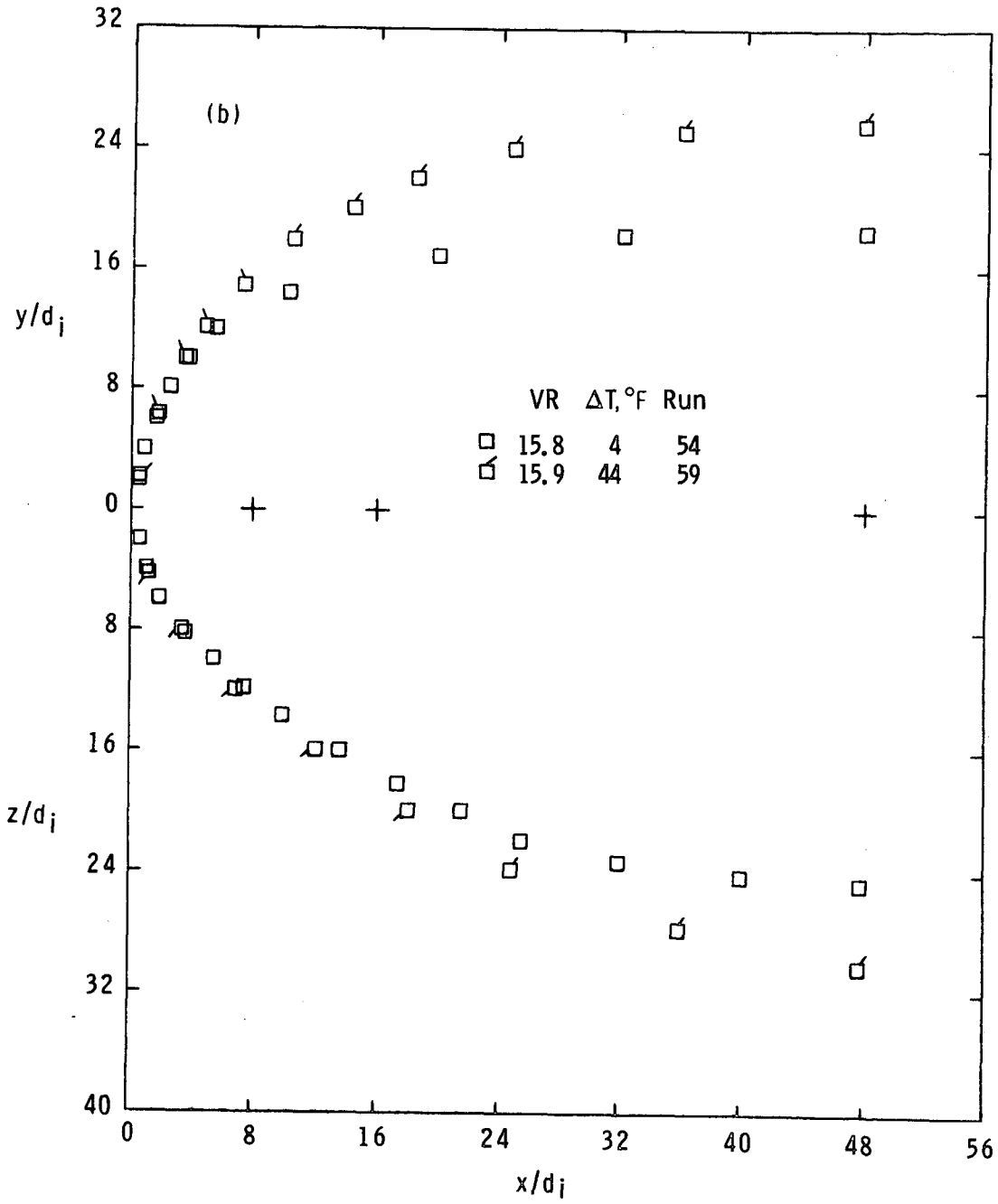

Figure 33.- Continued.

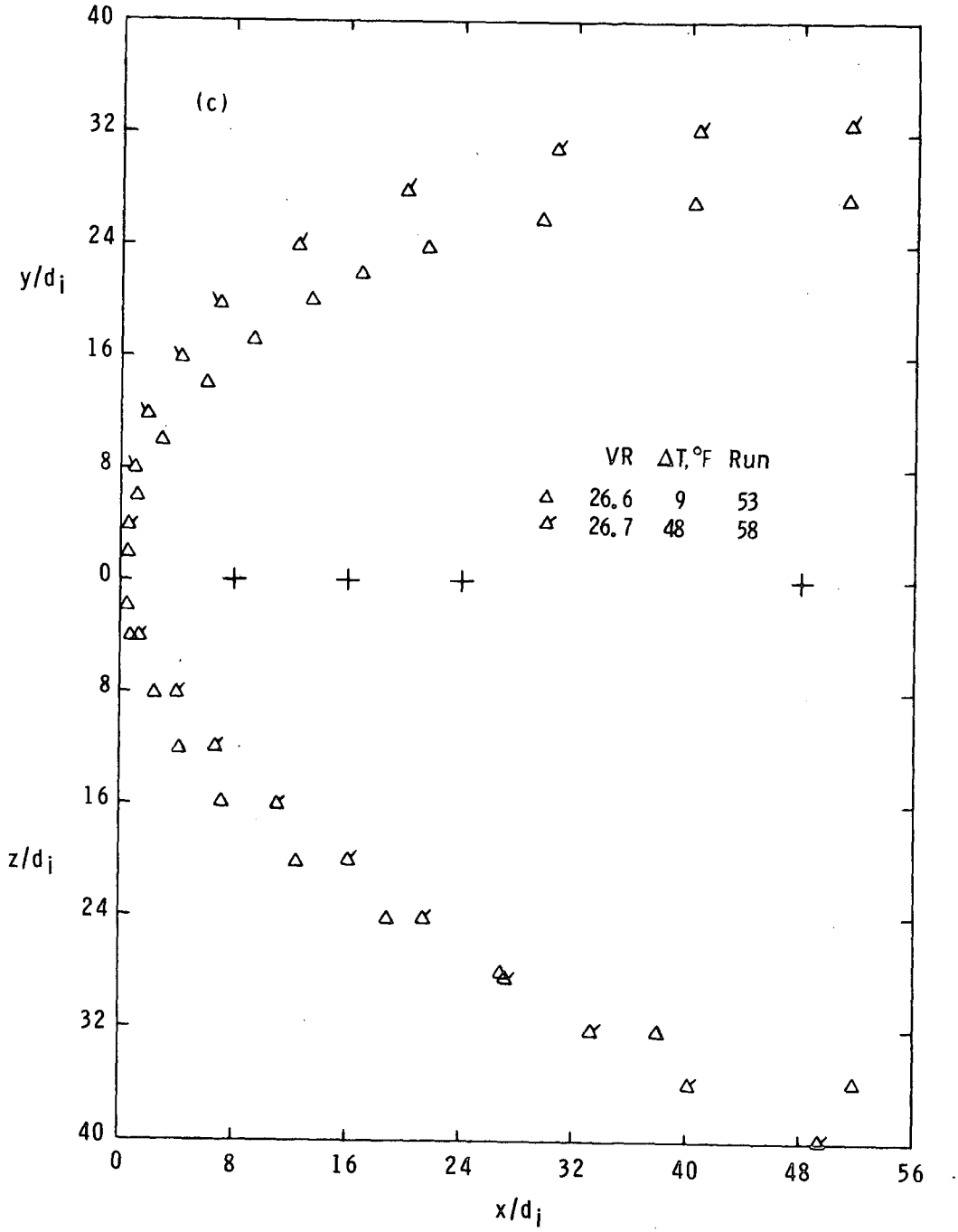

Figure 33.- Continued.

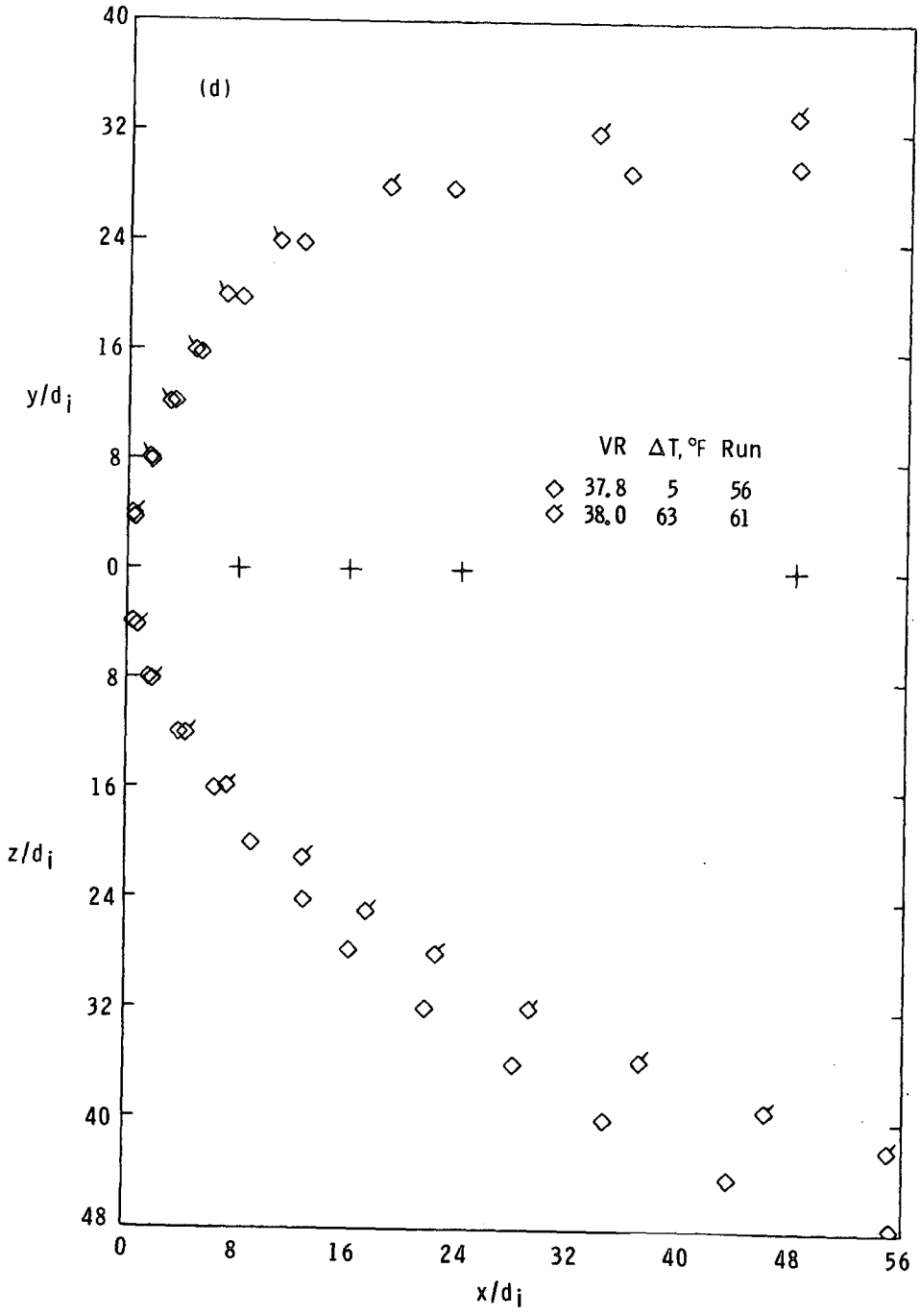

Figure 33.- Concluded.

Photographs of the oblique injection in the upstream ($\alpha_i = 140^\circ$, $\beta_i = 90^\circ$) and downstream ($\alpha_i = 40^\circ$, $\beta_i = 90^\circ$) directions are presented in Figs. 34 and 35, respectively. Trajectory data approximating the centerline of the jet paths in the photographs are shown in Figs. 36 and 37. For the case where $\alpha_i = 140^\circ$ the jet reaches a maximum distance upstream before it proceeds in the downstream direction. The data of Platten and Keffer[14] also illustrate this trend (Fig. 36), even though the injection conditions are somewhat different from the present experiment. The trajectory estimated by Ivanov's empirical expression[13], Eq. (59),

$$\frac{x}{d_i} = \left(\frac{q_\infty}{q_i}\right)^{1.3} \left(\frac{y}{d_i}\right)^3 + \frac{y}{d_i} \cos \alpha_i \qquad (59)$$

is presented for comparison with the present data.

For the case where the jet is injected downstream (Fig. 35) the jet path has less curvature and penetration than was observed for lateral injection (Fig. 19). This is reasonable since the curvature of the trajectory is governed by the forces perpendicular to the jet path, which are proportionately less for $\alpha_i = 40^\circ$ than for $\alpha_i = 90^\circ$. In the limit as $\alpha_i \to 0^\circ$, these normal forces go to zero resulting in the familiar co-axial jet flow process whose trajectory is the X-axis. The present theory adequately estimates the trajectories for injection with $\alpha_i = 40^\circ$ (Fig. 37).

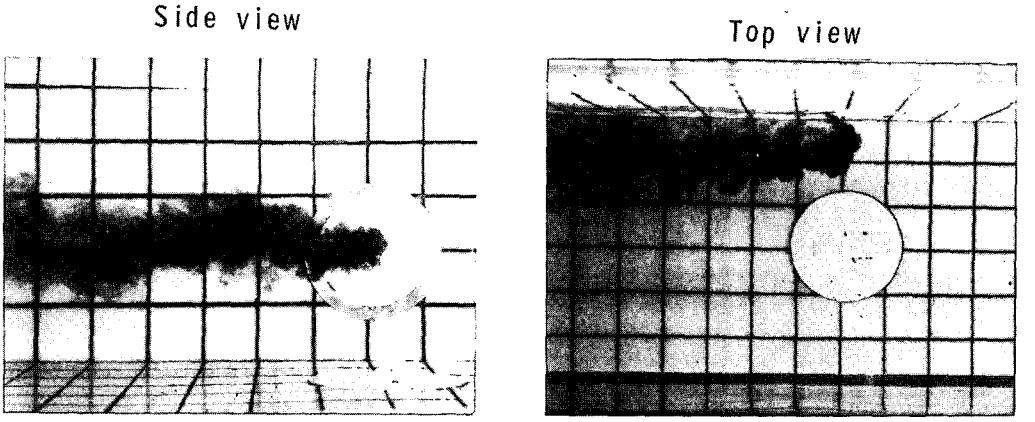

Figure 34.- Photographs of oblique injection in upstream direction ($\alpha_i = 140°$, $\beta_i = 90°$) for VR = 8.7 and $\Delta T_i = 67°F$.

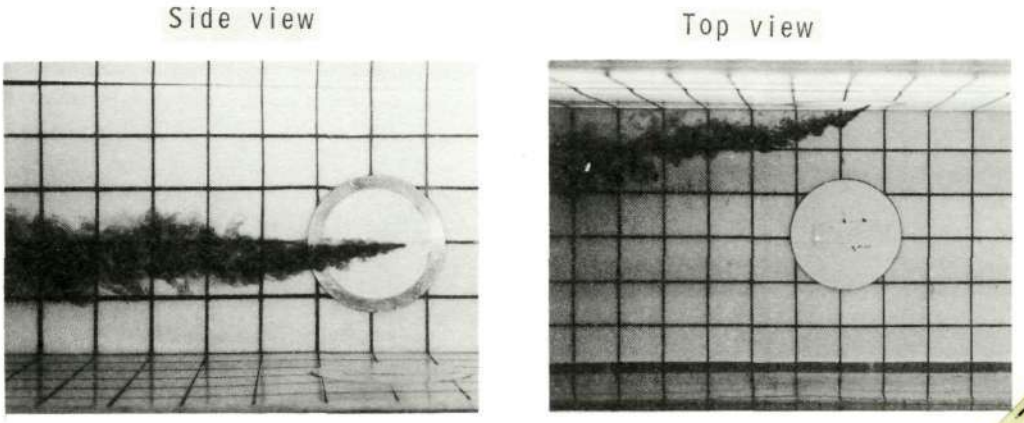

(a) VR = 8.6, ΔT_i = 17°F, Run 69.

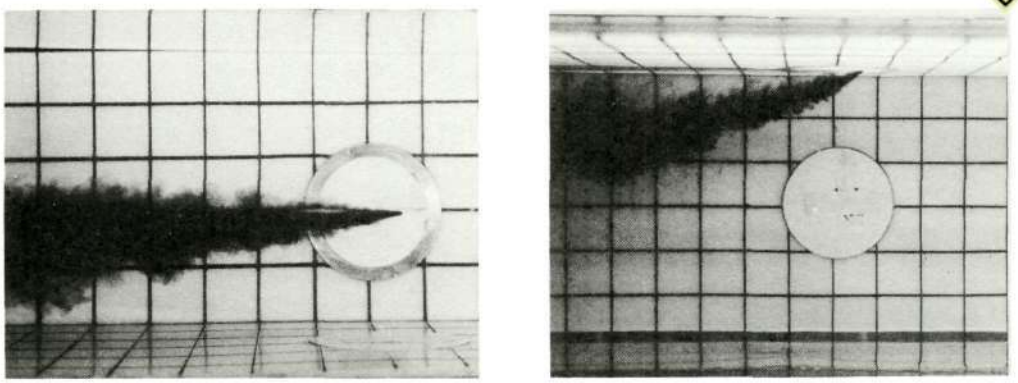

(b) VR = 28.5, ΔT_i = 43°F, Run 71.

Figure 35.- Photographs of oblique injection in downstream direction ($\alpha_i = 40^\circ$, $\beta_i = 90^\circ$) for several injection velocities.

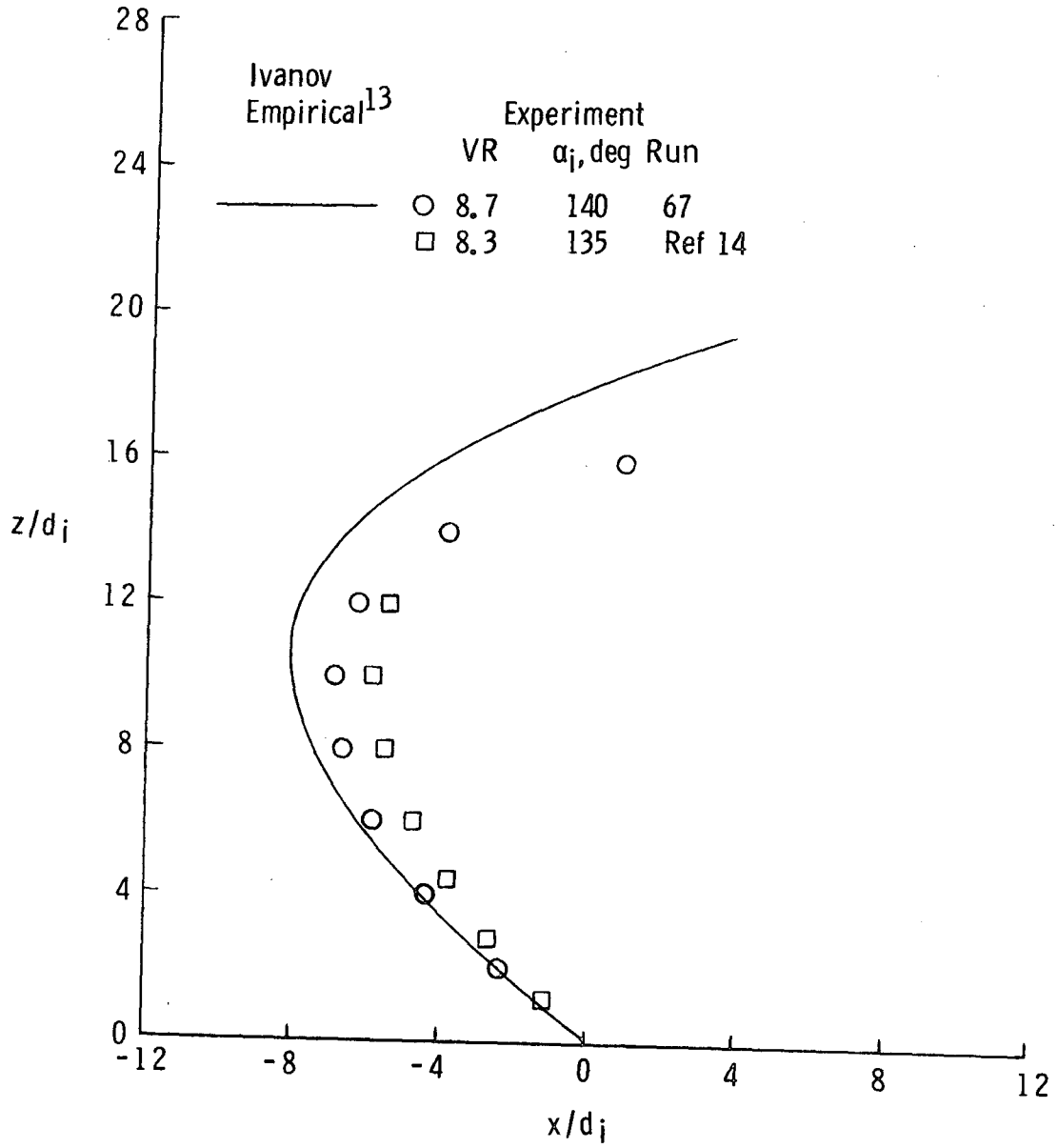

Figure 36.- Experimental trajectory resulting from oblique injection upstream; $\beta_i = 90°$.

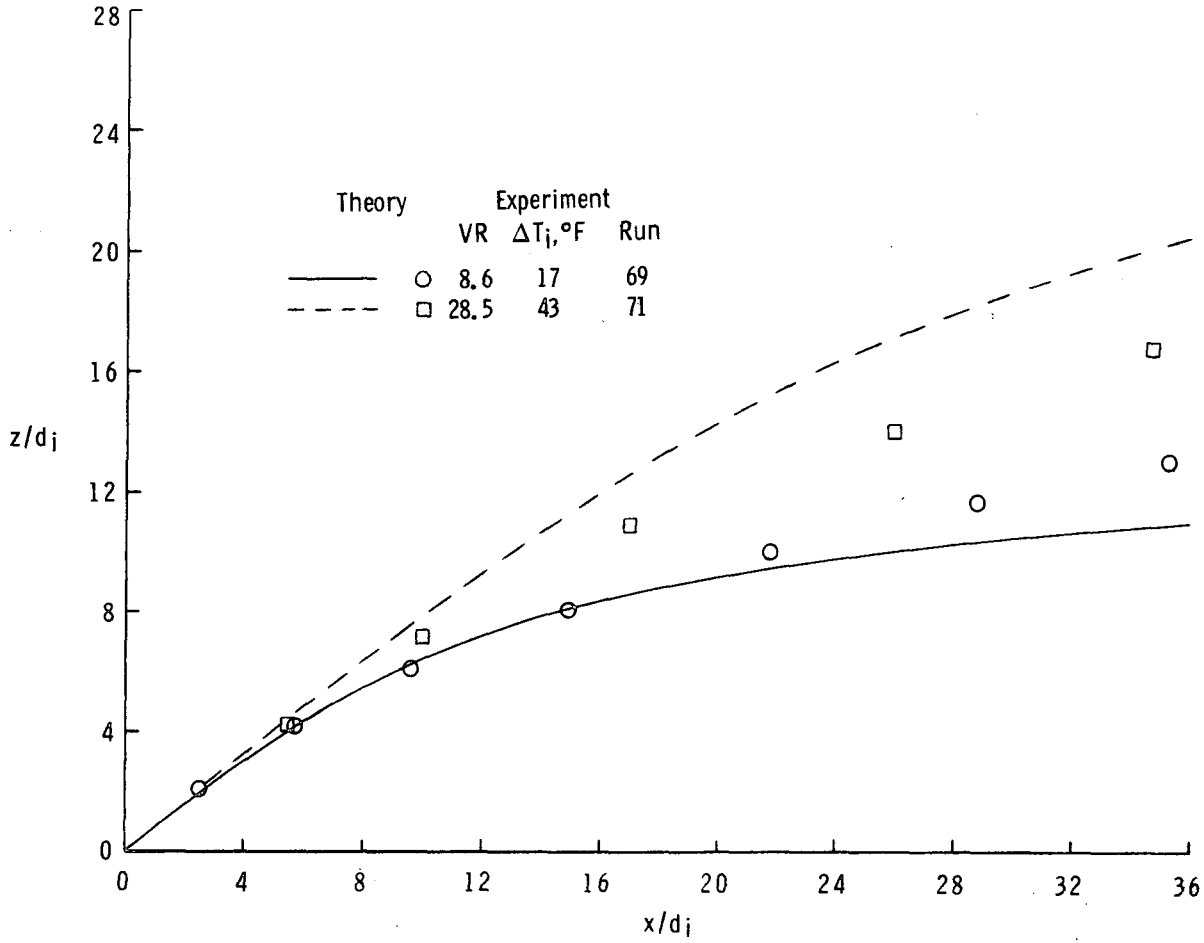

Figure 37.- Experimental and theoretical trajectories for oblique injection downstream; $\alpha_i = 40^\circ$, $\beta_i = 90^\circ$.

X. FURTHER EXAMINATION OF THE THEORY

The purpose of this section is to discuss some of the limitations of the theory developed in Chapter VIII, and to demonstrate its versatility for handling a variety of injection situations. In order to establish the authenticity of the present theoretical method for estimating jet flow properties, its predictions are compared to estimates from other analytical models as well as to experimental data acquired from a number of studies. The last portion of the section presents a theoretical example of a jet with a three-dimensional trajectory.

Two-Dimensional Trajectory

Experimental trajectory data obtained from different investigations of air jets are presented in Figures 38 and 39 and show the two-dimensional paths of the turbulent jet for a range of injection velocities and orientations. These data were obtained from hot-wire measurements and, thus, represent the path that is traced by the maximum velocity in the jet flow. The theoretical trajectories were calculated with the same injection conditions as the experimental data and are in good agreement with the measured trajectories throughout the range of injection velocities and orientations.

Theoretical trajectories calculated with the present theory are compared with theoretical and experimental results of other researchers in Figures 40 - 43. The analytical methods of Abramovich[19], Schetz and Billig[23], and Reilly[24] provide jet trajectories which are comparable to

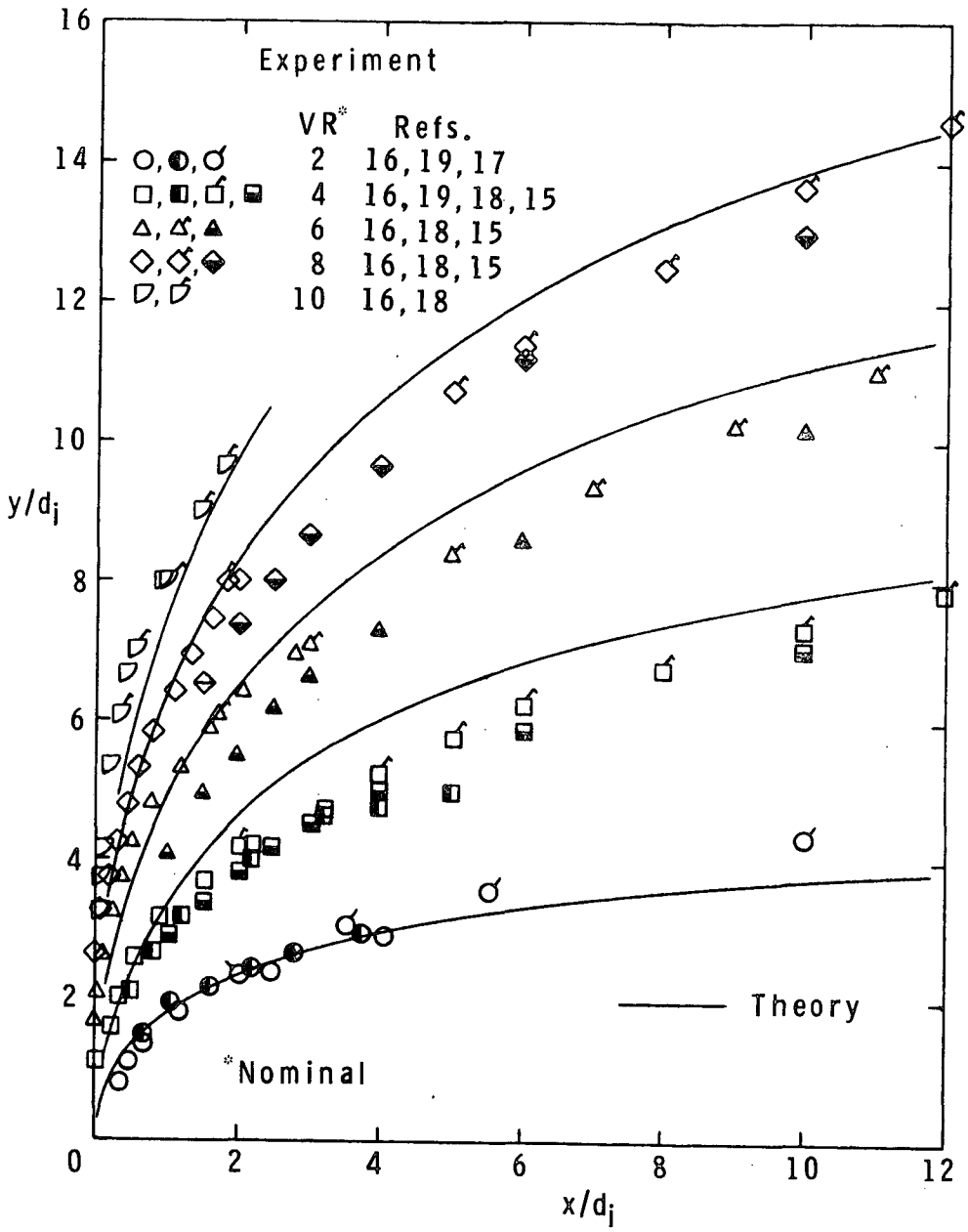

Figure 38.- Experimental and theoretical trajectories of an air jet having a range of injection velocities; $\alpha_i = 90^\circ$, $\beta_i = 0^\circ$.

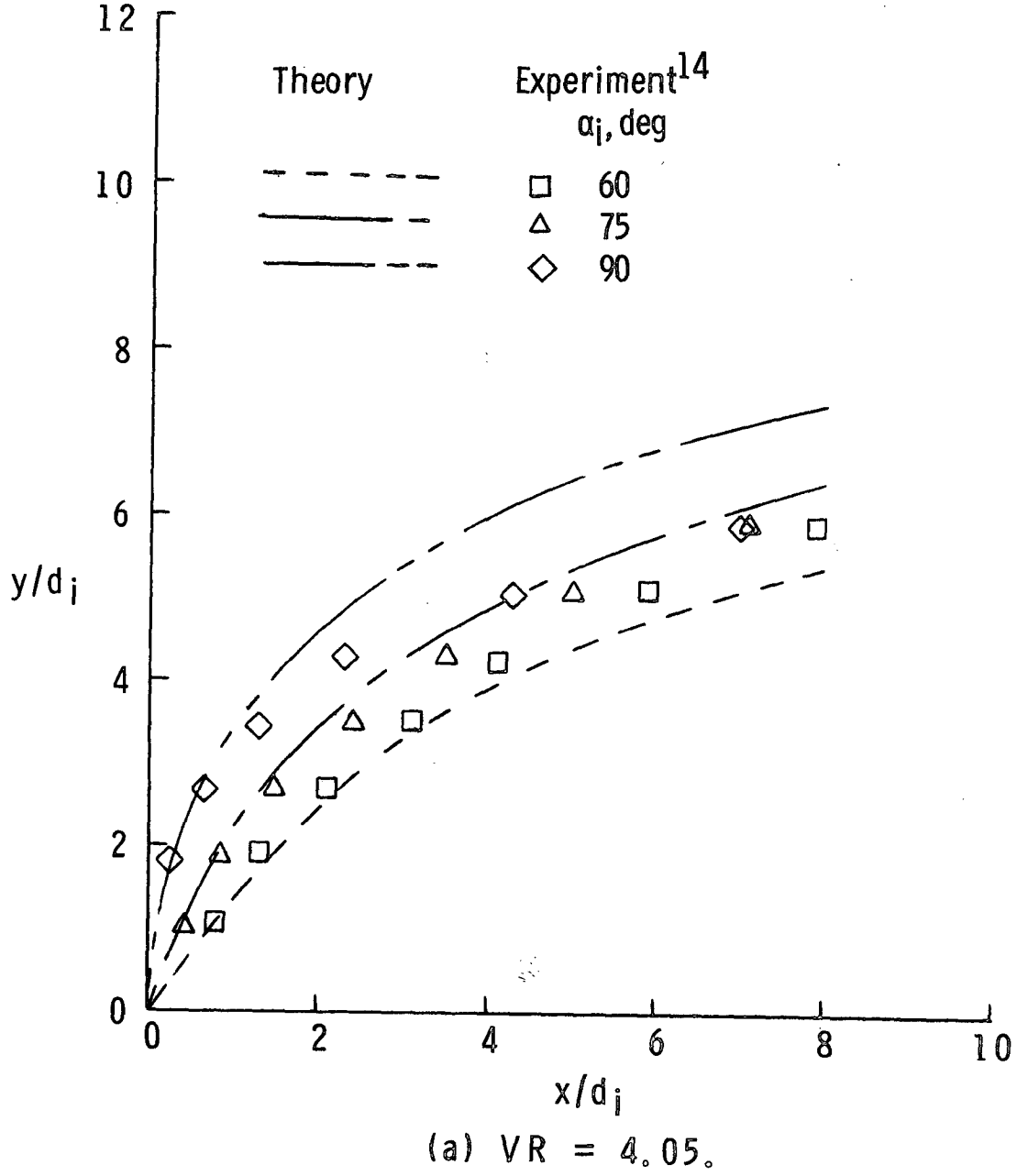

Figure 39.- Effect of injection angle on experimental and theoretical trajectories of an air jet; $\beta_j = 0^\circ$.

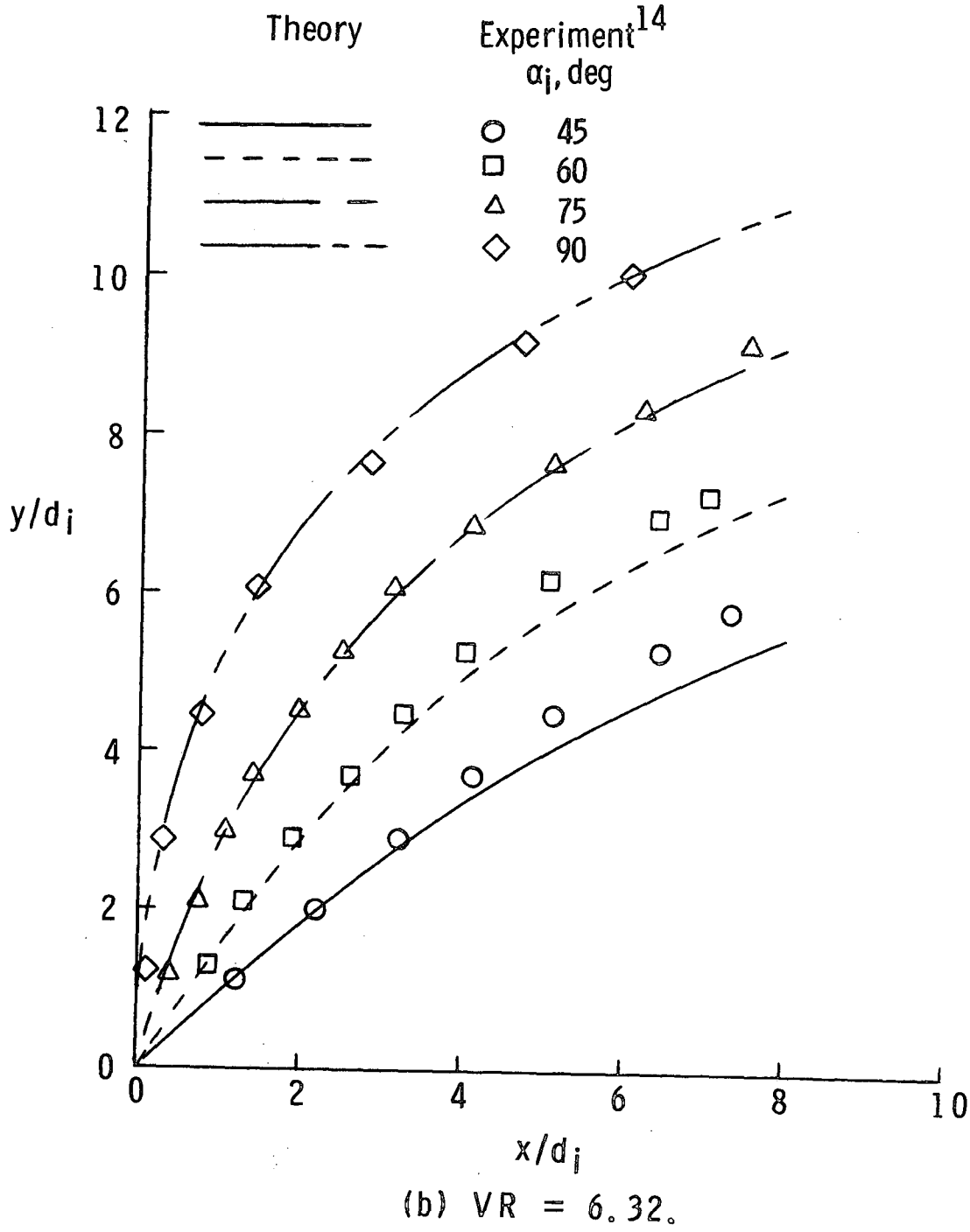

(b) VR = 6.32.

Figure 39.- Continued.

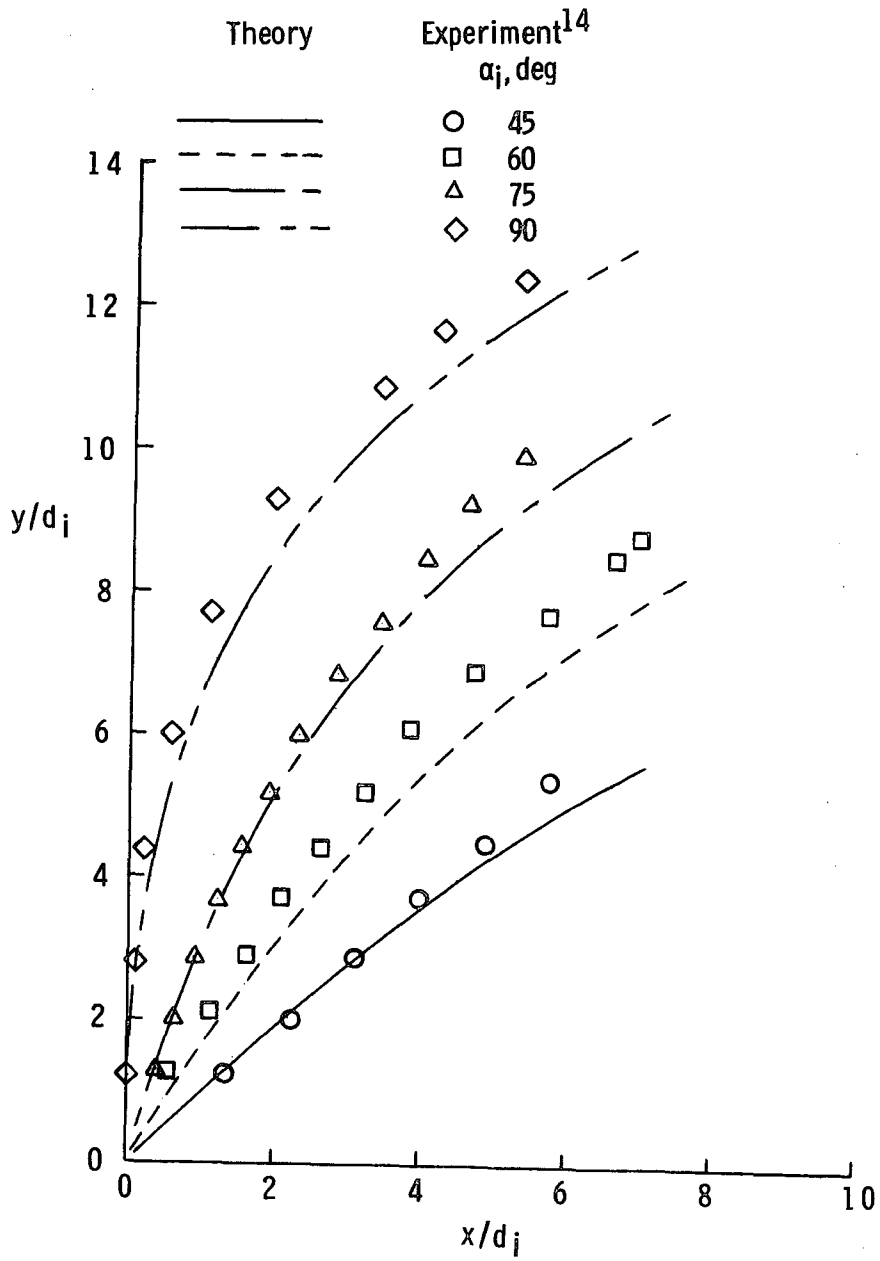

(c) VR = 8.32.

Figure 39.- Concluded.

those of the present theory for the injection conditions presented (Fig. 40 and 41). It is recalled that the theories of Refs. 19, 23, and 24 assumed the growth of the jet cross-sectional area along the trajectory using an empirical expression (see Fig. 6) based on experimental data for $s/d_i \leq 10$. As a consequence, the trajectories predicted by these theories agree quite well with experimental data in the vicinity of the injection point. Care must be exercised in using these theories to estimate jet trajectories and flow properties at large s/d_i values.

One of the best theoretical methods prior to the present is that of Hirst[29], who attempts to account for the complex flow processes that take place as the flow evolves from a momentum jet near the injection point to a buoyant plume at large distances downstream. His results are compared with the present theory in Figs. 42 and 43 for a range of injection velocities and angles. As noted, the present theory is in better agreement with the bulk of experimental data for all of the injection conditions. Since Hirst assumed a Gaussian type of velocity distribution in the jet, his theory is applicable only in the region where the jet flow has become fully developed. This explains why his theoretical trajectories do not originate at the injection point. The experimental data obtained by Gordier[12] are shown in Fig. 42 because Hirst compared his theory with these data in Ref. 29. Gordier's data, however, indicate greater penetration by the jet than is seen for the other data. Ramsey[17] suggested that this discrepancy was probably due to injection into a

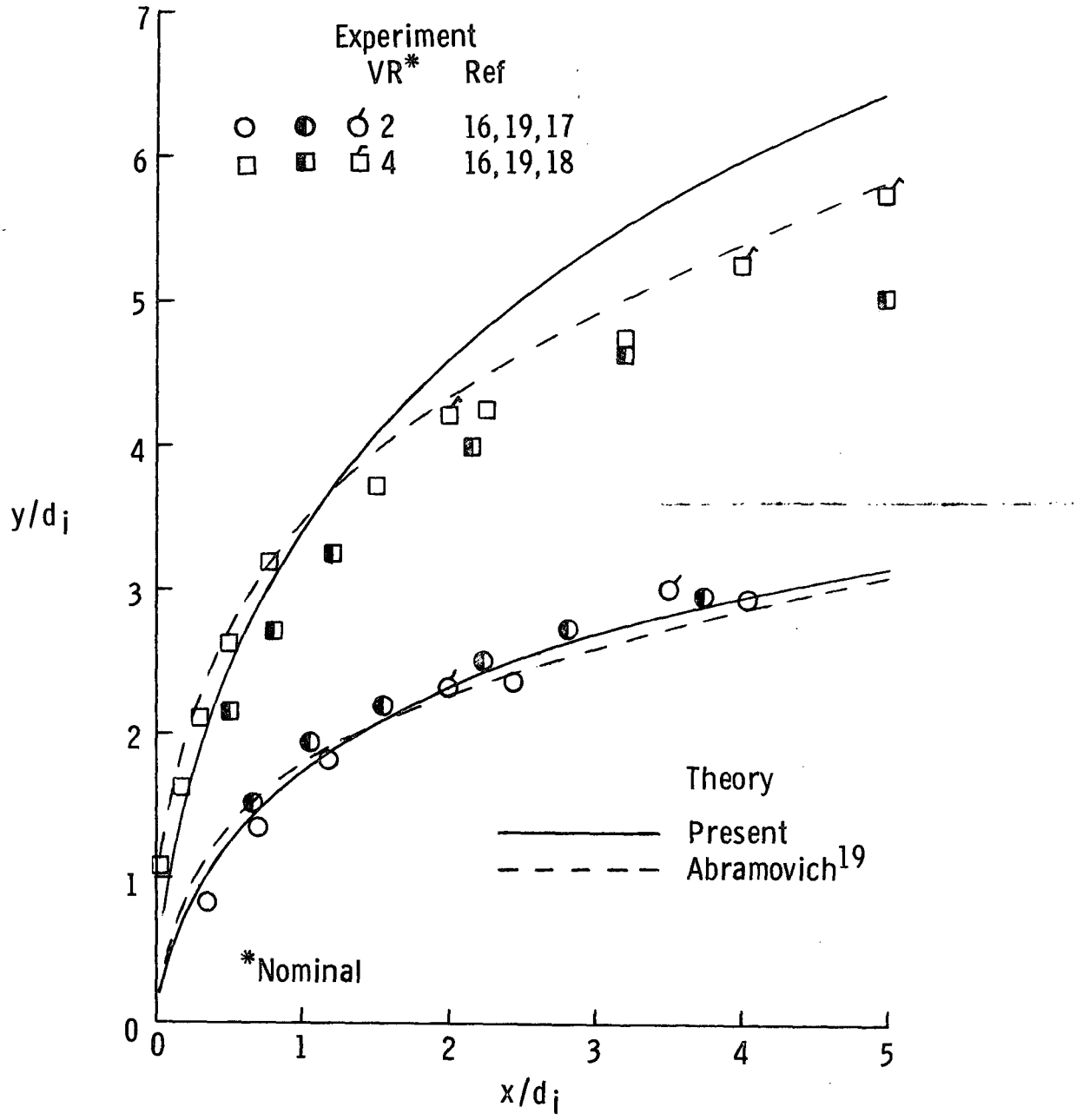

Figure 40.- Comparison of theoretical trajectories estimated by present theory and by Abramovich; $\alpha_i = 90^o$, $\beta_i = 0^o$.

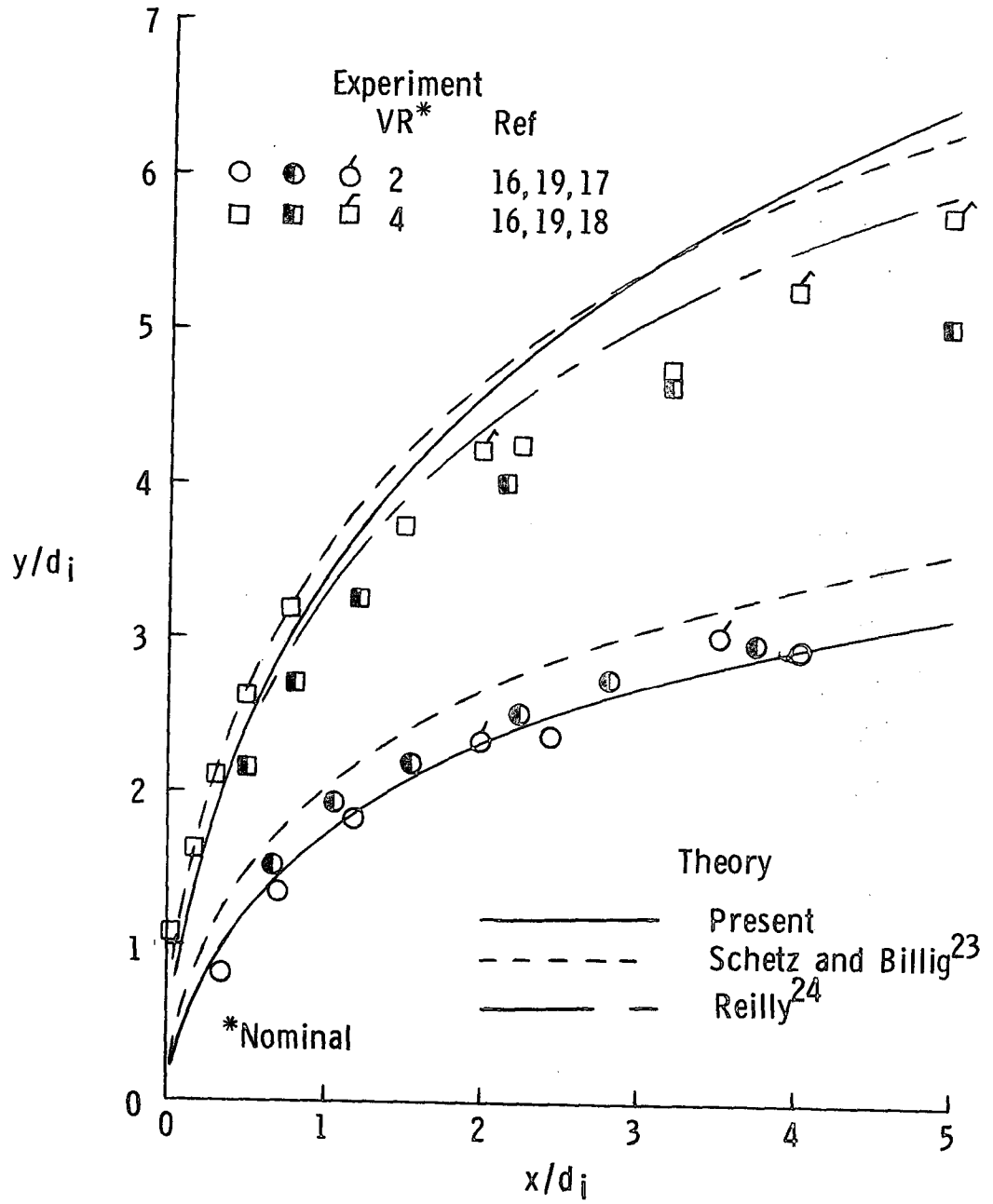

Figure 41.- Comparison of theoretical trajectories estimated by present theory with those of Schetz & Billig and Reilly; $\alpha_i = 90°$, $\beta_i = 0°$.

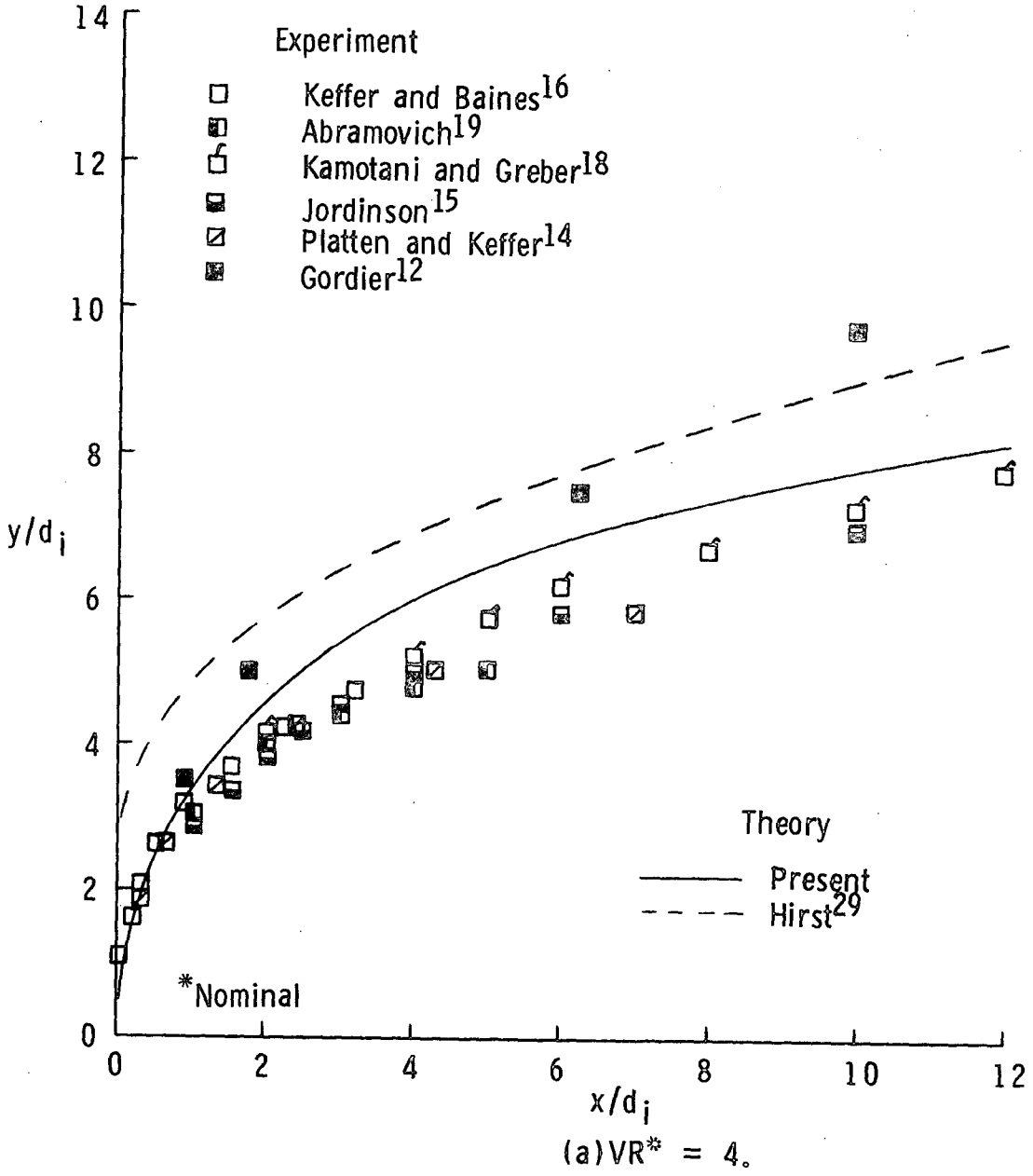

Figure 42.- Comparison of theoretical trajectories estimated by present theory with those of Hirst for normal injection; $\alpha_i = 90^\circ$, $\beta_i = 0^\circ$.

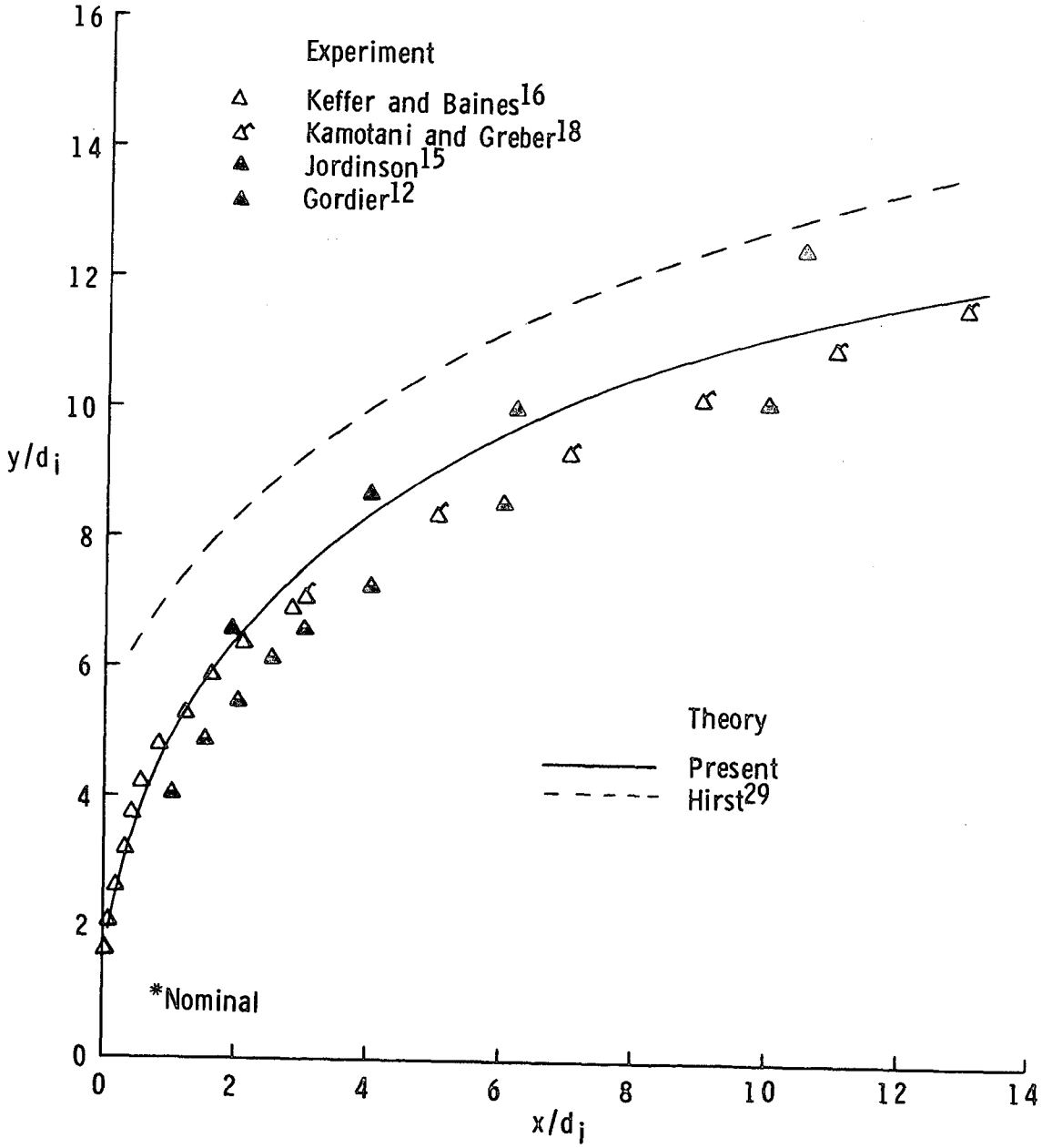

(b) VR* = 6

Figure 42.- Continued.

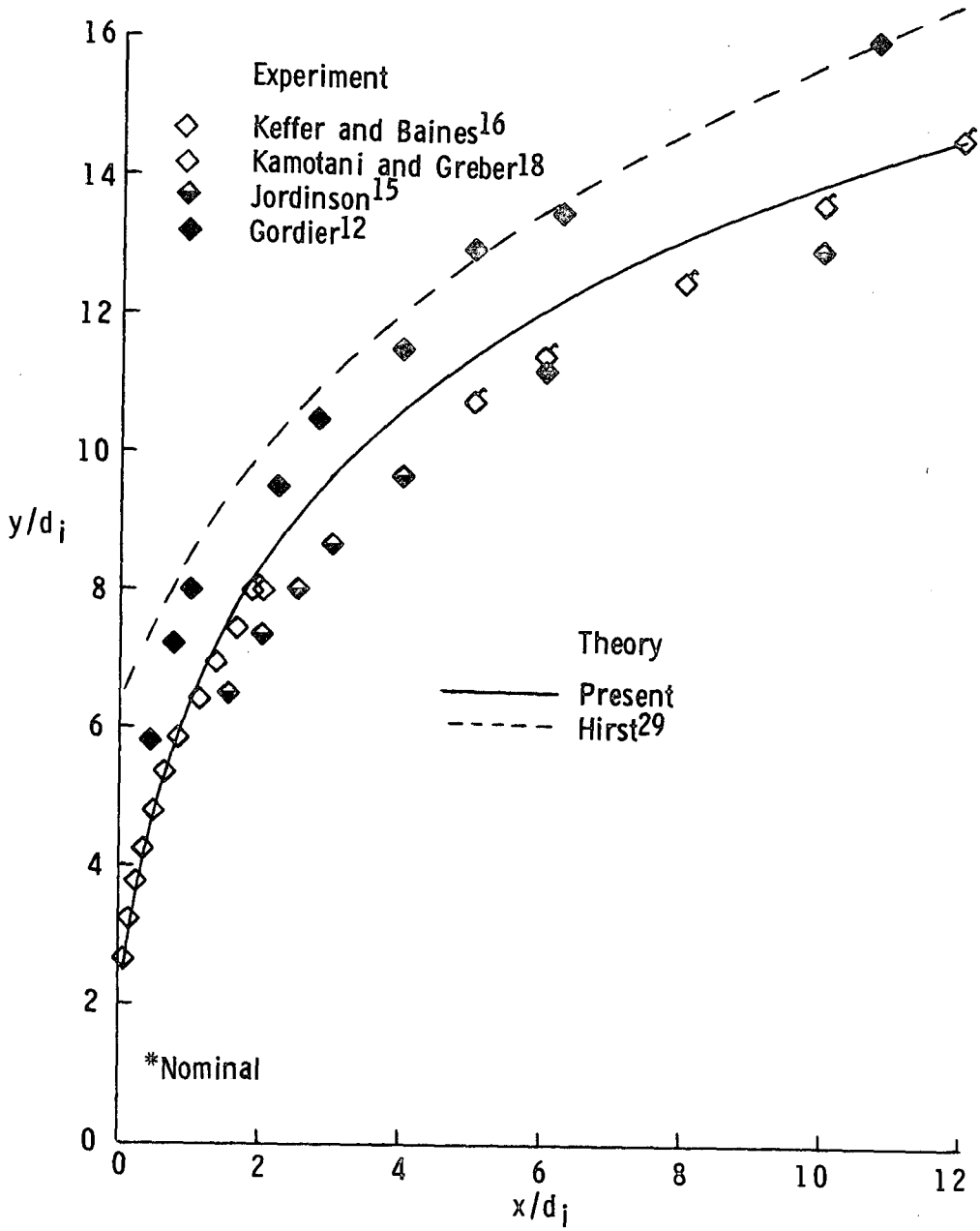

(c) VR* = 8.

Figure 42.- Concluded.

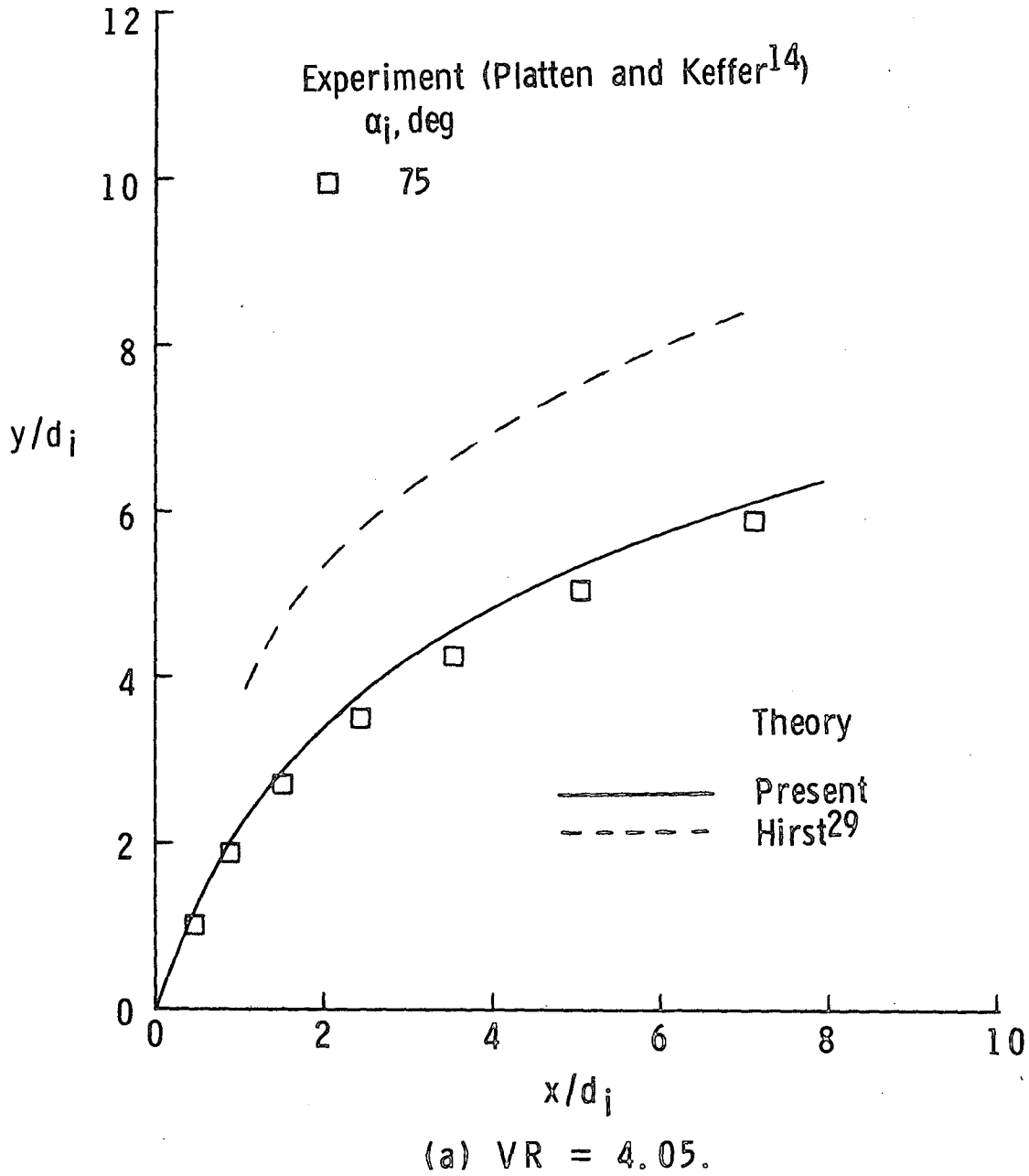

(a) VR = 4.05.

Figure 43.- Comparison of theoretical trajectories estimated by present theory with those of Hirst where $\alpha_i \neq 90^\circ$, $\beta_i = 0^\circ$.

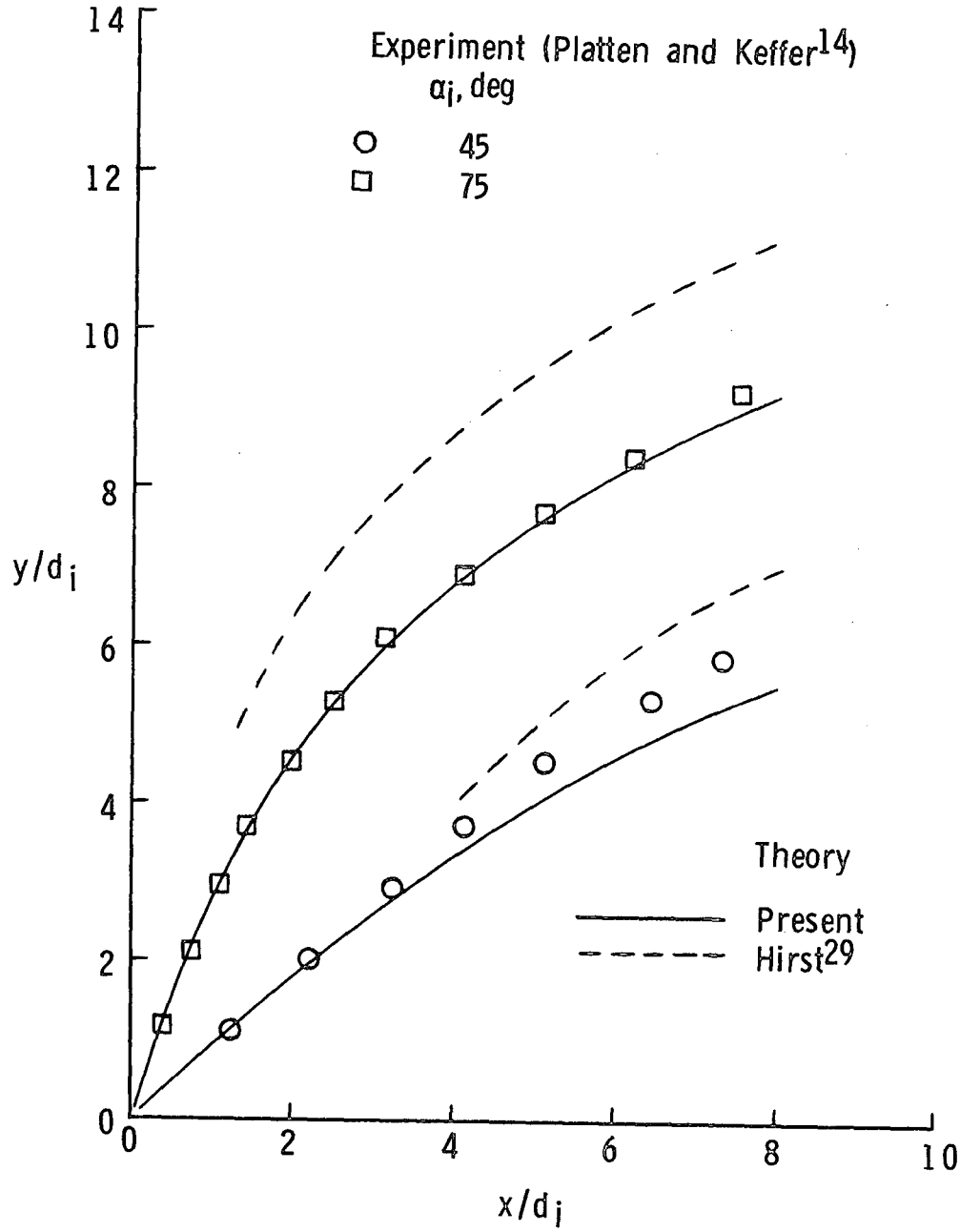

(b) VR = 6.32.

Figure 43.- Continued.

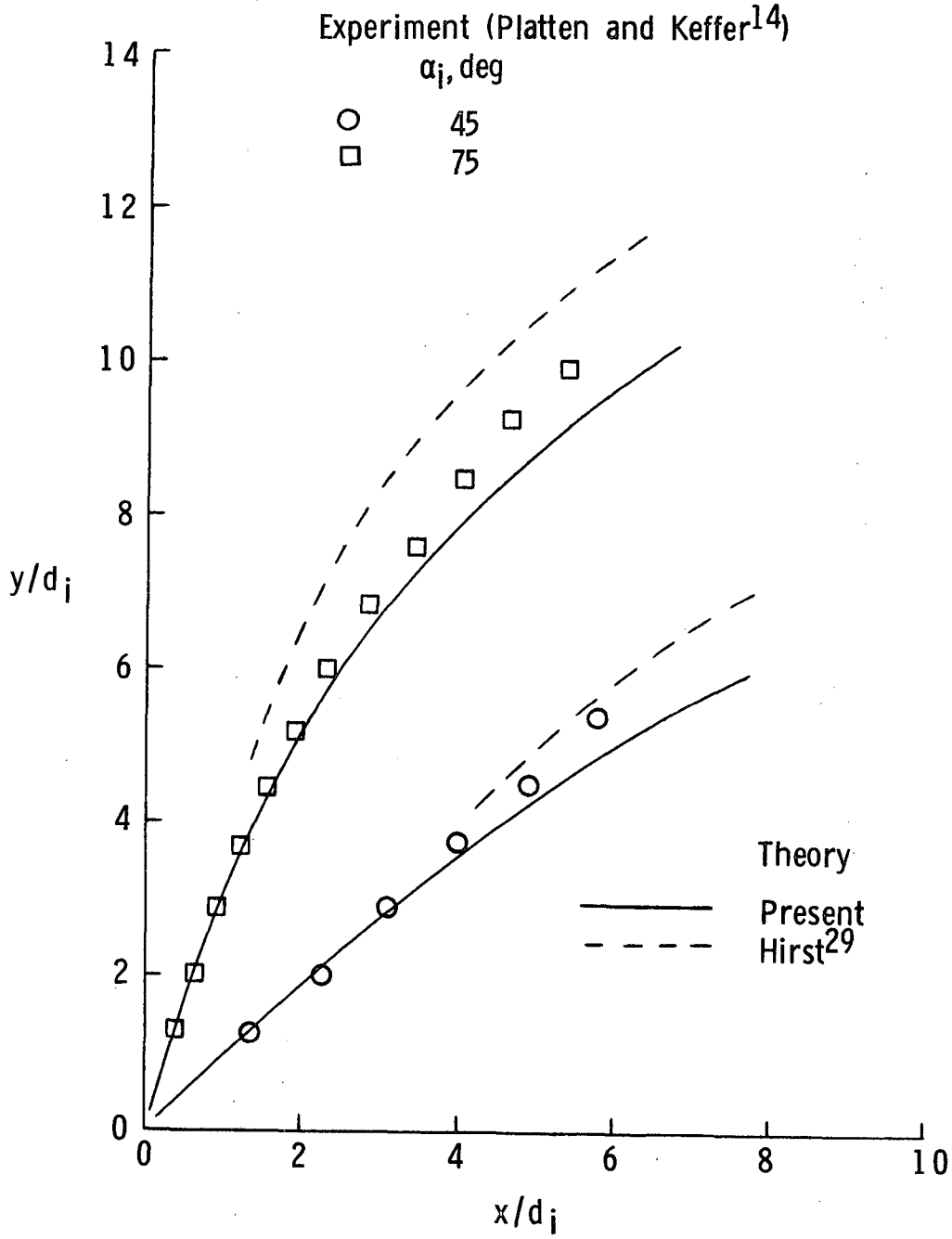

(c) VR = 8.32.

Figure 43.- Concluded.

cross flow with a very thick boundary layer. This trend will be shown later in this chapter.

Jet Flow Properties

Examples of some of the theoretical flow properties obtained in the process of solving the governing conservation equations are presented in Figures 44 to 49. It was observed in the experimental portion of the present study that the cross-sectional area of the jet continually increases as the jet proceeds along the trajectory. This trend is shown in Fig. 44 where the jet area, normalized by the jet area at the injection point, is plotted as a function of s/d_i. The data points acquired from Kamotani and Greber's work[18] were obtained by measuring the area encompassed by a contour of jet velocity where the velocity excess had decreased to 10% of the maximum excess with respect to the free-stream velocity component tangent to the jet flow. It is noted that Keffer and Baines[16] also defined the edge of the jet flow in this fashion. Experimental areas for the VR = 30 case were obtained from the photographic information in Fig. 19 by assuming the cross-sectional shape to be a 5:1 ellipse and by measuring the minor axis. The data in Fig. 44 indicate that an increase in injection velocity (VR) results in larger rates of area growth with s/d_i.

Theoretical areas are shown for comparison and predict the same trends as the experimental areas, however, the theory underestimates the magnitude of the area growth experienced by the jet for the range of injection velocities shown. It should be mentioned that these

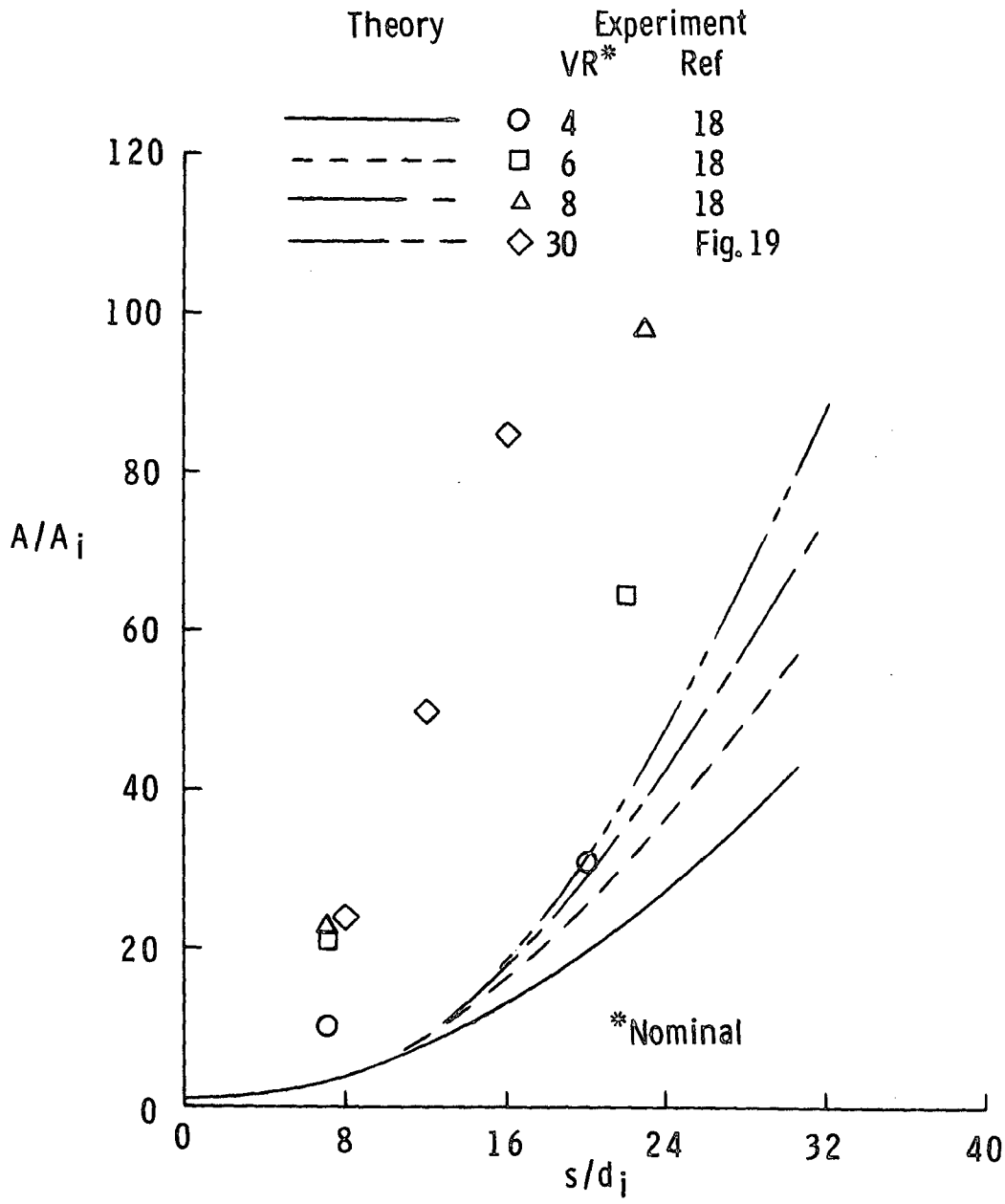

Figure 44.- Variation of jet cross-sectional area with distance along trajectory for a range of injection velocities, $\alpha_i = 90^\circ$. (Values from Ref. 18 are measurements of the area bounded by a contour of jet velocity).

theoretical estimates of jet area are very sensitive to the amount of entrainment, small increases in entrainment resulting in large increases in the cross-sectional areas. It will be shown shortly that the entrainment model used in the theory could be improved, which would result in better agreement between the theory and the experiment in Fig. 44.

As the area occupied by the jet fluid grows with increase in distance along the trajectory, the jet velocity correspondingly decays. This is illustrated in Fig. 45 where the jet velocity is nondimensionalized by the injection velocity and where the V_∞/V_i values for the various injection conditions are depicted by the arrows. The experimental data that are shown are measurements of the maximum jet velocity for VR = 4, 8, and ∞ (free jet). These data indicate that the trend for velocity decay is similar for all injection velocities.

For the VR = 4 case there is a short distance (potential core) where the maximum jet velocity remains equal to the injection velocity. Further increase in s/d_i results in continued decreases in jet velocity which eventually approaches the free-stream velocity value (V_∞/V_i). Increasing injection velocity increases the potential core length, a maximum value being obtained for the free jet[18], and decreases the value of V_∞/V_i that the jet velocity must approach (note arrows), $V_\infty/V_i = 0$ for the free jet. The combination of these experimental trends helps in comprehending the theoretical velocity decay curves presented in the figure for a range of injection velocities.

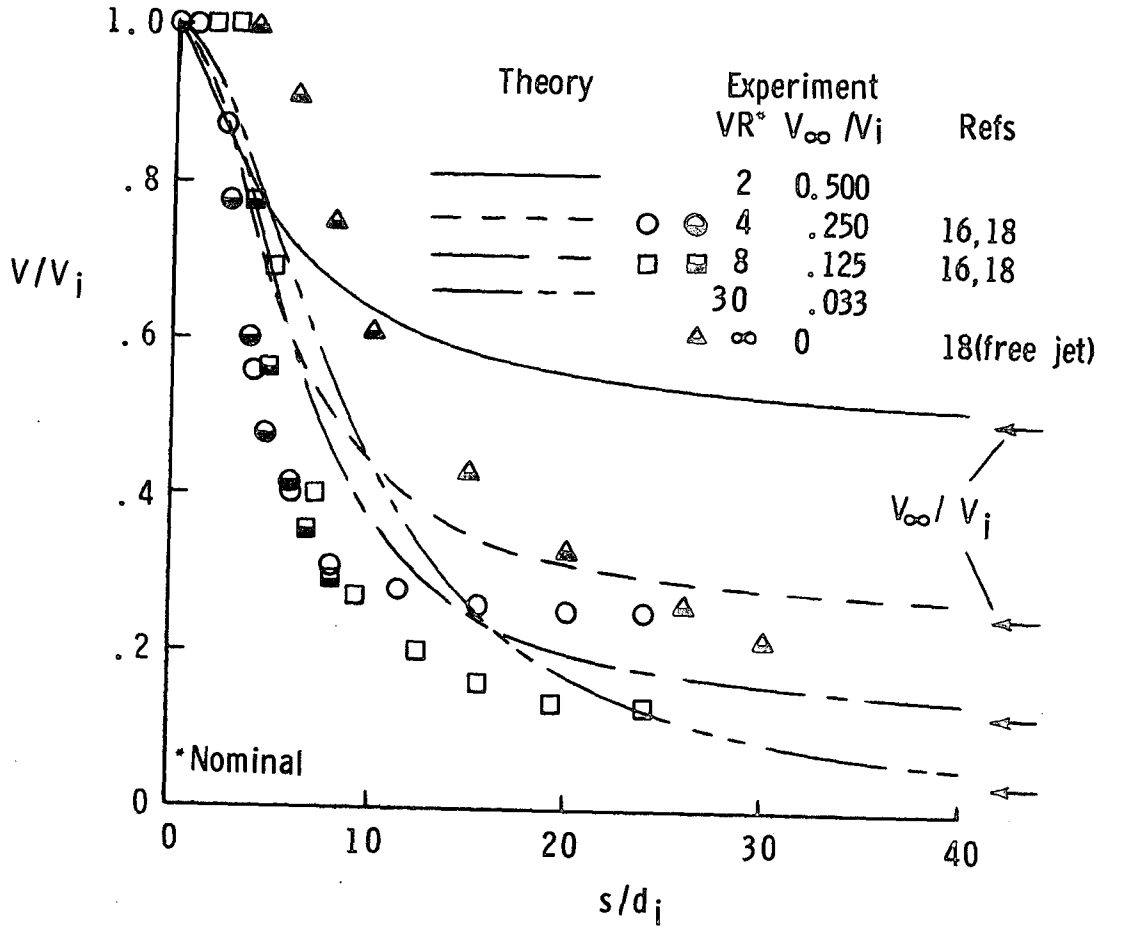

Figure 45.- Effect of injection velocity on jet velocity decay with increase in distance along trajectory; $\alpha_i = 90^\circ$.

Comparing the theoretical velocities with the experimental data for VR = 4 and 8, it is observed that the theory predicts V/V_i values that are greater than the experimental values and which approach V_∞/V_i at a slower rate. The fact that the mathematical model estimates average jet velocities explains why the theory predicts a decrease in velocity immediately after injection compared to the existence of a potential core demonstrated by the maximum velocity measurements.

The effects of increased injection velocity on velocity decay, which were discussed in Fig. 45, are put into perspective in Fig. 46 by plotting the velocity as a velocity deficit, where the difference between the jet and free-stream velocity is divided by the difference at the injection point. Presenting the results in this fashion causes the velocity deficit to approach zero as $V \to V_\infty$. As noted, an increase in VR results in a corresponding increase in experimental velocity deficit at a given distance on the trajectory. This trend also essentially applies to the theoretical velocity deficit variations. Keffer and Baines[16] observed that velocity deficit showed a universality (i.e. independent of VR) when plotted against the distance from the virtual source of the jet flow.

The variation of theoretical mass flux in the jet with distance along the trajectory is shown in Fig. 47 for a range of injection velocities. As would be expected from our consideration of mass conservation in Chapter VIII, the mass flow in the jet increases with increased distance along the trajectory, the higher mass flows occurring

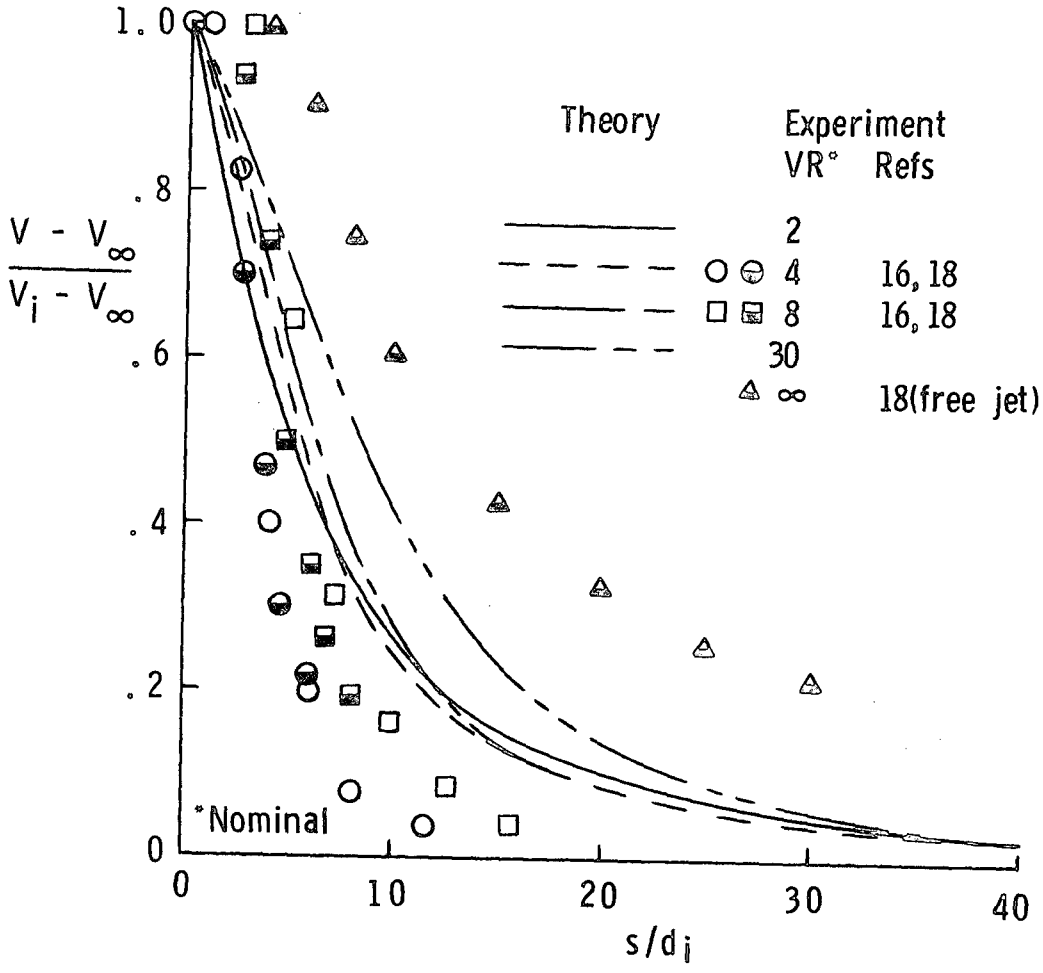

Figure 46.- Variation of jet velocity deficit with distance along trajectory for range of injection velocities; $\alpha_i = 90^\circ$.

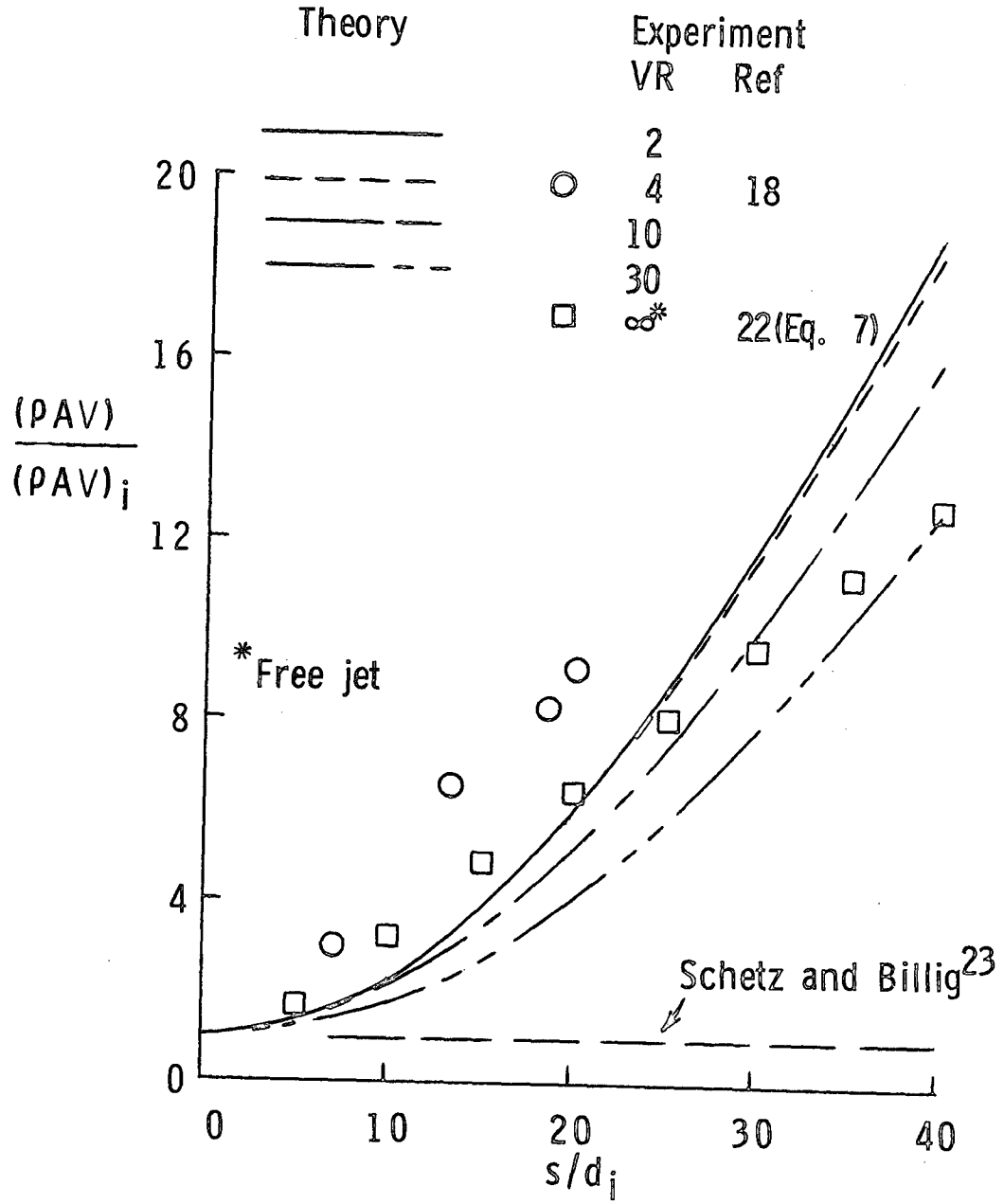

Figure 47.- Variation of mass flow in jet with distance along trajectory for range of injection velocities; $\alpha_i = 90^o$.

for the lower injection velocities. This increase in mass flow with increase in s/d_i is demonstrated by experimental data[18] for VR = 4, although the measured values indicate higher mass flows in the jet than are predicted by the theory. A further indication that the theoretical mass flows should be greater than they are is provided by the measurements of mass flow in a free jet.[22] The fact that these mass flows are less than the experimental values for the jet with VR = 4 supports the premise that the entrainment rate for a jet in a cross flow should be greater than that for a free jet. At certain values of s/d_i the disturbing situation exists that the theory predicts mass flows that are less than the free-jet values. Improvements in the entrainment model used in the current analytical effort will provide improved estimates of the jet's mass flow, and consequently will yield more realistic cross-sectional area and velocity decay results than were observed in the last few figures. In the study by Schetz and Billig[23], the mass flow was assumed to remain constant at the initial value. Their assumption is represented by the horizontal line in the figure and becomes more realistic nearer to the injection point.

The variation of theoretical jet momentum flux with distance along the trajectory is shown in Fig. 48 for a range of injection velocities. The jet momentum, normalized by the value at the injection point, is seen to decrease immediately after injection, reaching a point on the trajectory where it attains a minimum value, after which it increases for the remainder of the trajectory. This trend occurs because the component of momentum in the y- and x-directions decreases

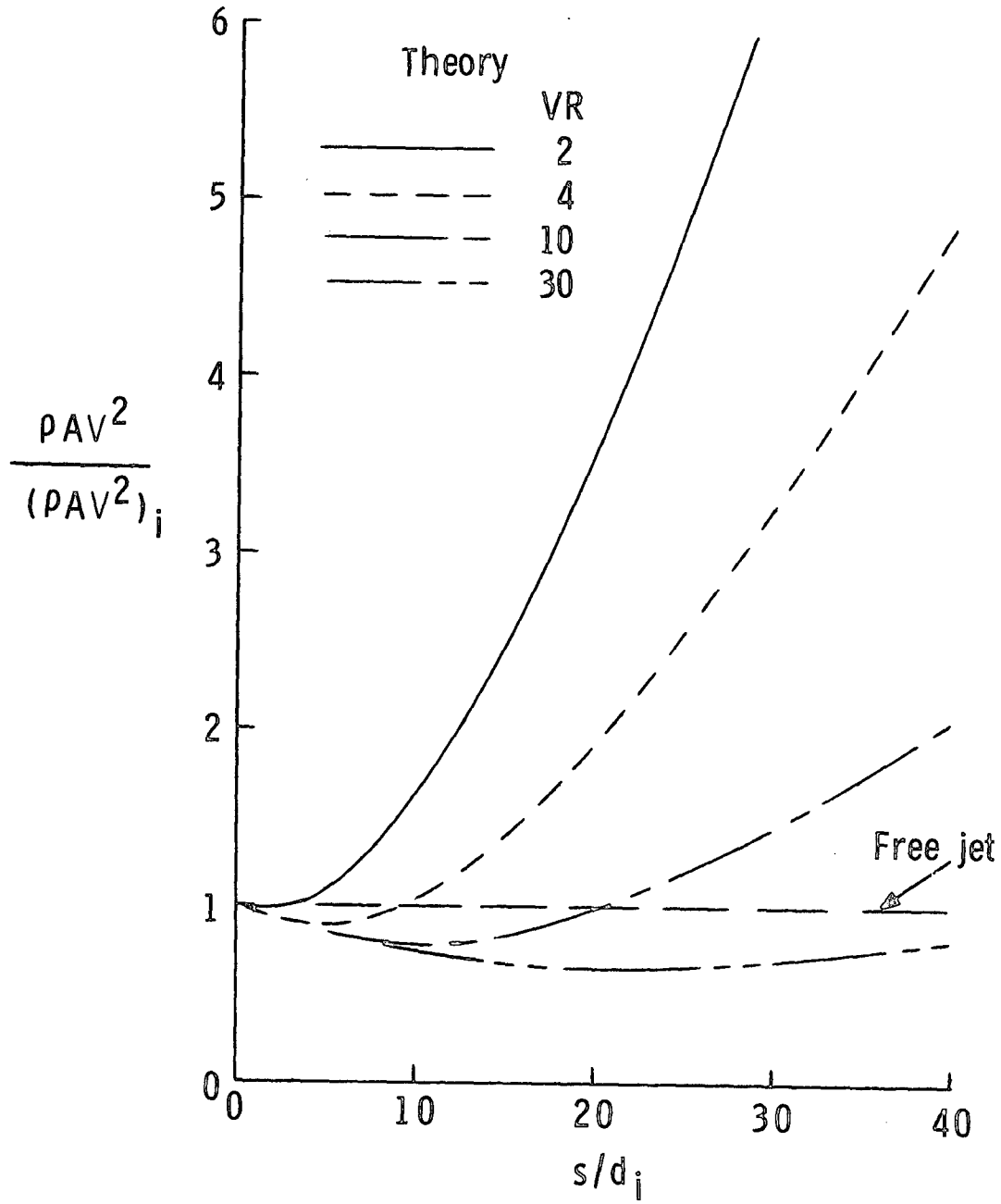

Figure 48.- Variation of theoretical jet momentum with distance along trajectory for range of injection velocities; $\alpha_i = 90^\circ$, $\beta_i = 0^\circ$.

and increases, respectively, along the trajectory of a jet that is injected normally into a free-stream flow. For this situation ($\alpha_i=90^o$) the y- and s-momenta are identical at the injection point, so that the natural decrease of y-momentum with increase in s/d_i results in a decrease in s-momentum during the initial phase of the injection process. As the jet axis becomes parallel to the free-stream direction, the y-momentum of the jet approaches zero and the x- and s-momenta become synonymous.

The continual decrease of y-momentum along the trajectory of a jet injected normal to a cross flow is illustrated in Fig. 49, where experimental data of Kamotani and Greber are presented for several injection velocities. As you would expect, the y-momentum is largest (at a given s/d_i location) for the jet with the highest injection velocity. These trends of y-momentum with increase in s/d_i and VR are also reflected by the theoretical results of the present study. Abramovich assumed in his analytical development that the component of jet momentum perpendicular to the free-stream direction (y-momentum) remains constant along the trajectory. The fallacy of this assumption is particularly obvious at large s/d_i distances.

Free-stream Nonuniformities

One advantage of the present theory is its flexibility for investigating parameters which affect the trajectory and flow properties of the injected jet. Not the least important of these parameters are the free-stream velocity and temperature fields into which the jet is injected. Up until now the free-stream velocity and

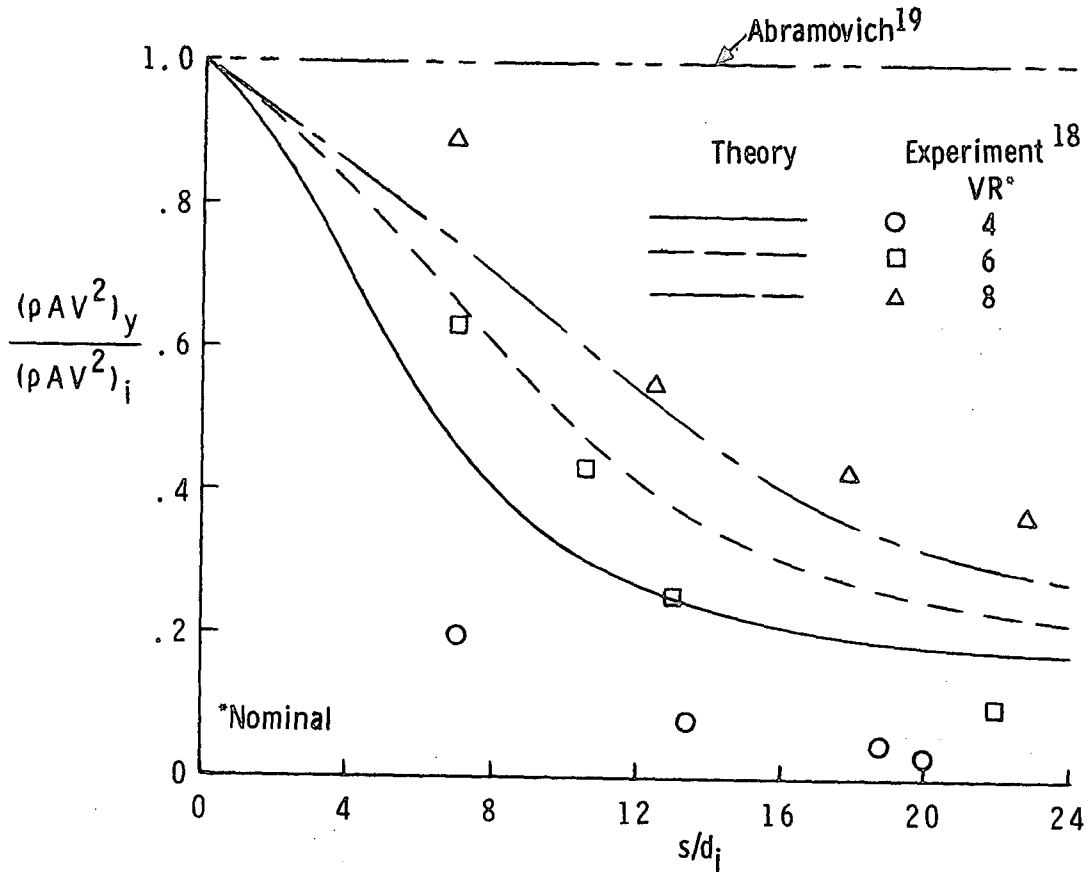

Figure 49.- Effect of injection velocity on the change of jet y-momentum with distance along trajectory; $\alpha_i = 90^\circ$, $\beta_i = 0^\circ$.

temperature have been assumed constant, but the next few figures will demonstrate some of the effects resulting from relaxing these assumptions.

For the purpose of this illustration, the jet is assumed to inject vertically into a free-stream flow which has a boundary-layer type of velocity distribution in the y-direction (Fig. 50(a)). Similar to the exercise in Appendix A, a Karman-Pohlhausen velocity function is described from the injection surface to the boundary-layer edge, which is taken to be $8d_i$ to correspond to the vertical injection tests of the present study. At larger values of y/d_i the velocity is assumed to be constant having the same value as the V_∞ used for the uniform free-stream velocity case, shown in Fig. 50(b). Figure 51 shows that injection into the nonuniform free-stream velocity field results in further penetration by the jet into the cross flow than injection into the free stream with the uniform velocity field. Coincident with this, the jet velocity decay is essentially unaffected, while the jet cross-sectional area and momentum are less at any given distance along the trajectory. It was noted that the effect of free-stream velocity nonuniformity on jet trajectory diminished with increase in injection velocity.

The linear temperature gradient shown in Fig. 52 is used to demonstrate the effect of injecting a heated jet vertically into a free-stream flow having constant velocity and nonuniform temperature fields. The free-stream temperature at the injection surface ($72^\circ F$) is equivalent to the value used for the uniform free-stream

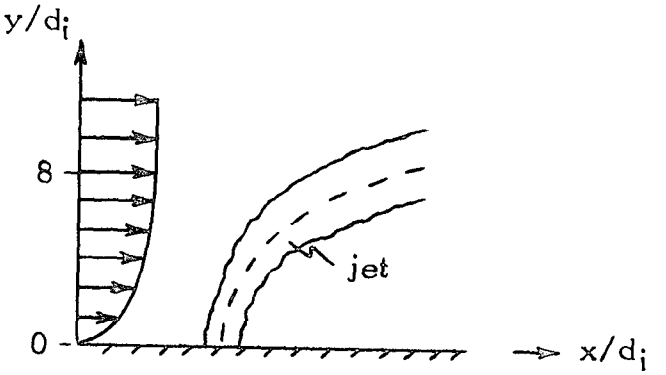

$0 \leq y/d_i \leq 8 \qquad V_\infty/V_i = 3/80\ (y/d_i) - 1/5120(y/d_i)^3$

$y/d_i \geq 8 \qquad V_\infty/V_i = 0.20$

(a) Nonuniform free-stream velocity

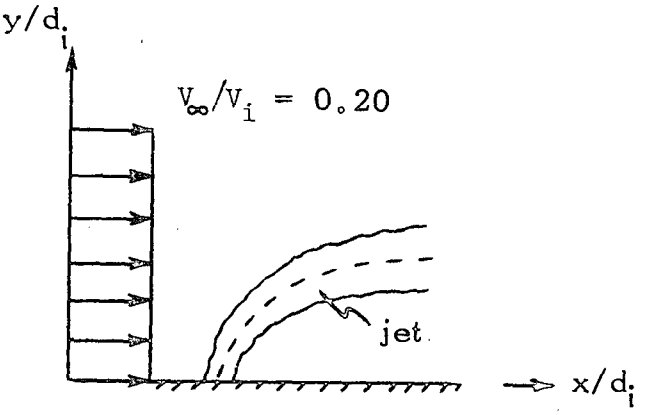

(b) Uniform free-stream velocity

Figure 50.- Uniformity of free-stream velocity field; $\alpha_i = 90^\circ$, $\beta_i = 0^\circ$.

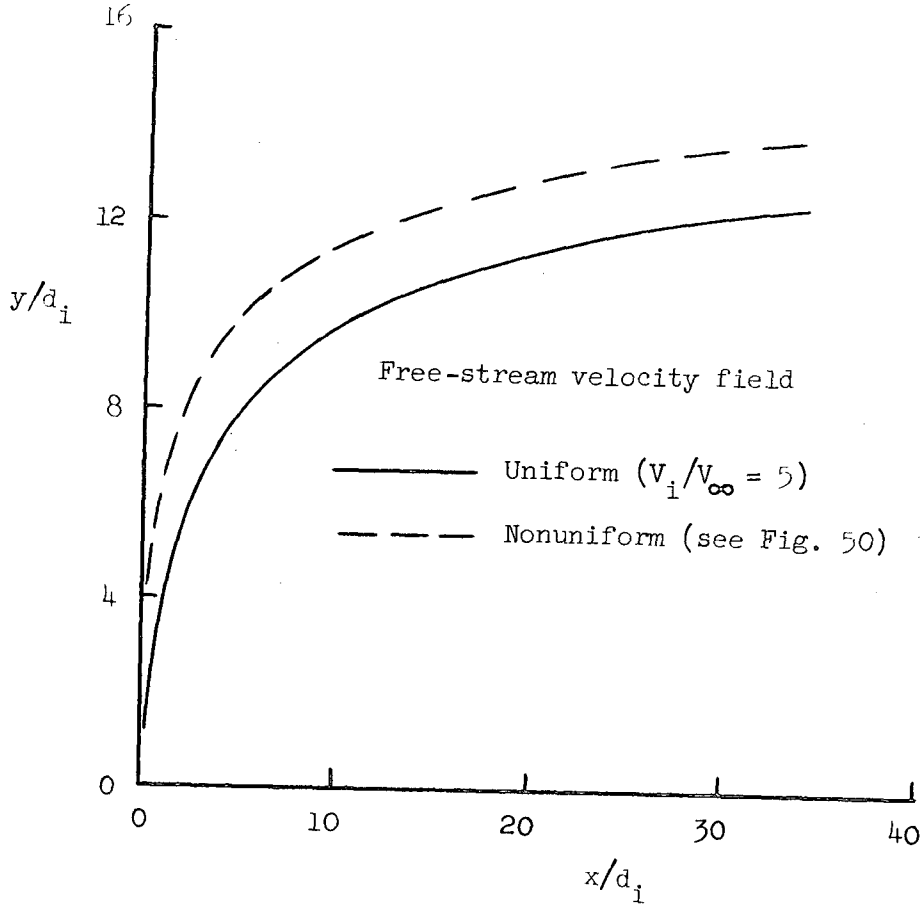

Figure 51.- Effect of free-stream velocity nonuniformity on theoretical trajectory; $\alpha_i = 90^\circ$, $\beta_i = 0^\circ$.

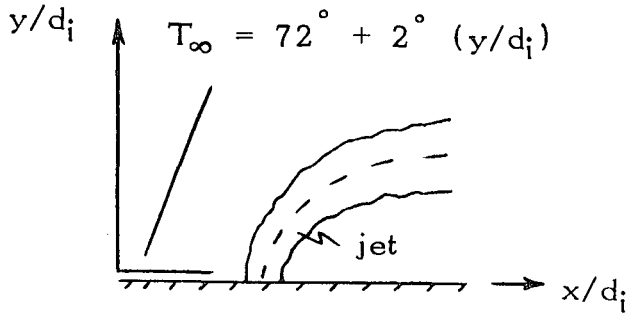

Nonuniform free-stream temperature

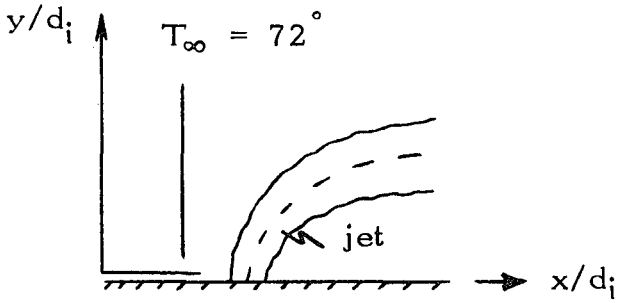

Uniform free-stream temperature

Figure 52.- Uniformity of free-stream temperature field; $\alpha_i = 90^\circ$, $\beta_i = 0^\circ$.

temperature case. Injecting a jet with initial temperatures of 72°F and 92°F into a free-stream flow having a uniform temperature results in the trajectory and temperature curves shown in Fig. 53. The combination of the jet flow having a very large Froude number and experiencing a rapid heat loss results in no change in the trajectory. This result agrees with the experimental observations made earlier in the paper as well as with the data of Kamotani and Greber. As noted in the figure, the temperature for the heated jet decreases along the trajectory until it reaches the free-stream value (T_∞/T_j). Injection of the heated jet into the free-stream flow with a temperature gradient results in a trajectory similar to that obtained by injecting the heated jet into the uniform temperature field. There is a definite difference, however, in the temperature curves resulting for these two injection conditions, where the nonuniform T_∞ situation results in higher jet temperatures because of the larger values of T_∞ that the jet flow "sees" as it penetrates into the cross flow. Heat is initially lost from this jet flow until a point is reached on the trajectory where a heat gain is experienced.

Three-Dimensional Trajectory

Up until now all of the theoretical trajectories that have been presented are, by definition, two dimensional, i.e. they lie in a single plane. The next few figures are presented to illustrate a three-dimensional path that results for a jet injected normal ($\alpha_j = 90°$) to the mainstream, and rotated 45° away from the vertical

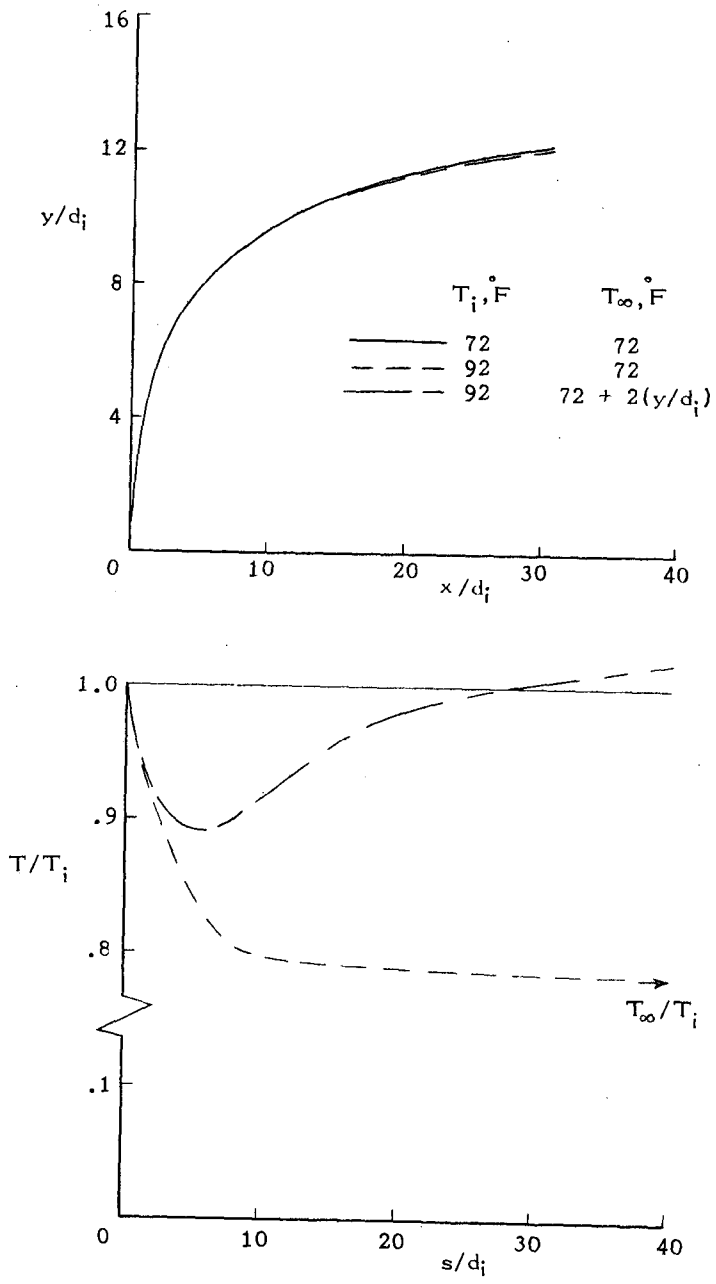

Figure 53.- Effect of free-stream temperature nonuniformity on theoretical jet trajectory and temperature; VR = 5, $\alpha_i = 90^\circ$, $\beta_i = 0^\circ$.

when buoyancy is significant. An injection situation similar to this was observed in Fig. 31, where the theoretical trajectories are actually two dimensional because the Froude number on the jet flow is so large, or in other words, the buoyancy force is small compared to the momentum forces. In order to obtain a three-dimensional trajectory, particularly near the injection point, the Froude number of the jet flow must be small.

For the purpose of this demonstration, the heat transfer from the jet is ignored so that the jet density is assumed constant along the trajectory. Solutions for the governing conservation equations were obtained for $Fr_i = \infty$ (i.e. $\rho_i = \rho_\infty$) and for $Fr_i = 10$; the projections of the resulting trajectories on the x-y and x-z planes are presented in Fig. 54. For the $Fr_i = \infty$ case, the projections on the two planes are equivalent which occurs only when $\beta_i = 45^\circ$ and the trajectory is two dimensional. Allowing ρ_i to be less than ρ_∞ leads to the second set of projections, which shows that decreasing the Froude number increases the penetration of the jet into the cross flow. The fact that the effect is more pronounced on the x-y projection than on the x-z projection is an indication that the triad of unit vectors associated with the natural coordinate system is tracing out a three-dimensional path. In effect these unit vectors are "twisting" out of the plane where the two-dimensional trajectory obtained for the $Fr_i = \infty$ case is located.

Further evidence that these numerical results are consistent can be obtained by examining the dependent variables of the governing

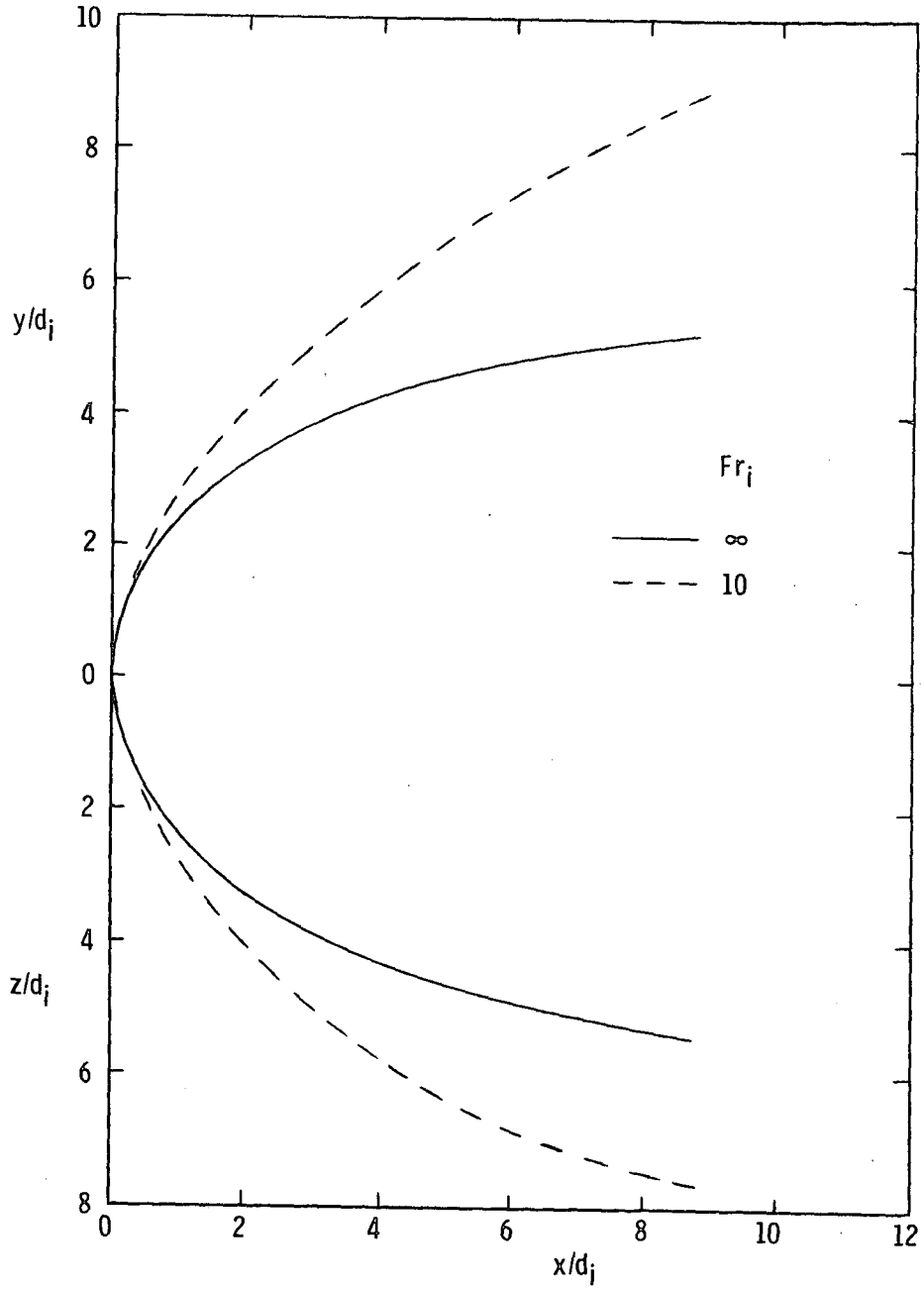

Figure 54.- Effect of Froude number on jet trajectory for $V_i/V_\infty = 4$; $\alpha_i = 90^\circ$, $\beta_i = 45^\circ$.

equations (u and w) and their gradients. This is done in Fig. 55 where the injection conditions are identical to those used in Fig. 54, and the parameters in question are plotted as functions of distance along the trajectory. The solid curves represent the case where buoyancy force is zero ($Fr_i = \infty$) and are typical of the trends that result for injections with $0^\circ \leq \alpha_i \leq 90^\circ$ and $0^\circ \leq \beta_i \leq 90^\circ$. As noted, as increase in s/d_i results in a continual increase in u and decrease in w, u and w approaching 1.0 and 0.0, respectively, for large s/d_i. This, of course, is coincident with the jet velocity vector becoming parallel to the free-stream velocity vector. In conjunction with these trends for u and w, du/ds and dw/ds are, respectively, positive and negative valued.

The dashed curves indicate what happens to the trajectory parameters when a sizeable buoyancy force is considered. The fact that the values of u and w which result when $Fr_i = 10$ are, respectively, smaller and larger than the corresponding values when $Fr_i = \infty$ is indicative of the increase in penetration experienced by the jet when the buoyancy force is added. An interesting aspect of this situation is seen in the variation of w with s/d_i, where w reaches a minimum value at some point on the trajectory and then begins to increase. This is the same as saying that β achieves a maximum value and then begins to decrease. The trend of w with s/d_i is reflected in the dw/ds curve, where dw/ds changes from its usual negative sign to a positive value. This result is important because it signifies that buoyancy force is becoming dominant over the other

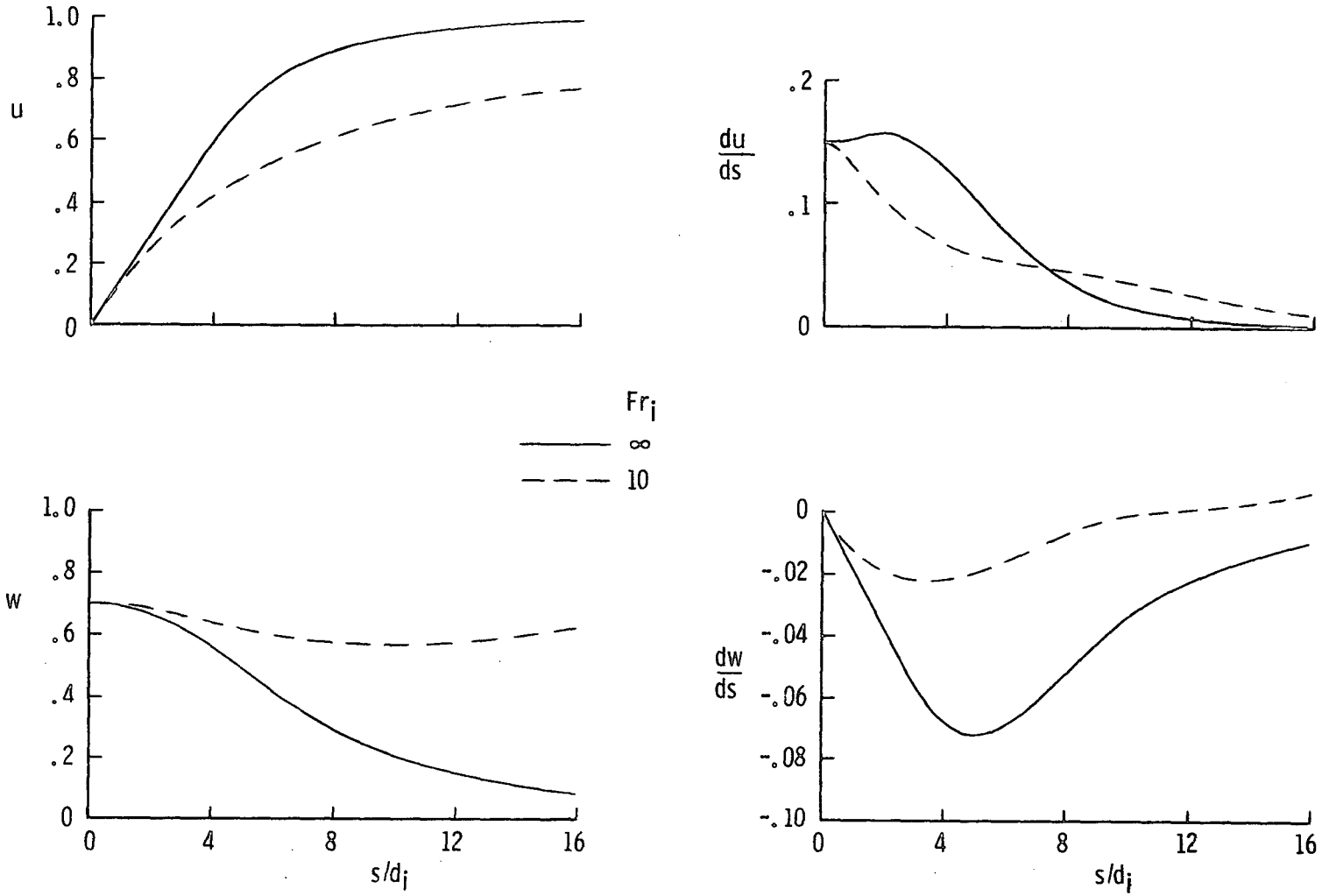

Figure 55.- Effect of Froude number on variation of jet trajectory parameters with distance along trajectory for $V_i/V_\infty = 4$; $\alpha_i = 90^\circ$, $\beta_i = 45^\circ$.

forces acting on the jet flow. It is intuitively obvious that for the situation where buoyancy is the driving force, the jet path will tend toward the vertical so that w will be increasing with increase in s/d_i and dw/ds will be greater than zero. This circumstance can be shown explicitly by letting $V_\infty = u = du/ds = 0$ in the n-momentum equation, Eq. (C-9), presented in Appendix C and by solving the resulting expression for dw/ds.

It is not possible to substantiate the trends discussed here with results from other studies, since no experimental data exists for a jet with a three-dimensional trajectory. In the theoretical development of Hirst[29], it was stated that the governing equations could apply to a jet following a three-dimensional path, however no calculations of a three-dimensional trajectory were presented to support that claim.

XI. CONCLUSIONS

An investigation has been conducted to determine the important parameters that affect the trajectory and flow properties of a heated, submerged effluent discharging into a moving waterway. Efforts to experimentally and theoretically model the effluent as a jet injection process lead to the following concluding remarks:

Experimental results for the jet injected laterally, vertically, and obliquely into a water channel showed that increasing jet injection velocity resulted in further penetration of the jet into the mainstream. For the range of conditions tested, increasing injectant temperature had no discernible effect on the jet trajectory for the lateral injection condition, decreased the amount of jet penetration for the vertical condition, and resulted in a higher trajectory for the oblique injection process with the largest injection velocity. Coincident with these results, addition of heat to the injectant caused a slightly greater rate of spreading of the jet fluid near the injection point; this was particularly obvious for the tests with the lowest injection velocities. The effects of injectant temperature on jet trajectory for the different injection conditions were due to a combination of the following factors: 1) water density is relatively insensitive to temperature change, 2) the jet fluid experienced a rapid heat loss along the trajectory, 3) the injection Froude number was very large implying

that the momentum forces dominated the buoyancy forces, 4) the nature of the jet flow was initially laminar for some of the test conditions, but tended to become turbulent with increase in injectant temperature, and 5) the formation of the counter-rotating vortices in the jet flows was different for the respective conditions.

The theory was developed by using an integral method, which accounted for natural fluid mechanisms such as turbulence, entrainment, buoyancy, and heat transfer, in order to obtain the conservation equations governing the jet flow. Solving these equations simultaneously yielded predictions of jet trajectory and area growth that agreed well with experimental results, and thus demonstrated the usefulness of the theory for estimating the location and size of the thermal plume with respect to the discharge point.

Unlike previous studies which assumed a specific cross-sectional area growth for the jet, the present investigation obtained the jet cross-sectional area in the process of solving the governing equations. Because of this, the present theory provided better estimates for the jet trajectory and allowed a prediction for various jet flow properties, such as velocity and momentum, to be obtained. Closer agreement with experimental jet flow properties could be achieved by improving the analytical model of the entrainment process.

Realistic estimates of temperature in the jet fluid were obtained by accounting for heat losses in the jet flow due to forced convection and to entrainment of free-stream fluid into the jet. Forced convection was seen to be the dominant heat-transfer mechanism during the early stages of the jet injection process, while the effects of entrainment became dominant as the jet penetrated further into the freestream flow.

The versatility of the theory was demonstrated by observing the effects of a jet injected into free-stream flows with either a nonuniform velocity field or a nonuniform temperature field. Theoretical results were also shown to illustrate a truly three-dimensional jet trajectory which was calculated by considering the injection Froude number to be small.

XII. REFERENCES

1. "Heat can Hurt - Better Water For America", Prepared by the Office of Public Information, FWQA, CWA-14, May 1970, GPO 889-539.

2. Aronson, R. B.: "Thermal Pollution and the Power Crisis", Machine Design, June 25, 1970, pp. 30.

3. Woodson, R. D.: "Cooling Towers", Scientific American, May 1971, pp. 70.

4. "Bibliography on Thermal Pollution", Committee on Thermal Pollution, Journal of Sanitary Engineering Division, Proc. of Amer. Society of Civil Engineers, June 1967, pp. 85-113.

5. Kennedy, V. S., and Mihursky, J. A.: "Bibliography of the Effects of Temperature in the Aquatic Environment", Submitted to Hearings on Thermal Pollution - 1968 before the Subcommittee on Air and Water Pollution, U. S. Senate, Feb. 1968, Part 1, pp. 471-568, GPO.

6. "Thermal Pollution Notes", Collection of papers from the Second Thermal Pollution Seminar, sponsored by the Institute of Environmental Sciences, Oct. 20-22, 1970, Chicago, Illinois.

7. Edinger, J. E., and Geyer, J. C., "Heat Exchange in the Environment," Dept. of Sanitary Engineering and Water Resources, The Johns Hopkins University, Baltimore, Md., June 1965.

8. Mahgary, Y. S. El, "Thermal Diffusion of the Warm Water of Power Plants into a Sea Basin," Journal of Environmental Sciences, Nov./Dec. 1971, pp. 20-23.

9. Tichenor, B. A., and Cawley, W. A.: "Research Needs for Thermal-Pollution Control", Proceedings of the National Symposium on Thermal Pollution, Nashville, Tennessee, Aug. 14-16, 1968, (Engineering Aspects of Thermal Pollution, edited by F. L. Parker and P. A. Krenkel, Vanderbilt University Press, 1969, pp. 329-338.)

10. Parker, F. L. and Krenkel, P. A.: "Physical and Engineering Aspects of Thermal Pollution" CRC Critical Reviews in Environmental Control, Vol. I, Issue I, Feb. 1970, pp. 101-192.

11. Margason, R. J.: "Jet-Wake Characteristics and Their Induced Aerodynamic Effects on V/STOL Aircraft in Transition Flight" NASA SP-218, Sept. 1969, pp. 1-18.

12. Gordier, R. L.: "Studies on Fluid Jets Discharging Normally into Moving Liquid," Univ. of Minn., St. Anthony Falls Hydraulic Lab., Tech. Paper No. 28, Series B, 1959.

13. Margason, R. J., "The Path of a Jet Directed at Large Angles to a Subsonic Free Stream," NASA TN D-4919, Nov. 1968.

14. Platten, J. L. and Keffer, J. F.: "Deflected Turbulent Jet Flows" ASME Paper No. 71-APM-SS (Submitted to J. of Applied Mechanics), 1972.

15. Jordinson, R., "Flow in a Jet Directed Normal to the Wind," R. and M. No. 3074, British A.R.C., 1958.

16. Keffer, J. F., and Baines, W. D., "The Round Turbulent Jet in a Cross-Wind," Journal of Fluid Mechanics, Vol. 15, Part 4, 1963, pp. 481-496.

17. Ramsey, J. W., "The Interaction of a Heated Air Jet with a Deflecting Flow," Ph. D. Thesis, University of Minnesota, June 1969.

18. Kamotani, Y., and Greber, I., "Experiments on a Turbulent Jet in a Cross Flow," NASA CR-72893, July 1971. (See also AIAA Paper No. 72-149 presented at 10th Aerospace Sciences Meeting, San Diego, CA, Jan. 17-19, '72).

19. Abramovich, G. N., The Theory of Turbulent Jets, The M.I.T. Press, Cambridge, Mass., 1963, pp. 541-553.

20. Keffer, J. F.: "The Physical Nature of the Subsonic Jet in a Cross-Stream" NASA SP-218, pp. 22.

21. Morton, B. R.: "On a Momentum-Mass Flux Diagram for Turbulent Jets, Plumes, and Wakes" J. of Fluid Mechanics, Vol. 10, Part 1, Feb. 1961, pp. 101-112.

22. Ricou, F. P., and Spalding, D. B.: "Measurements of Entrainment by Axisymmetrical Turbulent Jets" J. of Fluid Mechanics, Vol. 11, 1961, pp. 21-32.

23. Schetz, J. A., and Billig, F. S., "Penetration of Gaseous Jets Injected Into A Supersonic Stream" Journal of Spacecraft and Rockets, Vol. 3, No. 11, November 1966, pp. 1658-1665.

24. Reilly, R. S.: "Investigation of the Deformation and Penetration of a Turbulent, Subsonic Jet Issuing Transversely into a Uniform Subsonic Main Stream" Ph. D. Thesis, Univ. of Maryland, Aug. 1968.

25. Campbell, J. F., and Schetz, J. A., "Penetration and Mixing of Heated Jets in a Waterway with Application to the Thermal Pollution Problem," Presented at AIAA Urban Technology Conference, New York City, May 24-26 1971, AIAA Paper No. 71-524.

26. Wooler, P. T., Burghart, G. H., and Gallagher, J. T., "Pressure Distribution on a Rectangular Wing with a Jet Exhausting Normally into an Airstream," Journal of Aircraft, Vol. 4, No. 6, Nov. - Dec. 1967, pp. 537-543.

27. Hoult, D. P., Fay, J. A., and Forney, L. J.: "A Theory of Plume Rise Compared with Field Observations" Journal of Air Pollution Control Associates, Vol. 19, No. 8, pp. 585-590, Aug. 1969.

28. Hoult, D. P. and Weil, J. C.: "Turbulent Plume in a Laminar Cross Flow", Fluid Mechanics Laboratory Publication No. 70-8, Dept. of Mechanical Eng., M.I.T., Oct. 1970.

29. Hirst, E. A.: "Analysis of Round, Turbulent, Buoyant Jets Discharged to Flowing Stratified Ambients," Oak Ridge National Laboratory, ORNL-4685, June 1971. (Available from National Technical Information Service, U. S. Dept. of Commerce, Springfield, Virginia).

30. Campbell, J. F., and Schetz, J. A.: "Flow Properties of Submerged Heated Effluents in a Waterway," Presented at AIAA 10th Aerospace Sciences Meeting, San Diego, Calif., Jan. 17-19, 1972, AIAA Paper No. 72-79.

31. Platten, J. L.; and Keffer, J. F.: "Entrainment in Deflected Axisymmetric Jets at Various Angles to the Stream", Univ. of Toronto, Mechanical Engineering Dept., UTME-TP-6808, 1968.

32. Schlichting, H., Boundary-Layer Theory, 6th Edition, McGraw-Hill Book Company, New York, 1968, pp. 681-707.

33. Eckert, E. R. G., and Drake, R. M., Jr., Heat and Mass Transfer, 2nd Edition, McGraw-Hill Book Company, New York,1959, pp. 139, 239-243.

34. Hildebrand, F. B.: Advanced Calculus For Applications, Prentice-Hall, Inc., Englewood Cliffs, New Jersey, 1962, pp. 271-275.

35. Applied Engineering Science, Chemical Rubber Company Press, 1st Edition, 1970, Table 1-35, pp. 66.

36. Theory and Problems of Fluid Dynamics, Schaum's Outline Series, McGraw-Hill Book Company, 1967, Table A.1, pp. 245.

XIII. APPENDIX A

Tabulated Test Conditions

The test conditions associated with the lateral, vertical, and oblique injection experiments are presented in Tables III, IV, and V, respectively. These test logs contain the values of the parameters locating the jet orifice, along with the measured mass flow rates and temperatures of the free-stream and injected fluids. Each test is assigned a run number to aid in identifying its conditions with the photographs presented in the text. The densities ρ_i and ρ_∞ were obtained from the measured values of T_i and T_∞, respectively, by linearly interpolating in a temperature-density table (Ref. 35).

An average free-stream velocity at the injection station (V_∞) was calculated using

$$\dot{m}_\infty = \rho_\infty A_\infty V_\infty \qquad \text{(A-1)}$$

where A_∞ is the cross-sectional area of the main flow at the injection station. It is noted that V_∞ has physical meaning only if it is considered as the integrated local free-stream velocity over A_∞, see Eq. (A-3). The average injection velocity was obtained using,

$$\dot{m}_i = \rho_i A_i V_i \qquad \text{(A-2)}$$

where $\dot{m}_i$ is the value listed in the test logs and was obtained from the flow meter calibration in Fig. 17.

TABLE III. TEST CONDITIONS FOR LATERAL INJECTION PROCESS; $\alpha_i = \beta_i = 90^\circ$, $d_i = 0.0625$ in.

RUN NO.	a inches	L inches	$\dot{m}_i$ lb_f/min	ΔT_i $^\circ F$	$\dot{m}_\infty$ lb_f/min	T_∞ $^\circ F$	ρ_∞ lb_f/ft^3	V_∞ ft/sec	ρ_i lb_f/ft^3	V_i ft/sec	ρ_i/ρ_∞	T_i/T_∞	V_i/V_∞	VR	$\nu_i \times 10^5$ ft^2/sec	Re_{d_i}	Fr_i
7	1.25	27.00	1.31	-2.2	242.4	78.0	62.246	0.547	62.264	16.462	1.00029	0.9718	30.095	30.099	0.98	8748	$-\infty$
8			0.79	-2.2	242.4	78.0	62.246	0.547	62.264	9.928	1.00029	0.9718	18.150	18.153	0.98	5276	$-\infty$
9			0.23	-2.0	242.4	77.7	62.248	0.547	62.264	2.890	1.00026	0.9743	5.283	5.284	0.98	1536	-387,629
13			0.23	-1.0	242.4	77.0	62.254	0.547	62.262	2.890	1.00013	0.9870	5.283	5.284	0.97	1552	-775,232
14	1.90	26.10	1.31	-0.6	255.6	75.7	62.265	0.577	62.269	16.461	1.00006	0.9921	28.529	28.530	0.98	8748	$-\infty$
15			0.79	-0.4	255.6	75.7	62.265	0.577	62.268	9.928	1.00005	0.9947	17.206	17.207	0.98	5276	$-\infty$
16			0.23	-0.4	255.6	75.7	62.265	0.577	62.268	2.890	1.00005	0.9947	5.009	5.009	0.98	1536	$-\infty$
31	1.25	27.00	0.79	64.5	247.2	72.0	62.307	0.558	61.443	10.061	0.98613	1.8958	18.030	17.905	0.53	9886	85,851
32			0.23	54.2	247.2	72.0	62.307	0.558	61.612	2.921	0.98885	1.7528	5.235	5.205	0.58	2623	9,021
33*			0.23	62.0	247.2	71.7	62.296	0.558	61.485	2.927	0.98698	1.8647	5.246	5.211	0.54	2823	7,746
34*			0.23	63.0	247.2	71.7	62.296	0.558	61.470	2.927	0.98674	1.8787	5.246	5.211	0.538	2833	7,604
36*			0.23	64.3	247.2	71.7	62.296	0.558	61.450	2.928	0.98642	1.8968	5.247	5.212	0.53	2877	7,427

*Jet temperatures measured during Runs 33, 34, and 36 using thermocouple probe (see Fig. 11)

TABLE IV. TEST CONDITIONS FOR VERTICAL INJECTION PROCESS; $\alpha_i = 90^\circ$, $\beta_i = 0^\circ$, $d_i = 0.0595$ in.

38	0	26.90	0.21	-3.2	240.0	75.3	62.268	0.331	62.293	2.911	1.00040	0.9575	8.795	8.796	1.02	1415	-251,818
39			0.41	-3.2	240.0	75.3	62.268	0.331	62.293	5.684	1.00040	0.9575	17.172	17.176	1.02	2763	$-\infty$
40			0.69	-3.2	240.0	75.3	62.268	0.331	62.293	9.565	1.00040	0.9575	28.897	28.903	1.02	4649	$-\infty$
45			0.21	25.7	240.0	68.0	62.324	0.330	62.069	2.922	0.99591	1.3779	8.855	8.836	0.80	1811	24,786
46			0.69	25.0	240.0	69.0	62.317	0.330	62.066	9.600	0.99597	1.3623	29.091	29.032	0.795	5987	271,785
63			0.69	43.7	222.0	64.0	62.352	0.305	61.908	9.625	0.99283	1.6828	31.557	31.445	0.69	6916	152,950
64			0.41	44.0	222.0	64.0	62.352	0.305	61.904	5.719	0.99276	1.6875	18.751	18.683	0.69	4109	53,899
65			0.21	46.0	222.0	64.5	62.349	0.305	61.873	2.931	0.99237	1.7132	9.610	9.573	0.67	2169	13,318

TABLE V. TEST CONDITIONS FOR OBLIQUE INJECTION PROCESS; $d_i = 0.0625$ in.

53	1.500	27.00	0.69	9.3	237.0	72.0	62.307	0.326	62.228	8.676	0.99873	1.1292	26.613	26.597	0.91	4965	706,970
54			0.41	3.6	237.0	72.0	62.307	0.326	62.265	5.152	0.99933	1.0500	15.804	15.798	0.98	2738	469,299
55	(α_i=90°, β_i=50°)		0.21	5.4	237.0	70.5	62.306	0.326	62.263	2.639	0.99931	1.0766	8.095	8.092	0.97	1417	120,266
56			0.98	5.4	237.0	70.5	62.306	0.326	62.263	12.313	0.99931	1.0766	37.770	37.757	0.97	6611	2,618,138
58			0.69	47.8	237.0	73.0	62.286	0.326	61.715	8.748	0.99083	1.6548	26.834	26.711	0.61	7469	98,645
59			0.41	44.0	237.0	73.0	62.286	0.326	61.775	5.193	0.99180	1.6027	15.929	15.864	0.63	4293	38,880
60			0.21	46.4	237.0	73.0	62.286	0.326	61.739	2.662	0.99122	1.6356	8.166	8.130	0.62	2236	9,549
61			0.98	63.0	237.0	73.0	62.286	0.326	61.450	12.476	0.98658	1.8630	38.270	38.012	0.53	12859	1[illegible],449
67	1.950	27.50	0.21	66.7	237.0	64.0	62.352	0.305	61.530	2.671	0.98682	2.0422	8.757	8.699	0.56	2484	6,869
	(α_i=140°, β_i=90°)																
69	1.950	26.50	0.21	17.1	237.0	65.0	62.345	0.306	62.205	2.642	0.99775	1.2631	8.634	8.624	0.90	1529	86,088
71	(α_i=40°, β_i=90°)		0.69	43.0	237.0	64.0	62.352	0.305	61.916	8.720	0.99301	1.6719	28.590	28.490	0.695	6534	178,781

Also shown in the test logs are ratios of temperature, density, and velocity between the injectant parameter and its counterpart in the free-stream flow. The momentum ratio is an important parameter for classifying jet flows and has been used by several researchers[13,16,18]. The square root of the momentum ratio, referred to here as the effective velocity ratio (VR), is seen to be essentially the same as the velocity ratio, V_i/V_∞. This is due to the fact that water density is a weak function of temperature.

The other properties of the jet flow at the injection point which are listed in the test logs and which were deduced from previous information in the tables are viscosity, Reynolds number, and Froude number. The viscosity was determined with the values of T_i from a viscosity-temperature plot (see Table A.1 in Ref. 36) and as can be seen is very temperature sensitive. This dependency on temperature is reflected in the values of Re_{d_i} and Fr_i, which are very susceptible to changes in injectant temperature.

Nonuniform Free-stream Velocity Field

One of the problems inherent with injection tests performed in small scale water channels is the nonuniformity of the free-stream velocity field. It is advantageous to investigate the extent of this nonuniformity because of its influence on injection characteristics. No measurements were made of local free-stream velocities during the experimental tests; however, the following exercise was performed to shed some analytical light on the subject.

A boundary layer is assumed to form on the channel surfaces as illustrated in Fig. 56(a), where $V_{\infty,\ell}$ is the local free-stream velocity. Estimated thicknesses of this boundary layer were previously presented in the Tests section of Chapter IX for the flow conditions of the current study. The local free-stream velocity can be used in the following definition to acquire the average velocity in the channel:

$$V_\infty = \frac{\iint V_{\infty,\ell}\, d\Gamma}{\iint d\Gamma} = \frac{\int_0^{W_c}\int_0^{H_c} V_{\infty,\ell}\, dy\, dz}{\int_0^{W_c}\int_0^{H_c} dy\, dz} \qquad \text{(A-3)}$$

where $\iint d\Gamma$ is the cross-sectional area of the water channel flow (A_∞). The idea is to postulate a velocity variation in the boundary layer, use the value of V_∞ yielded by Eq. (A-1), and work backwards through Eq. (A-3) to obtain an estimate of the maximum velocity in the channel flow.

Assuming that the local velocity can be divided into regions as shown in Fig. 56(b), and neglecting any shear between the moving water surface and the atmosphere, the velocity in the boundary layer regions can be approximated by the Karman-Pohlhausen method. This leads to a functional form for the local velocity in regions 1 and 2, where $V_{\infty,\ell} = V_{\infty,\ell}(z)$. Thus,

$$\frac{V_{\infty,\ell}}{V_{\infty,e}} = \frac{3}{2}\left(\frac{z}{\delta}\right) - \frac{1}{2}\left(\frac{z}{\delta}\right)^3 \qquad \text{(A-4)}$$

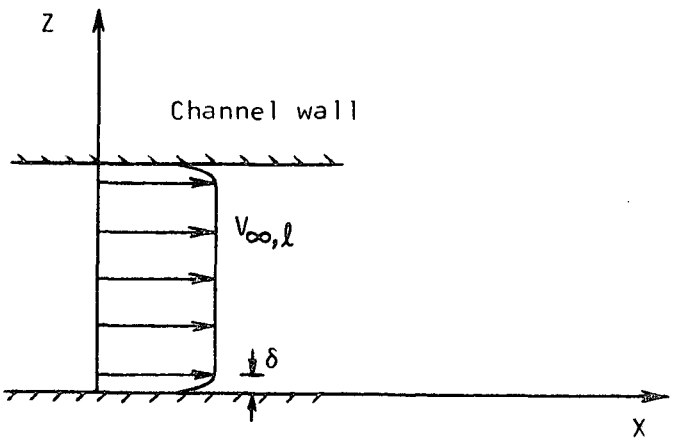

(a) Postulated local free-stream velocity

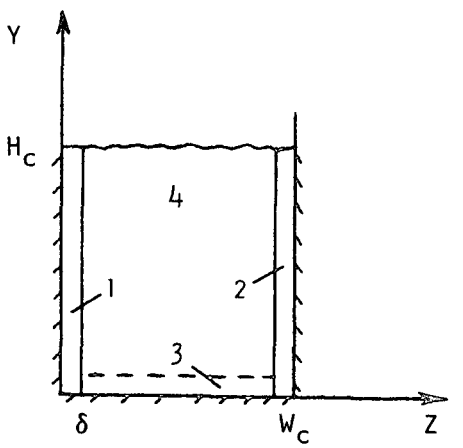

(b) Regions of boundary-layer flow

Figure 56.- Schematic diagram of free-stream velocity field assumed to exist in water channel.

where $V_{\infty,e}$ is the velocity at the boundary layer edge and is assumed to be constant through region 4. The resulting expression for region 3 is

$$\frac{V_{\infty,\ell}}{V_{\infty,e}} = \frac{3}{2}\left(\frac{y}{\delta}\right) - \frac{1}{2}\left(\frac{y}{\delta}\right)^3 \qquad \text{(A-5)}$$

The local velocity functions shown above are integrated in Eq. (A-3) over the respective regions where they are assumed to be acting. Taking the proper values for H_c, W_c, and δ associated with the vertical and oblique injection tests we find that $V_{\infty,e} = 0.365$ ft/sec compared to the average velocity value of $V_\infty = 0.330$ ft/sec. This result suggests that the maximum velocity in the channel is about 10% higher than the average velocity and occupies approximately 75% of the flow area.

The value of $V_{\infty,e}$ for the lateral injection tests would be proportionately closer to the value of V_∞ than was obtained above for the vertical and oblique injection tests. This is because the estimated boundary layer thickness for the lateral injection tests is 2/3 of the value used in the calculations above, hence $V_{\infty,e}$ would occupy a greater flow area and its value would correspondingly be lower. An example of the theoretical effects obtained when the jet is discharged into a nonuniform free-stream velocity field of this type is presented in Chapter X.

XIV. APPENDIX B

Space Curve Information

This appendix provides additional information about the natural coordinate system used in the analytical study, and presents the expressions necessary to transform the momentum equations in the text to the form used in the numerical solution.

Space Curves

As was mentioned in Chapter VIII, the natural coordinate system consists of a moving triad of unit vectors $\vec{e}_s$, $\vec{e}_n$, and $\vec{e}_t$. This is illustrated in Fig. 57(a) where $\vec{r}$ is the position vector from the origin to a point on the curve and is given by,

$$\vec{r} = x\,\vec{e}_x + y\,\vec{e}_y + z\,\vec{e}_z \tag{B-1}$$

The derivative of a position vector is shown by Hildebrand[34] to be a unit vector tangent to the curve and pointing in the direction of increasing arc length:

$$\vec{e}_s = \frac{d\vec{r}}{ds} = \frac{dx}{ds}\vec{e}_x + \frac{dy}{ds}\vec{e}_y + \frac{dz}{ds}\vec{e}_z \tag{B-2}$$

where it is noted that $d\vec{r}/dt$ is the velocity vector associated with a point moving with speed ds/dt along the curve. Thus,

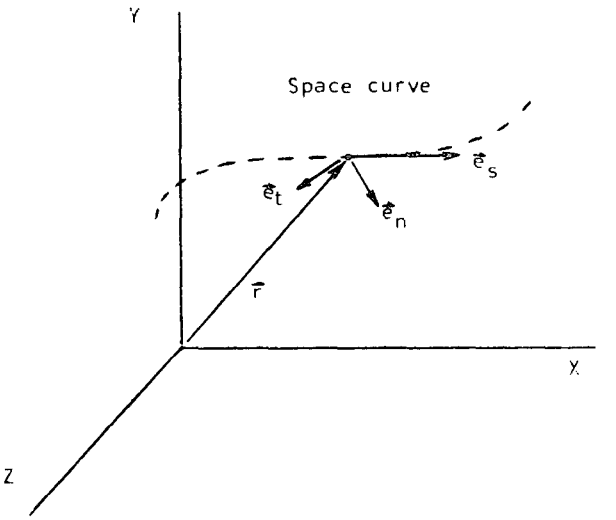

(a) Natural coordinate system

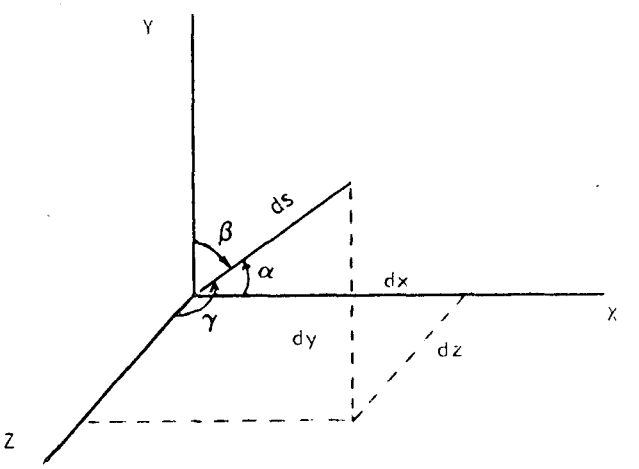

(b) Direction cosines of $\vec{e}_s$

Figure 57.- Illustration of the natural coordinate system and the direction cosines of the unit vector $\vec{e}_s$.

$$\vec{V} = \frac{ds}{dt}\frac{\vec{dr}}{ds} = V\,\vec{e}_s \tag{B-3}$$

Since $\vec{e}_s$ is a unit vector, it follows that

$$\left(\frac{dx}{ds}\right)^2 + \left(\frac{dy}{ds}\right)^2 + \left(\frac{dz}{ds}\right)^2 = 1 \tag{B-4}$$

The derivative of $\vec{e}_s$ with respect to s has a direction perpendicular to the curve and is written as,

$$\frac{\vec{de}_s}{ds} = \frac{d^2x}{ds^2}\vec{e}_x + \frac{d^2y}{ds^2}\vec{e}_y + \frac{d^2z}{ds^2}\vec{e}_z \tag{B-5}$$

where the length of this vector is the curvature of the curve. Defining the radius of curvature (R) as the reciprocal of the curvature, and $\vec{e}_n$ as the unit vector in a direction normal to $\vec{e}_s$, we have

$$\frac{\vec{de}_s}{ds} = \frac{1}{R}\vec{e}_n \tag{B-6}$$

so that

$$\frac{1}{R} = \left[\left(\frac{d^2x}{ds^2}\right)^2 + \left(\frac{d^2y}{ds^2}\right)^2 + \left(\frac{d^2z}{ds^2}\right)^2\right]^{1/2} \tag{B-7}$$

A moving, rotating triad of mutually orthogonal unit vectors is completely described by the addition of the third unit vector, $\vec{e}_t$, which by definition is,

$$\vec{e}_t = \vec{e}_s \times \vec{e}_n \tag{B-8}$$

It is noted that for a plane curve, $\vec{e}_s$ and $\vec{e}_n$ lie in the plane of the curve, while $\vec{e}_t$ is a constant unit vector perpendicular to that plane. The trajectory resulting from the vertical injection process is an example of this situation. Differentiating Eq. (B-8) leads to,

$$\frac{d\vec{e}_t}{ds} = -\tau_o \vec{e}_n \tag{B-9}$$

where the scalar τ_o is the torsion of the curve, the negative sign implying that τ_o is positive when the vector triad rotates in a right-handed sense about $\vec{e}_s$ as it progresses along the curve.

To find $d\vec{e}_n/ds$ we write $\vec{e}_n = \vec{e}_t \times \vec{e}_s$ and differentiate to get,

$$\frac{d\vec{e}_n}{ds} = \tau_o \vec{e}_t - \frac{1}{R}\vec{e}_s \tag{B-10}$$

Equations (B-6), (B-9), and (B-10) are known as the Frenet-Serret formulas. Taking the dot product of $\vec{e}_t$ with $d\vec{e}_n/ds$ leads to an expression for torsion which can be written in determinant form as,

$$\tau_o = R^2 \begin{vmatrix} dx/ds & dy/ds & dz/ds \\ d^2x/ds^2 & d^2y/ds^2 & d^2z/ds^2 \\ d^3x/ds^3 & d^3y/ds^3 & d^3z/ds^3 \end{vmatrix} \tag{B-11}$$

We are now in a position where we can find the dot products that are required in the momentum equations in Chapter VIII. For example, $(\vec{e}_x \cdot \vec{e}_n)$ and $(\vec{e}_y \cdot \vec{e}_n)$ are needed in the expression for n-momentum, Eq. (26). Using equations (B-5) and (B-6) yields,

$$\vec{e}_n = R \frac{d^2\vec{r}}{ds^2} \tag{B-12}$$

so that we get,

$$(\vec{e}_x \cdot \vec{e}_n) = R \frac{d^2x}{ds^2} \tag{B-13}$$

and

$$(\vec{e}_y \cdot \vec{e}_n) = R \frac{d^2y}{ds^2} \tag{B-14}$$

A similar procedure is used to get the dot products needed for the s-momentum expression:

$$(\vec{e}_x \cdot \vec{e}_s) = \frac{dx}{ds} \tag{B-15}$$

and

$$(\vec{e}_y \cdot \vec{e}_s) = \frac{dy}{ds} \tag{B-16}$$

The process for obtaining the dot products for the t-momentum expression, Eq. (51), is more envolved because of the use of $\vec{e}_t$. The equation for $\vec{e}_t$ is found from Eq. (B-10) to be,

$$\vec{e}_t = \frac{1}{\tau_o}\frac{d}{ds}\left(R\frac{d^2\vec{r}}{ds^2}\right) + \frac{1}{R\tau_o}\frac{d\vec{r}}{ds} \qquad \text{(B-17)}$$

Dotting $\vec{e}_x$ and $\vec{e}_y$, respectively, with this expression and using the distributive law for dot products leads to,

$$(\vec{e}_x \cdot \vec{e}_t) = \frac{1}{\tau_o}\frac{dR}{ds}\frac{d^2x}{ds^2} + \frac{R}{\tau_o}\frac{d^3x}{ds^3} + \frac{1}{R\tau_o}\frac{dx}{ds} \qquad \text{(B-18)}$$

and

$$(\vec{e}_y \cdot \vec{e}_t) = \frac{1}{\tau_o}\frac{dR}{ds}\frac{d^2y}{ds^2} + \frac{R}{\tau_o}\frac{d^3y}{ds^3} + \frac{1}{R\tau_o}\frac{dy}{ds} \qquad \text{(B-19)}$$

Direction Cosines

It was mentioned in Chapter VIII that the procedure for solving the governing equations (5), (27), (43), (52) simultaneously was simplified by using the direction cosines of the unit vector $\vec{e}_s$ as the dependent variables. The angles $\vec{e}_s$ makes with the x,y, and z axes are shown in Fig. 57(b) and are defined as,

$$\cos(\alpha) = \frac{dx}{ds} \qquad \cos(\beta) = \frac{dy}{ds} \qquad \cos(\gamma) = \frac{dz}{ds} \qquad \text{(B-20)}$$

Eq. (B-4) represents the auxilliary equation for these direction cosines and is used to express the third direction cosine (dz/ds) in terms of the other two. Define

$$u = \frac{dx}{ds} \quad \text{and} \quad w = \frac{dy}{ds} \tag{B-21}$$

so that Eq. (B-4) becomes,

$$\frac{dz}{ds} = (1 - u^2 - w^2)^{1/2} = \eta^{1/2} \tag{B-22}$$

The derivatives of this expression are found to be,

$$\frac{d^2z}{ds^2} = \frac{- u \frac{du}{ds} - w \frac{dw}{ds}}{\eta^{1/2}} = \frac{\Lambda}{\eta^{1/2}} \tag{B-23}$$

and

$$\frac{d^3z}{ds^3} = \frac{\eta \left[- u \frac{d^2u}{ds^2} - \left(\frac{du}{ds}\right)^2 - w \frac{d^2w}{ds^2} - \left(\frac{dw}{ds}\right)^2 \right] - \Lambda^2}{\eta^{3/2}} \tag{B-24}$$

Expressions for R, dR/ds, τ_o

At this point it is desirable to obtain the expressions for R, dR/ds, and τ_o in terms of the direction cosines u and w. Equations (B-21) and (B-23) are substituted into Eq. (B-7) to get the expression for R:

$$\frac{1}{R} = \left[\left(\frac{du}{ds}\right)^2 + \left(\frac{dw}{ds}\right)^2 + \frac{\Lambda^2}{\eta}\right]^{1/2} \qquad \text{(B-25)}$$

The relation for dR/ds is obtained by differentiating R, Eq. (B-7), and substituting the necessary auxilliary equations from Eq. (B-21) to (B-24):

$$-\frac{1}{R^3}\frac{dR}{ds} = \frac{du}{ds}\frac{d^2u}{ds^2} + \frac{dw}{ds}\frac{d^2w}{ds^2} + \frac{\Lambda}{\eta^{1/2}}\left\{-\frac{1}{\eta^{1/2}}\left[u\frac{d^2u}{ds^2} + \left(\frac{du}{ds}\right)^2 + w\frac{d^2w}{ds^2} + \left(\frac{dw}{ds}\right)^2\right] - \frac{\Lambda^2}{\eta^{3/2}}\right\} \qquad \text{(B-26)}$$

The torsion of the curve is obtained after some manipulation by expanding the determinant in Eq. (B-11), and by substituting the auxilliary equations:

$$\frac{\tau_o}{R^2} = -\left(u\frac{dw}{ds} - w\frac{du}{ds}\right)\left\{\frac{1}{\eta^{1/2}}\left[u\frac{d^2u}{ds^2} + \left(\frac{du}{ds}\right)^2 + w\frac{d^2w}{ds^2} + \left(\frac{dw}{ds}\right)^2\right] + \frac{\Lambda^2}{\eta^{3/2}}\right\}$$
$$+\left(-\frac{\Lambda}{\eta^{1/2}}u + \eta^{1/2}\frac{du}{ds}\right)\frac{d^2w}{ds^2} + \left(\frac{\Lambda}{\eta^{1/2}}w - \eta^{1/2}\frac{dw}{ds}\right)\frac{d^2u}{ds^2} \qquad \text{(B-27)}$$

Thus, equations (B-25) to (B-27) represent R, dR/ds, and τ_o as functions of u and w and their derivatives for the general case of a three-dimensional curve. It is interesting to note the forms these equations take when the trajectory is two dimensional, such as for a vertical injection process ($\gamma = 90^o$). For this situation, the auxilliary equation (B-22) becomes,

$$u^2 + w^2 = 1 \quad (\text{i.e. } n = 0) \tag{B-28}$$

so that

$$\Lambda = u \frac{du}{ds} + w \frac{dw}{ds} = 0 \tag{B-29}$$

Using these relations in Eq. (B-25) leads to

$$\frac{1}{R} = \frac{1}{w} \frac{du}{ds} \tag{B-30}$$

Likewise,

$$-\frac{1}{R^3} \frac{dR}{ds} = \frac{du}{ds} \frac{d^2u}{ds^2} + \frac{dw}{ds} \frac{d^2w}{ds^2} \tag{B-31}$$

and $\tau_o = 0$. Torsion would be expected to equal zero from Eq. (B-9), since the trajectory is a plane curve which implies that $\vec{e}_t$ is a constant vector (parallel to the z-axis).

XV. APPENDIX C

Nondimensional Conservation Equations

The purpose of this appendix is to nondimensionalize the governing conservation equations and to make several observations concerning their numerical solution. In addition, special forms of the governing equations are examined and the t-momentum equation is shown to be an identity for the vertical injection situation.

s-Momentum

The direction cosine expressions from Appendix B are substituted into Eq. (43) and the resulting expression is divided by $\frac{(\rho AV^2)_i}{d_i}$ to get the nondimensionalized s-momentum equation:

$$\frac{1}{(\rho AV^2)_i}\frac{d(\rho AV^2)}{d\bar{s}} = \frac{1}{2}\left(\frac{A}{A_i}\right) d_i \frac{g(\rho_\infty - \rho)w}{q_i} + \frac{1}{2}\left(\frac{A}{A_i}\right)\left(\frac{q_\infty}{q_i}\right)\left[\bar{R}\frac{d\bar{R}}{d\bar{s}}\left(\frac{du}{d\bar{s}}\right)^2 + \bar{R}^2\frac{du}{d\bar{s}}\frac{d^2u}{d\bar{s}^2}\right] + J\left(\frac{V_\infty}{V_i}u\right) - 4\,H\,K_1\left(\frac{\rho}{\rho_i}\right)\frac{(V - V_\infty u)^2}{V_i^2} \qquad (C\text{-}1)$$

where the barred symbols indicate division by d_i, and $H = h/d_i$. The expression,

$$E = J\frac{(\rho AV)_i}{d_i} \qquad (C\text{-}2)$$

was also used in the process of obtaining Eq. (C-1).

As was mentioned in Solution Procedure in Chapter VIII, Eq. (C-1) is solved at point "j+1" for the jet momentum which is estimated by

using a backward finite difference to approximate the rate of change of (ρAV^2) with $\bar{s}$. This gives

$$\left.\frac{d(\rho AV^2)}{d\bar{s}}\right|_{j+1} = \frac{(\rho AV^2)_{j+1} - (\rho AV^2)_j}{\Delta\bar{s}} \qquad (C\text{-}3)$$

which can be substituted into Eq. (C-1). The momentum $(\rho AV^2)_{j+1}/(\rho AV^2)_i$ is calculated by using values for the various parameters in Eq. (C-1) evaluated at (j) as a first estimate, and then using (j+1) values after the first iteration. The jet momentum is then used in conjunction with $(\rho AV)_{j+1}$ to provide values for V_{j+1}, and hence A_{j+1}.

At this point in the numerical solution the heat loss from the jet control volume is accounted for. It should be recalled [see Eq. (53)] that the mass of fluid in the control volume must be specified before and after entrainment takes place in order to calculate the effect of entrainment on jet temperature. The total mass in the control volume after entrainment is given by,

$$m_{j+1} = m_j + m_e \qquad (C\text{-}4)$$

where the entrained mass (m_e) is found to be,

$$m_e = \frac{(\Delta s)^2 E}{V_a} \qquad (C\text{-}5)$$

V_a is the velocity of entrainment and is taken to be an average velocity in the control volume; Eq. (6) is used in conjunction with

the E^* function presented in Fig. 3 to specify E.

n-Momentum

The expressions for the direction cosines (Appendix B) are substituted into Eq. (27) and the resulting equation is divided by ρAV^2. The ratio of mass flow in the jet to the initial jet mass flow is written as,

$$K = \frac{\rho AV}{(\rho AV)_i} \tag{C-6}$$

and is used to get the nondimensional n-momentum equation:

$$\frac{1}{\bar{R}} = G_1 \bar{R} \frac{dw}{d\bar{s}} + G_2 \bar{R}^2 \left(\frac{du}{d\bar{s}}\right)^2 + G_3 \bar{R} \frac{du}{d\bar{s}} \tag{C-7}$$

where $\bar{R} = R/d_i$ and

$$G_1 = \frac{d_i}{2} \left(\frac{\rho}{\rho_i}\right)\left(\frac{A}{A_i}\right)^2 \frac{g(\rho_\infty - \rho)}{K^2 q_i}$$

$$G_2 = \frac{2H}{\pi K^2} C_{D_n} \left(\frac{q_\infty}{q_i}\right) \left(\frac{\rho}{\rho_i}\right)\left(\frac{A}{A_i}\right)$$

$$G_3 = \frac{J}{K^2} \left(\frac{V_\infty}{V_i}\right) \left(\frac{\rho}{\rho_i}\right)\left(\frac{A}{A_i}\right)$$

In order to put Eq. (C-7) into the form used in the numerical solution, the expression for R must be considered [Eq. (B-25)]. Examining the vertical injection case results in a cubic equation

in du/ds after equations (B-25), (B-28), (B-29), and(B-30) are substituted into Eq. (C-7). It is noted that two roots of the cubic equation are zero if the buoyancy term is neglected. This type of trivial solution can be avoided by dividing du/ds out of Eq. (B-25) to get,

$$\frac{1}{\bar{R}} = \frac{du}{d\bar{s}}\left[1 + \left(\frac{dw}{du}\right)^2 + \frac{\left(u + w\,\frac{dw}{du}\right)^2}{(1 - u^2 - w^2)}\right]^{1/2} = A_1\,\frac{du}{d\bar{s}} \qquad (C\text{-}8)$$

which is substituted into Eq. (C-7) to get the transformed n-momentum equation:

$$\frac{du}{d\bar{s}} = \frac{G_1}{A_1^2}\,\frac{dw}{du} + \frac{G_3}{A_1^3} + \frac{G_4}{A_1^2} \qquad (C\text{-}9)$$

This equation is used to calculate $(du/ds)_{j+1}$ by knowing u_{j+1}, w_{j+1}, $(dw/du)_{j+1}$, G_1, G_2, and G_3. Appropriate values of u are then obtained by utilizing:

(1) a backward finite difference scheme at the first step away from the injection point (i.e. $\bar{s} = \Delta\bar{s}$):

$$u_{j+1} = u_j + \Delta\bar{s}\left(\frac{du}{d\bar{s}}\right)_{j+1} \qquad (C\text{-}10)$$

and (2) a central finite difference scheme to get u_{j+2} at points on the remainder of the trajectory (i.e. $\bar{s} > \Delta\bar{s}$):

$$u_{j+2} = u_j + 2(\Delta\bar{s}) \left(\frac{du}{d\bar{s}}\right)_{j+1} \tag{C-11}$$

For the vertical or lateral injection situations, the auxilliary relation, Eq. (B-22), can be used to obtain a value of w_{j+2} corresponding to the value of u_{j+2} in Eq. (C-11), while its derivative,

$$u \frac{du}{ds} + w \frac{dw}{ds} = 0 \tag{C-12}$$

can be used to obtain a value of $(dw/ds)_{j+1}$, and hence $(dw/du)_{j+1}$. These parameters are used to iterate through the governing equations to obtain a solution for the two-dimensional trajectory. For the more general injection cases, the t-momentum equation is required to provide information on w and its derivatives.

t-Momentum

The direction cosine expressions from Appendix B are substituted into Eq. (52) and the resulting relation is divided by d_i/q_i to obtain the nondimensional t-momentum equation:

$$F_1 \bar{\tau}_o \frac{d\bar{R}}{d\bar{s}} + F_2 \bar{\tau}_o \frac{d^2w}{d\bar{s}^2} + F_3 \bar{\tau}_o + F_4 \left(\frac{d\bar{R}}{d\bar{s}}\right)^2 + F_5 \left(\frac{d^2u}{d\bar{s}^2}\right)^2 + F_6$$
$$+ F_7 \frac{d\bar{R}}{d\bar{s}} \frac{d^2u}{d\bar{s}^2} + F_8 \frac{d^2u}{d\bar{s}^2} + F_9 \frac{d\bar{R}}{d\bar{s}} + F_{10} \bar{\tau}_o \frac{d\bar{R}}{d\bar{s}} + F_{11} \bar{\tau}_o \frac{d^2u}{d\bar{s}^2} + F_{12} \bar{\tau}_o = 0 \tag{C-13}$$

where $\bar{\tau}_o = \tau_o d_i$ and

$$F_1 = \frac{g\,A}{d_i q_i}(\rho_\infty - \rho)\frac{dw}{d\bar{s}} \qquad F_2 = \frac{g\,A\,\bar{R}}{d_i q_i}(\rho_\infty - \rho)$$

$$F_3 = \frac{g\,A\,w}{d_i q_i \bar{R}}(\rho_\infty - \rho) \qquad F_4 = \frac{H}{5} C_{D_t}\left(\frac{q_\infty}{q_i}\right)\left(\frac{du}{d\bar{s}}\right)^2$$

$$F_5 = \frac{H}{5} C_{D_t}\left(\frac{q_\infty}{q_i}\right)\bar{R}^2 \qquad F_6 = \frac{H}{5} C_{D_t}\left(\frac{q_\infty}{q_i}\right)\frac{u^2}{\bar{R}^2}$$

$$F_7 = \frac{2\,H}{5} C_{D_t}\left(\frac{q_\infty}{q_i}\right)\bar{R}\frac{du}{d\bar{s}} \qquad F_8 = \frac{2H}{5} C_{D_t}\left(\frac{q_\infty}{q_i}\right) u$$

$$F_9 = \frac{2\,H}{5} C_{D_t}\left(\frac{q_\infty}{q_i}\right)\frac{u}{\bar{R}}\frac{du}{d\bar{s}} \qquad F_{10} = \frac{\pi}{2} J\left(\frac{V_\infty}{V_i}\right)\frac{du}{d\bar{s}}$$

$$F_{11} = \frac{\pi}{2} J\left(\frac{V_\infty}{V_i}\right)\bar{R} \qquad F_{12} = \frac{\pi}{2} J\left(\frac{V_\infty}{V_i}\right)\frac{u}{\bar{R}}$$

We have seen in Eqs. (B-26) and (B-27)that dR/ds and τ_o are functions of d^2w/ds^2, d^2u/ds^2, plus lower order terms. The approach used here is to define d^2u/ds^2 by using a finite difference approximation after a solution has been obtained from Eq. (C-9). The problem then becomes one of getting dR/ds and τ_o in terms of d^2w/ds^2. Thus, from Eq. (B-26) we have,

$$\frac{dR}{ds} = B_1 + B_2\left(\frac{d^2w}{ds^2}\right) \tag{C-14}$$

and from Eq. (B-27),

$$\tau_o = B_3 + B_4\left(\frac{d^2w}{ds^2}\right) \tag{C-15}$$

where the B coefficients are functions of u, w, du/ds, dw/ds, and d^2u/ds^2. When these relations are substituted into the t-momentum equation, Eq. (C-13), a quadratic expression in d^2w/ds^2 results:

$$B_5 \left(\frac{d^2w}{ds^2}\right)^2 + B_6 \left(\frac{d^2w}{ds^2}\right) + B_7 = 0 \qquad \text{(C-16)}$$

The coefficients are calculated from information obtained from the n-momentum equation, and a solution is acquired at point "j+1" by approximating d^2w/ds^2 with a central finite difference. This results in a quadratic in w_{j+2}, which is solved to provide an update on w_{j+2}, $(dw/ds)_{j+1}$, and $(dw/du)_{j+1}$.

It is desirable to demonstrate that the t-momentum equation is an identity for the vertical injection situation where the trajectory is two dimensional and is confined to the x-y plane. For this case, $\vec{e}_t$ is parallel to the z-axis which implies that the dot products of this vector with $\vec{e}_x$ and $\vec{e}_y$ in Eq. (51) are zero, and hence the t-momentum equation is an identity. This can be shown in a more rigorous fashion by considering the expressions for $(\vec{e}_x \cdot \vec{e}_t)$ and $(\vec{e}_y \cdot \vec{e}_t)$, Eqs. (B-18) and (B-19). Substituting for direction cosines into these two equations, we can write,

$$R \frac{d^2u}{ds^2} + \frac{dR}{ds}\frac{du}{ds} + \frac{u}{R} \stackrel{?}{=} 0 \qquad \text{(C-17)}$$

and

$$R \frac{d^2w}{ds^2} + \frac{dR}{ds}\frac{dw}{ds} + \frac{w}{R} \stackrel{?}{=} 0 \qquad \text{(C-18)}$$

where we want to prove that these relations are equal to zero for the vertical injection case. To do this it is necessary to use the auxilliary expressions that are presented in Eq. (B-22), with $\eta = 0$, and in Eq. (C-12). It is noted that Eq. (C-17) can be written as,

$$\frac{d}{ds}\left(R\,\frac{du}{ds}\right) + \frac{u}{R} \stackrel{?}{=} 0 \qquad \text{(C-19)}$$

The expression for R for a vertical injection case was shown in Appendix B, Eq. (B-30), and is substituted into the above equation to get,

$$u\,\frac{du}{ds} + w\,\frac{dw}{ds} \stackrel{?}{=} 0 \qquad \text{(C-20)}$$

which is definitely zero from Eq. (C-12).

The procedure is similar for Eq. (C-18) where we can write,

$$\frac{d}{ds}\left(R\,\frac{dw}{ds}\right) + \frac{w}{R} \stackrel{?}{=} 0 \qquad \text{(C-21)}$$

Eq. (C-12) is solved for dw/ds which, along with the relationship for R, is substituted into the above equation to obtain,

$$-\frac{du}{ds} + \frac{du}{ds} = 0 \qquad \text{(C-22)}$$

Thus, the dot products $(\vec{e}_x \cdot \vec{e}_t)$ and $(\vec{e}_y \cdot \vec{e}_t)$ are zero for the

vertical injection situation, and hence the t-momentum equation, Eq. (51), is an identity. This fact was used as a check of the computer results to see that the numerical output from the t-momentum equation was correct.

XVI. VITA

The author was born in [redacted] on [redacted]. After attending school through the ninth grade, a family move required that he finish the last three years of high school in Lewisburg, Pennsylvania. He entered Mississippi State University in September, 1959 and completed the requirements for a Bachelor of Science degree in Aerospace Engineering in May, 1963. Subsequently, he joined the staff of the National Aeronautics and Space Administration's Langley Research Center in Hampton, Virginia where he has since been employed.

In September, 1966 the author began work for the Master of Science degree in Aerospace Engineering at Virginia Polytechnic Institute and had completed the requirements in February, 1968. He commenced the academic course work leading toward the present degree in September, 1969.

[redacted]